Article

Current Biology

Invariant neural dynamics drive commands to control different movements

Highlights

- The same motor command is issued with different neural activity across movements
- A single model of neural dynamics predicts the different activity issuing a command
- These invariant dynamics propagate neural activity to issue the next command
- These dynamics reduce the input that neurons need to issue commands based on feedback

Authors

Vivek R. Athalye, Preeya Khanna, Suraj Gowda, Amy L. Orsborn, Rui M. Costa, Jose M. Carmena

Correspondence

va2371@columbia.edu (V.R.A.), pkhanna@berkeley.edu (P.K.), rc3031@columbia.edu (R.M.C.), jcarmena@berkeley.edu (J.M.C.)

In brief

The brain's capacity to control diverse movement may rely on reusing an invariant neural code. Athalye and Khanna et al. show that animals control a brain-machine interface using dynamics of neural population activity that are invariant across movements. A model demonstrates that invariant dynamics can help transform feedback into motor commands.

Athalye et al., 2023, Current Biology *33*, 2962–2976
July 24, 2023
https://doi.org/10.1016/j.cub.2023.06.027

CellPress

CellPress
OPEN ACCESS

Current Biology

Article

Invariant neural dynamics drive commands to control different movements

Vivek R. Athalye,[1,7,9,14,*] Preeya Khanna,[2,7,10,*] Suraj Gowda,[4] Amy L. Orsborn,[3,11] Rui M. Costa,[1,8,12,*] and Jose M. Carmena[4,5,6,8,13,*]

[1]Zuckerman Mind Brain Behavior Institute, Departments of Neuroscience and Neurology, Columbia University, New York, NY 10027, USA
[2]Department of Neurology, University of California, San Francisco, San Francisco, CA 94158, USA
[3]Departments of Bioengineering, Electrical and Computer Engineering, University of Washington, Seattle, Seattle, WA 98195, USA
[4]Department of Electrical Engineering and Computer Sciences, University of California, Berkeley, Berkeley, CA 94720, USA
[5]Helen Wills Neuroscience Institute, University of California, Berkeley, Berkeley, CA 94720, USA
[6]UC Berkeley-UCSF Joint Graduate Program in Bioengineering, University of California, Berkeley, Berkeley, CA 94720, USA
[7]These authors contributed equally
[8]Senior author
[9]Twitter: @vr_athalye
[10]Twitter: @prekhanna
[11]Twitter: @neuroamyo
[12]Twitter: @ruimcosta
[13]Twitter: @blancinegre1972
[14]Lead contact
*Correspondence: va2371@columbia.edu (V.R.A.), pkhanna@berkeley.edu (P.K.), rc3031@columbia.edu (R.M.C.), jcarmena@berkeley.edu (J.M.C.)
https://doi.org/10.1016/j.cub.2023.06.027

SUMMARY

It has been proposed that the nervous system has the capacity to generate a wide variety of movements because it reuses some invariant code. Previous work has identified that dynamics of neural population activity are similar during different movements, where dynamics refer to how the instantaneous spatial pattern of population activity changes in time. Here, we test whether invariant dynamics of neural populations are actually used to issue the commands that direct movement. Using a brain-machine interface (BMI) that transforms rhesus macaques' motor-cortex activity into commands for a neuroprosthetic cursor, we discovered that the same command is issued with different neural-activity patterns in different movements. However, these different patterns were predictable, as we found that the transitions between activity patterns are governed by the same dynamics across movements. These invariant dynamics are low dimensional, and critically, they align with the BMI, so that they predict the specific component of neural activity that actually issues the next command. We introduce a model of optimal feedback control (OFC) that shows that invariant dynamics can help transform movement feedback into commands, reducing the input that the neural population needs to control movement. Altogether our results demonstrate that invariant dynamics drive commands to control a variety of movements and show how feedback can be integrated with invariant dynamics to issue generalizable commands.

INTRODUCTION

The human brain can generate a vast variety of movements. It is believed that the brain would not have such capacity if it used separate populations of neurons to control each movement. Thus, it has been proposed that the brain's capacity to produce different movements relies on reusing the dynamics of a specific neural population's activity.[1–3] While theoretical work shows how dynamics emerge from neural activity transmitted through recurrent connectivity,[1,4–6] it has been elusive to identify whether the brain reuses dynamics to actually control movements.

Recent work on the motor cortex, a region that controls movement through direct projections to the spinal cord[7] and other motor centers,[8–10] has found that population dynamics are similar across different movements. Specifically, the spatial pattern of population activity at a given time point (i.e., the instantaneous firing rate of each neuron in the population) systematically influences what spatial pattern occurs next. Models of dynamics h that are invariant across movements[3] can predict the transition from the current population activity pattern x_t to the subsequent pattern x_{t+1}:

$$x_{t+1} = h(x_t) + \text{input}_t + \text{noise}_t, \quad \text{(Equation 1)}$$

where external input (input_t) and noise (noise_t) are typically unmeasured. Recent work[11] has provided the intuition that invariant dynamics bias neural activity to avoid "tangling," which

occurs when the same activity pattern undergoes different transitions in different movements. These dynamic models have explained features of neural activity that were unexpected from behavior,[11–14] such as oscillations,[12] and have predicted neural activity during different movements on single trials,[15–18] for single neurons' spiking,[15] for local field potential features,[19,20] and over many days.[18,21] These models also help predict behavior.[16,18,19,22]

While past work characterized the statistical relationship between invariant dynamics and behavior, it remains untested if invariant dynamics are actually used to issue commands for movement. This test requires identifying the causal transformation from neural activity to command, where the "command" is the instantaneous influence of the nervous system on movement. This is a longstanding challenge in understanding motor control. While past work has modeled this transformation,[23–25] ongoing research reveals its complexity.[8–10,26–28]

We addressed this challenge with a brain-machine interface (BMI)[29–32] in which the transformation from neural activity to command was known exactly and determined by the experimenter. We trained rhesus monkeys to use motor-cortex population activity to move a two-dimensional computer cursor on a screen through a BMI. The BMI transformed neural activity into a force-like command to update the cursor's velocity, analogous to muscular force on the skeleton. Thus, an individual movement was produced by a series of commands, where each command acted on the cursor at an instant in time.

We discovered that the same command is issued with different neural-activity patterns in different movements. Critically, these different patterns transition according to low-dimensional, invariant dynamics to patterns that issue the next command, even when the next command differs across movements. Thus, our results demonstrate that invariant dynamics drive commands to control different movements.

While past work has presented a view of how dynamics operate in a feedforward manner, propagating an initial state of activity[23,33,34] to produce movement, it has been unclear how feedback[24,35–37] integrates with invariant dynamics. Given that the motor cortex is interconnected to larger motor-control circuits including cortical[38–41] and cortico-basal ganglia-thalamic circuits,[8,9,42,43] we introduce a hierarchical model[44] of optimal feedback control (OFC) in which the brain (i.e., larger motor-control circuitry) uses feedback to control the motor-cortex population which controls movement.[45,46] Our model reveals that invariant dynamics can help transform feedback into commands, as they reduce the input that a population needs to issue commands. Altogether, our results demonstrate that invariant neural dynamics are both used and useful for issuing commands across different movements.

RESULTS

BMI to study neural population control of movement

We used a BMI[47–49] to study the dynamics of population activity as it issued commands for movement of a two-dimensional computer cursor (Figure 1A). Population activity (20–151 units) was recorded using chronically implanted microwire-electrode arrays spanning the bilateral dorsal premotor cortex and primary motor cortex. Each unit's spiking rate at time t (computed as the number of spikes in a temporal bin) was stacked into a vector of population activity x_t, and the BMI used a "decoder" given by matrix K to linearly transform population activity into a two-dimensional command:

$$\text{command}_t = Kx_t. \quad \text{(Equation 2)}$$

The command linearly updated the two-dimensional velocity vector of the computer cursor:

$$\text{velocity}_t = \text{command}_t + \alpha * \text{velocity}_{t-1} + \text{offset}. \quad \text{(Equation 3)}$$

We note that the BMI was not identical across the two subjects, as neural activity was modeled with different statistical distributions (Gaussian for monkey G and a point process[47,48] for monkey J; see STAR Methods section neuroprosthetic decoding).

The decoder was initialized as subjects passively watched cursor movement, calibrated as subjects used the BMI in closed loops[49] without performing trained overt movement and then fixed for the experiment (Figure 1B). Critically, the decoder was not fit during trained overt movement, as was done previously,[16] so it did not demand neural dynamics associated with overt movement.

To study control of diverse movements, we trained monkeys to perform two different tasks (Figures 1C and 1D). Monkeys performed a center-out task in which they moved the cursor from the center of the workspace to one of eight radial targets, and they performed an obstacle-avoidance task in which they avoided an obstacle blocking the straight path to the target. Our tasks elicited up to 24 conditions of movement (with an average of 16–17 conditions per session), where each condition is defined as the task performed ("co" = center-out task; "cw"/"ccw" = clockwise/counterclockwise movement around the obstacle in the obstacle-avoidance task) and the target achieved (numbered 0–7).

Importantly, the BMI enabled us to identify when neural activity issued the same command in different conditions (Figures 1E, 1F, and S1). We considered two-dimensional, continuously valued commands as the same if they fell within the same discrete bin for analysis. We categorized commands into 32 bins (8 angular × 4 magnitude) based on percentiles of the continuously valued distribution (Figure S1A; STAR Methods section command discretization for analysis). In each session, a command (of the 32 discretized bins) was analyzed if it was used in a condition 15 or more times (Figure S1B), for more than one condition. Each individual command was used with regularity during multiple conditions (average ~7 conditions) (Figure S1B), within distinct local "subtrajectories" (Figures 1F and S1; STAR Methods section cursor and command trajectory visualization).

Using the BMI to test whether invariant dynamics are used to control different movements

The BMI enabled us to test whether the pattern of neural activity systematically influences the subsequent pattern and command. We can visualize an activity pattern x_t as a point in high-dimensional activity space, where each neuron's

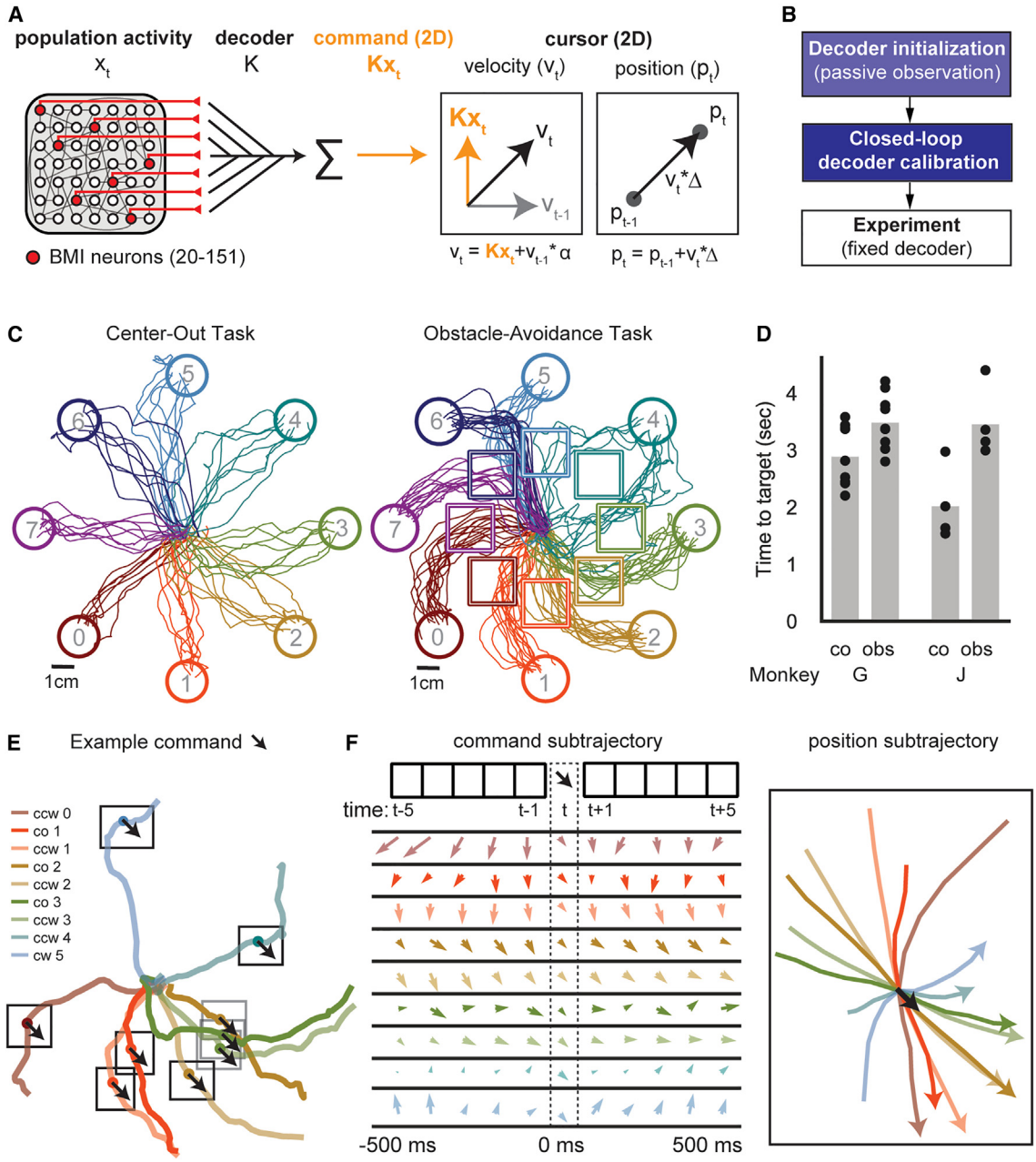

Figure 1. BMI to study neural population control of movement

(A) Schematic of the BMI system.

(B) Schematic of decoder calibration.

(C) Single trials of BMI control.

(D) Average target-acquisition time per session.

(E) Example of the same command (black arrow) being issued during single trials under different conditions. The example command was in the −45° direction and the smallest magnitude bin of analysis.

(F) Left: the average command subtrajectory from −500 to 500 ms. Right: the average position subtrajectory from −500 to 500 ms.

See Figure S1 for analysis of subtrajectories.

activity is one dimension, and visualize the transition between two patterns x_t and x_{t+1} as an arrow (Figure 2A). Then, dynamics can be visualized as a flow field in activity space. This flow field is invariant because the predicted transition for a given neural-activity pattern (i.e., its arrow) does not change, regardless of the current command or condition. Because there are more neurons than dimensions of the command, different activity patterns can issue the same command[24,50] (Figure 2B), as is believed to be true in the natural motor system.[23,24,50] The BMI decoder defined the "decoder

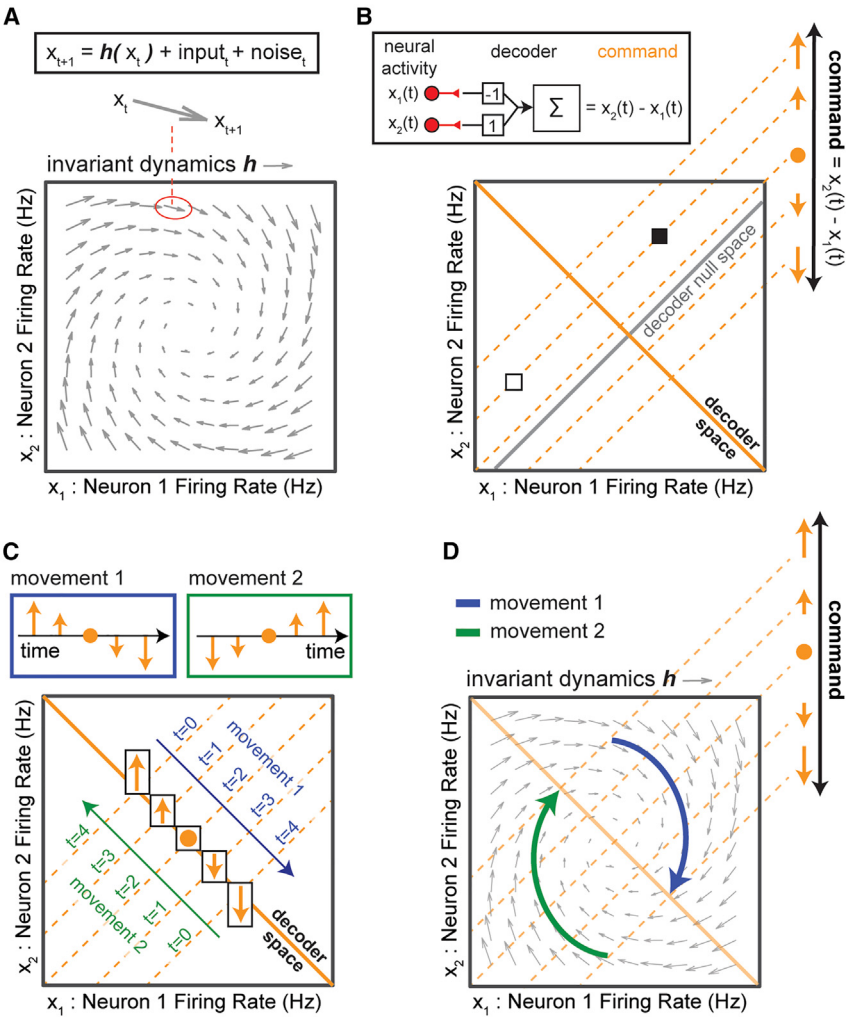

Figure 2. Using the BMI to test whether invariant dynamics are used to control different movements

(A) Illustration of invariant dynamics.

(B) Multiple neural-activity patterns (e.g., white and black square) issue the same command. An illustrative decoder defines the command at time *t* as the difference between two neurons' instantaneous activity $x_2(t) - x_1(t)$, symbolized with orange arrows (top right) indicating the command's magnitude and sign.

(C) A trajectory of commands (orange arrows) produces one whole movement. Movements 1 (blue) and 2 (green) are driven by the same commands in different temporal orders.

(D) Neural activity that follows invariant dynamics *h* in order to issue the commands for movement.

See Figure S3D for another example of invariant dynamics (decaying dynamics).

space" as the dimensions of neural activity that determine the command and the "decoder-null space" as the orthogonal dimensions, which have no consequence on the decoder. The BMI allowed us to observe the precise temporal order of commands (Figure 2C) and test whether activity trajectories followed the flow of invariant dynamics to issue these commands for movements (Figure 2D).

The same command is issued by different neural-activity patterns in different movements

First, we tested whether the same command is issued by different neural-activity patterns in different movements, as would be expected if the current pattern influences the subsequent pattern and command (Figure 3A). The BMI enabled this analysis with its concrete definition of the command for movement. We calculated the distance between (1) the average neural activity for a given command and condition and (2) the average neural activity for the given command pooled over conditions. We then tested if this distance is larger than expected simply due to the variability of noisy neural activity. To emulate the scenario in which neural activity for a given command has the same distribution across conditions, we constructed shuffled datasets where we identified all observations of neural activity issuing a given command and shuffled their condition-labels, for all commands (STAR Methods section behavior-preserving shuffle of activity). In this scenario, the distance is expected to be greater than zero simply because average activity is estimated from limited samples and thus is subject to variability.

Overall, neural activity issuing a given command significantly deviated across conditions relative to the shuffle distribution (Figures 3B–3E). Distances averaged within sessions ranged from 10% to 200% larger than shuffle distance (Figure 3D; see also Figure S2 for additional distributions). Distances were significantly larger than shuffle distances for a large fraction of individual command/condition tuples (~30% for monkey G, ~70% for monkey J), individual commands (~65% for G, ~90% for J) when aggregating over conditions, and individual neurons (~40% for G, ~80% for J) when aggregating over all command/condition tuples (Figure 3E). Further, these deviations reflected the behavior; the distance between two patterns issuing the same command correlated with the distance between the command subtrajectories (Figures S6E–S6H).

Invariant dynamics predict the different neural-activity patterns used to issue the same command

Given that a command was not issued with the same activity pattern across conditions, we next constructed a model of invariant dynamics. We used single-trial neural activity x_t from all conditions to estimate dynamics with a linear model (Figure 4A):

$$x_{t+1} = Ax_t + b. \qquad \text{(Equation 4)}$$

We found that the dynamics *A* were low-dimensional (~4 dimensions) (Figures 5D and S3B) and decaying to a fixed point

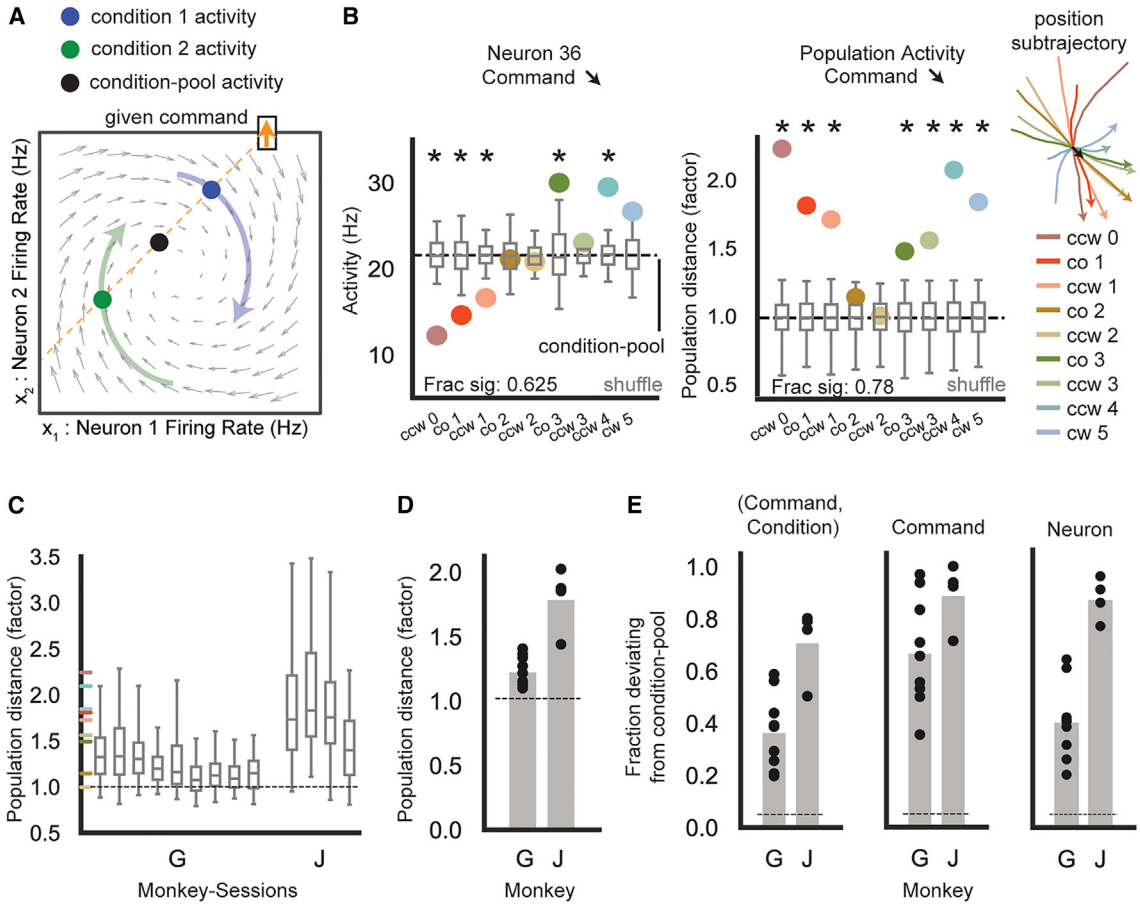

Figure 3. The same command is issued by different neural-activity patterns in different movements

(A) The same command (orange upward arrow) is issued in different conditions with different activity patterns (blue and green dots). These patterns deviate from the condition-pooled average activity pattern for the command (black dot).

(B) Left: example neuron's average firing rate (colored dots) for the example command and conditions from Figure 1F (position subtrajectories plotted at right legend), as well as the condition-pooled average activity (dashed black line labeled "condition-pool"). The condition-shuffled distributions of average activity are shown with gray boxplots indicating the 2.5th, 25th, 50th, 75th, and 97.5th percentiles. Asterisk indicates the distance for the command/condition/neuron exceeded the shuffle distance ($p < 0.05$); 5/9 or 62.5% of the examples were significant. Distance was significantly greater than shuffle distance aggregating over all command/condition/neuron tuples: for monkeys G and J, $p < 0.001$ for 9/9 and 4/4 sessions, respectively; $p < 0.001$ for pooled sessions. Right: population distance normalized to the shuffle mean (colored dots); 7/9 or 78% of examples were significant. Figure S2A shows population distances for all command/condition tuples in this session.

(C) The distribution of normalized population distances across command/condition tuples. Colored ticks indicate distances in (B, right). See Figures S2B and S2C for additional distance distributions.

(D) Normalized population distance averaged across command/condition tuples, for monkeys G and J: n = 9 and 4 sessions, respectively. Bars indicate the average across sessions. Population distance was significantly greater than shuffle distances, aggregating over all command/condition tuples; for monkeys G and J, $p < 0.001$ for 9/9 and 4/4 sessions, respectively; $p < 0.001$ for pooled sessions.

(E) Left: fraction of command/condition tuples with distance significantly greater than shuffle distance. Middle: fraction of commands with distance significantly greater than shuffle distance, aggregating over conditions. Right: fraction of neurons with distance significantly greater than shuffle distance, calculated for each command/condition separately and aggregating over all command/condition tuples for statistics. Dashed line indicates chance level (fraction equal to 0.05 significantly deviating from shuffle distance), and data points are each of 9 and 4 sessions for monkey G and J, respectively. See Figures S6E–S6H for the relationship between population distance and command subtrajectories across pairs of conditions.

See Table S1 for statistical details.

(Figures S3A–S3C), contrasting with rotational dynamics observed during natural motor control.[12,13,16,22,51] See Figure S3D for an illustration of how decaying invariant dynamics can control different movements. Notably, a nonlinear-model (a recurrently switching linear dynamical system[52]) did not outperform these simple linear dynamics (Figures S5C–S5F).

We asked whether invariant dynamics predict the different activity patterns observed to issue the same command. Concretely, we predicted the activity pattern given the command it issued and its previous activity (Figure 4A; STAR Methods section invariant dynamics model predictions), combining the dynamics model (Equation 4) with the decoder (Equation 2). This analyzed whether the model could predict the component of the activity pattern that can vary when a given command is issued, i.e., the component in the decoder-null space. For comparison, we also computed the prediction of neural activity

CellPress
OPEN ACCESS

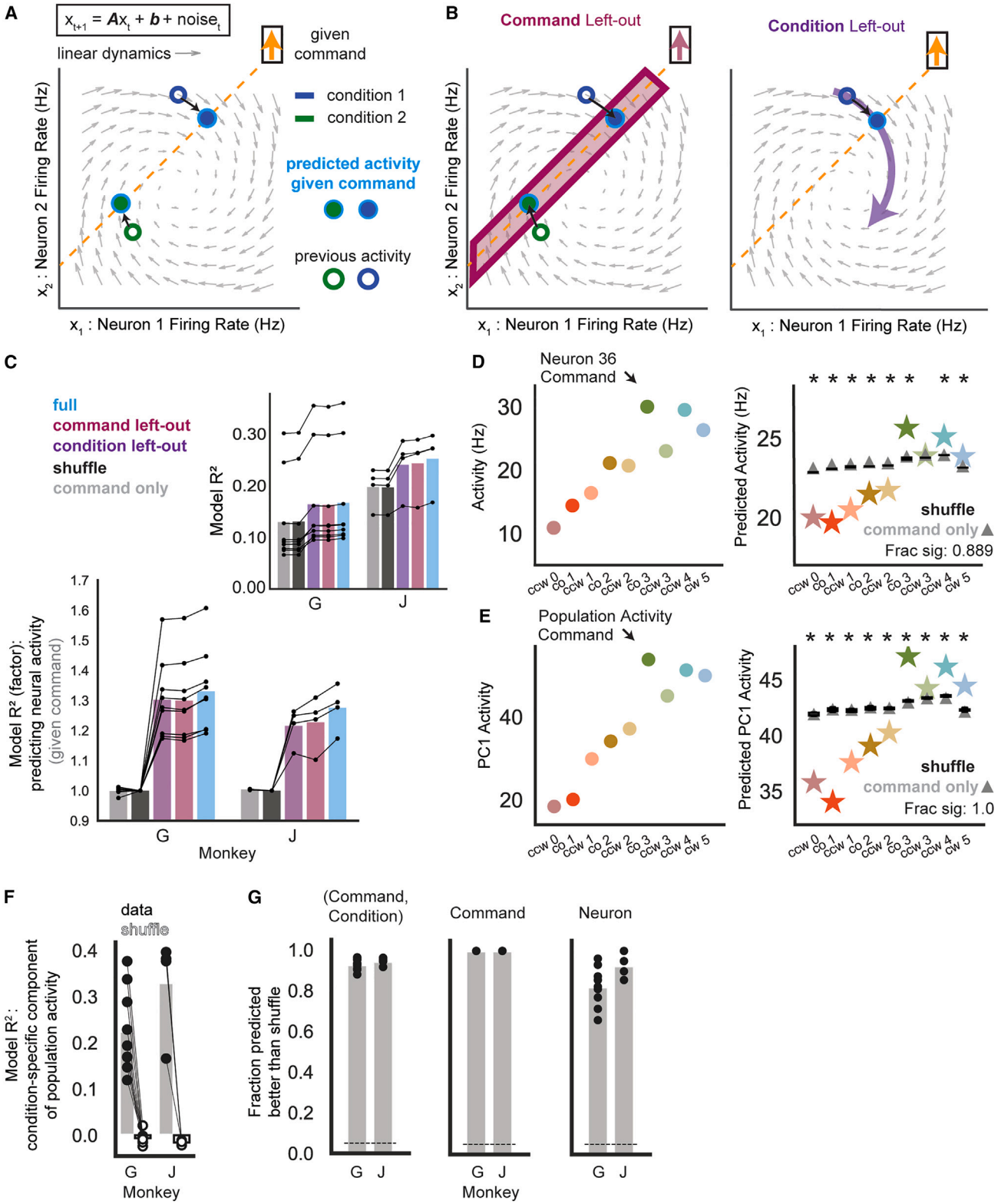

Figure 4. Invariant dynamics predict the different neural activity patterns used to issue the same command

(A) A linear-dynamics model predicts the different activity patterns (cyan-outlined dots) that issue a given command (orange arrow) based on previous activity. See Figure S6 for predictions of the relationship between activity patterns across pairs of conditions.

(legend continued on next page)

only when given the command it issued (in the absence of a dynamics model). Further, we tested whether the invariant-dynamics model generalized to new commands and conditions. Dynamics models were fit on neural activity specifically excluding individual commands or conditions, and these models were used to predict the neural activity for the left-out commands or conditions (Figures 4B and S4; STAR Methods section invariant-dynamics models).

We tested whether the dynamics model's accuracy exceeded a dynamics model fit on the shuffled datasets that preserved the temporal order of commands while shuffling the neural activity issuing the commands (STAR Methods section behavior-preserving shuffle of activity). The shuffle-dynamics model captured the expected predictability in neural activity due to the predictability of commands in the performed movements.

On the level of single time points in individual trials, we found that the dynamics model significantly exceeded shuffle dynamics in predicting the activity pattern issuing a given command based on the previous pattern. Importantly, it generalized across "left-out" commands and conditions (Figure 4C) and even when much larger subsets of commands and conditions were left out (Figure S4). We confirmed that the result was not driven by neural activity simply representing behavioral variables (cursor kinematics, target location, and condition) in addition to the command (Figures S5A and S5B), consistent with previous work.[53]

The invariant-dynamics model also predicted the different average activity patterns for each command and condition (Figures 4D–4G) significantly better than shuffle dynamics. It predicted 20%–40% of the condition-specific component of neural activity (i.e., the difference between average activity for a command/condition and the prediction of that activity based on the command alone) (Figure 4F; STAR Methods section invariant dynamics model predictions). The model predicted neural activity for the vast majority of commands, conditions, and neurons (Figure 4G), revealing that dynamics were indeed invariant.

Finally, the dynamics model preserved structure of neural activity across pairs of conditions (Figures S6A–S6D) and predicted that the distance between two activity patterns issuing the same command would be correlated with the distance between the corresponding command subtrajectories (Figures S6E–S6I). Altogether, these results show that invariant dynamics contribute to what activity pattern was used to issue a command, generalizing across commands and conditions.

Invariant dynamics align with the decoder, propagating neural activity to issue the next command

We next asked whether invariant dynamics were actually used to transition between commands. Concretely, we used the dynamics model (Equation 4) to predict the transition from the current activity pattern to the next pattern, and then we applied the BMI decoder to this prediction of next pattern in order to predict the next command (i.e., its continuous value) (Figure 5A). We used the same dynamics model fit in Figure 4, except here we did not combine the model with given information about the command. This tests whether invariant dynamics predict the component of neural activity in the decoder space, which actually drives the BMI. The BMI enabled this analysis as it defines the transformation from neural activity to command, which has not been measurable during natural motor control.

We emphasize that one possibility is that invariant dynamics accompany commands without actually driving them, i.e.,

(B) Models were tested on neural activity for a command (left, magenta) or condition (right, purple) left-out of training the model. See Figure S4 for elaboration on invariant dynamics generalization.

(C) The coefficient of determination (R^2) of models predicting neural activity given the command it issues and previous activity, evaluated on test data not used for model fitting, for monkeys G and J, n = 9 and 4 sessions, respectively. See Figure S3 for properties of the models. Inset shows raw R^2, where "shuffle" is the 95th percentile of the shuffle distribution of R^2. Main panel shows R^2 normalized to shuffle. Full dynamics, command left-out dynamics, and condition left-out dynamics all predicted neural activity significantly better than shuffle dynamics. For each model, for monkeys G and J, $p < 0.001$ for 9/9 and 4/4 sessions, respectively; $p < 0.001$ for sessions pooled. Figure S5 shows models with behavior variables and nonlinear dynamics.

(D) Left: average activity for the example neuron, command, and conditions from Figure 3B, left. Right: prediction of the activity in left panel by the full-dynamics model (stars), the shuffle-dynamics model (black boxplot distribution), and the model predicting neural activity only using the command (gray triangle); 8/9 (88.9%) of these examples were predicted significantly better than shuffle dynamics. The full-dynamics model predicted individual neuron activity better than shuffle dynamics, aggregating over all command/condition/neuron) tuples (for monkeys G and J, $p < 0.001$ for 9/9 and 4/4 sessions, respectively; $p < 0.001$ for pooled sessions).

(E) Left: average population activity for the example command and conditions from Figure 3B right, visualized along the activity dimension that captured the most variance (the first principal component, labeled "PC1," of condition-specific average population activity). Right: prediction of activity in left panel by the full-dynamics model (stars), the shuffle-dynamics model (black boxplot distribution), and the model predicting neural activity only using the command (gray triangle); 9/9 (100.0%) of these examples were predicted with significantly lower error than shuffle dynamics (prediction was calculated using full population activity, not just PC1). The full-dynamics model predicted population activity with lower error than shuffle dynamics, aggregating over all command/condition/neuron tuples (for monkeys G and J, $p < 0.001$ for 9/9 and 4/4 sessions, respectively; $p < 0.001$ for pooled sessions).

(F) Model R^2 from predicting the component of average neural activity for a given command that is specific to a condition, comparing the full-dynamics model (dark gray bar and filled dots) with the mean of the shuffle-dynamics model (light bar and empty dots) (for monkeys G and J, n = 9 and 4 sessions, respectively). The full-dynamics model predicted significantly more variance than shuffle dynamics (for monkeys G and J, $p < 0.001$ for 9/9 and 4/4 sessions, respectively; $p < 0.001$ for pooled sessions).

(G) Left: fraction of command/condition tuples where full dynamics predicts average population activity significantly better than shuffle dynamics. Center: fraction of commands where full dynamics predicts average population activity significantly better than shuffle dynamics, calculated for each condition separately and then aggregated over all conditions for statistics. Right: fraction of neurons where full dynamics predicts the neuron's average activity significantly better than shuffle dynamics, calculated for each command/condition separately and then aggregated over all command/condition tuples for statistics. Dashed line indicates chance level (fraction equal to 0.05 significantly better than shuffle), and data points are each of 9 and 4 sessions for monkey G and monkey J, respectively.

See Table S1 for statistical details.

CellPress
OPEN ACCESS

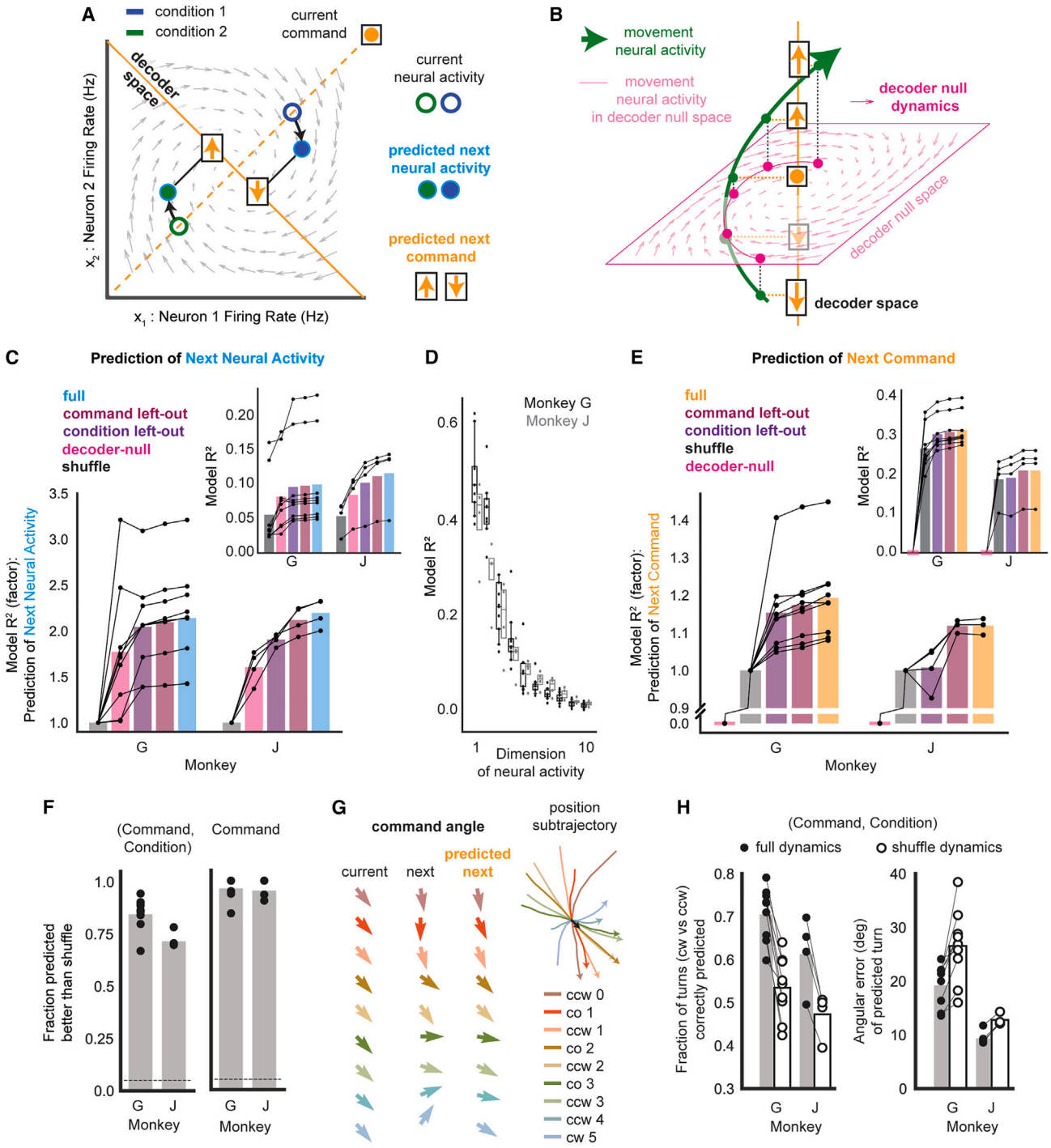

Figure 5. Invariant dynamics align with the decoder, propagating neural activity to issue the next command

(A) A linear-dynamics model predicts the transition from current neural activity (colored rings) to next neural activity (cyan-outlined dots) and next commands (orange symbols) (i.e., the component of neural activity in the decoder space).

(B) If invariant dynamics are low-dimensional and only occupy the decoder-null space (pink plane), then they do not predict the next command (i.e., the component of neural activity in the decoder space).

(C) The coefficient of determination (R^2) of models predicting next neural activity given current neural activity, evaluated on test data not used for model fitting (for monkeys G and J, n = 9 and 4 sessions, respectively). Inset shows raw R^2, where shuffle is the 95th percentile of the shuffle distribution of R^2. Main panel shows R^2 normalized to shuffle. All models predicted next neural activity significantly better than shuffle dynamics. For each model, monkey G and monkey J. $p < 0.001$ for 9/9 and 4/4 sessions, respectively; $p < 0.001$ for sessions pooled.

(D) R^2 of full model for each neural activity dimension (dynamics eigenvector), sorted by R^2.

(legend continued on next page)

without predicting the component of neural activity in the decoder space (Figure 5B). Invariant dynamics that are low-dimensional might only occupy dimensions that are orthogonal to the decoder, such that they only predict the component of neural activity in the decoder-null space. To assess this possibility, we fit an invariant-dynamics model on the component of neural activity in the decoder-null space ("decoder-null dynamics") (STAR Methods section invariant dynamics models). While this model was restricted to the decoder-null space, it maintained similar dimensionality and eigenvalues to the full-dynamics model (Figures S3B and S3C).

Both the full dynamics and the decoder-null-dynamics model predicted next neural activity significantly better than shuffle dynamics (Figure 5C) on the level of single time points in individual trials. This reveals that invariant dynamics occupied decoder-null dimensions. Given that the full-dynamics model was low-dimensional (Figure S3B) and predicted ~4 dimensions more accurately than the rest of neural activity (Figure 5D), we next tested whether the dynamics aligned with the decoder. Critically, the full-dynamics model predicted the next command (Figure 5E) better than shuffle dynamics, while decoder-null dynamics provided absolutely no prediction for the next command, as expected by construction. The dynamics were invariant, as the full-dynamics model generalized across commands and conditions that were omitted from model fitting (Figure 5E) and predicted the next command for the majority of (command, condition) tuples (Figure 5F). These predictions preserved structure across pairs of conditions, such that invariant dynamics indicated how similar the next command would be across pairs of conditions (Figures S6I–S6K).

Notably, invariant dynamics could predict the turn that the next command would take following a given command in a specific condition relative to the average next command (averaged across conditions for the given current command) (Figures 5G and 5H). Specifically, the dynamics model predicted whether the turn would be clockwise or counterclockwise (Figure 5H, left) and the angle of turn (Figure 5H, right) better than shuffle dynamics. Altogether, these results show that invariant dynamics align with the decoder and are used to transition between commands.

An OFC model reveals that invariant dynamics reduce the input that a neural population needs to issue commands based on feedback

We observe that the invariant-dynamics model did not perfectly predict transitions between commands. Throughout movement there were substantial residuals (Figures S3E–S3G), consistent with ongoing movement feedback driving neural activity in addition to invariant dynamics. However, it has been unclear how the brain can integrate feedback with invariant dynamics to control movement. Thus, we constructed a model of OFC that incorporates invariant neural dynamics.

We introduce a hierarchical model in which the brain (i.e., larger motor-control circuitry) controls the neural population, which controls movement of the BMI cursor (Figure 6A; Equation 5). Population activity x_t issues commands for movement and is driven by three terms: invariant dynamics (which we hypothesize are intrinsic to some connectivity of the neural population), input, and noise. The brain transforms ongoing cursor state and population activity into the input to the population, which is necessary to achieve successful movement. Concretely, the brain acts as an optimal linear feedback controller with knowledge of the neural population's invariant dynamics, the BMI decoder, and the condition of movement. In this formulation, the brain's objective is to achieve the target while using the smallest possible input to the population. This objective minimizes the communication from the brain to the population, which we can think of as minimizing the specific synaptic input to the neural population that would not be predicted based on the current state of the population's firing rates. Importantly, this incentivized the OFC model to optimize input in order to use invariant dynamics to control movement, rather than relying solely on input to issue commands. Consistent with this formulation, experiments show that thalamic input into motor cortex is optimized during motor learning.[54]

$$\begin{aligned} x_{t+1} &= Ax_t + b + \text{input}_t + \text{noise}_t \\ \text{input}_t &= f_t^{\text{LQR}}(x_t, \text{cursor}_t, \text{condition}) \\ \text{cursor}_{t+1} &= \text{BMI}(\text{cursor}_t, x_t) \end{aligned} \qquad \text{(Equation 5)}$$

We used this model to address whether observed invariant dynamics could be used for feedback control; future work will be needed to compare actual synaptic input to predicted input from

(E) Same as (C), except prediction of next command given current neural activity (monkey G [J]: n = 9 [4] sessions). All models except decoder-null dynamics predicted next command significantly better than shuffle dynamics. For condition left-out dynamics (purple), monkey G and monkey J, $p < 0.001$ for 9/9 and 2/4 sessions, and $p < 0.05$ for 9/9 and 3/4 sessions, respectively; p = n.s. for 0/0 and 1/4 sessions, respectively; $p < 0.001$ for sessions pooled. For full dynamics and command left-out dynamics, monkey G and monkey J, $p < 0.001$ for 9/9 and 4/4 sessions, respectively; $p < 0.001$ for sessions pooled.

(F) Analyses how well the next command is predicted for individual command/condition tuples. The full-dynamics model predicted condition-specific next command better than shuffle dynamics, aggregating over all command/condition tuples (for monkeys G and J, $p < 0.001$ for 9/9 and 4/4 sessions, respectively; $p < 0.001$ for pooled sessions). Left: fraction of command/condition tuples where full dynamics predicts the next command significantly better than shuffle dynamics (monkeys G and J, n = 9 and 4 sessions, respectively). Right: fraction of commands where full dynamics predicts the next command significantly better than shuffle dynamics, calculated for each condition separately and then aggregated over all conditions for statistics (monkeys G and J, n = 9 and 4 sessions, respectively). Dashed line indicates chance level (fraction equal to 0.05 significantly better than shuffle).

(G) Visualization of the command angle (left) (i.e., the direction that the command points) for the example command and conditions (right) from Figure 3B. For each condition (each row): visualization shows the average current command angle (first column); the average next command angle (second column); and the prediction of the average next command angle by the full-dynamics model (third column).

(H) For each command/condition tuple, prediction of the angle between the next command and the condition-pooled average next command. Left: fraction of command/condition tuples for which the sign of the angle is accurately predicted (positive, turn counterclockwise; negative, turn clockwise). Full-dynamics predictions are significantly more accurate than shuffle dynamics (for monkeys G and J, $p < 0.001$ for 9/9 and 4/4 sessions, respectively; $p < 0.001$ for pooled sessions. Right: error in predicted angle. Full dynamics predictions are significantly more accurate than shuffle dynamics (for monkeys G and J, $p < 0.001$ for 9/9 4/4 sessions, respectively; $p < 0.001$ for pooled sessions).

See Table S1 for statistical details. See also Figure S5 for models with behavior variables and nonlinear dynamics.

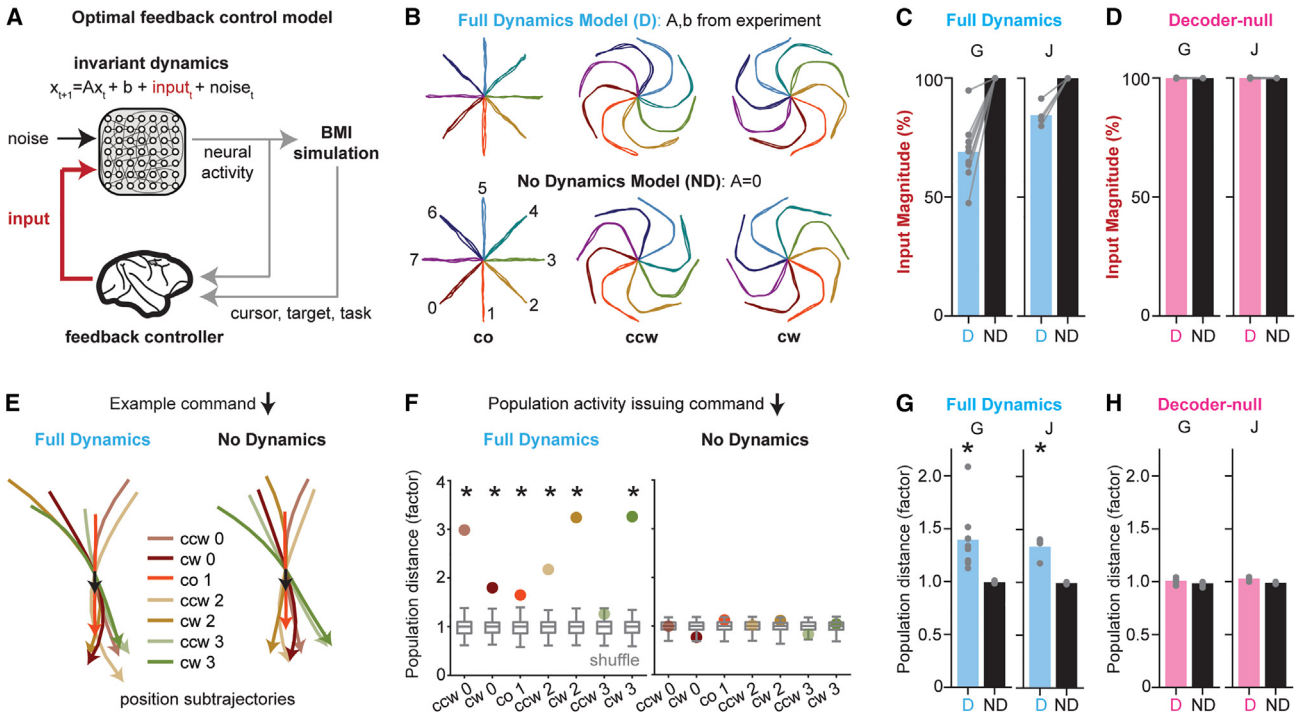

Figure 6. An OFC model reveals that invariant dynamics reduce the input that a neural population needs to issue commands based on feedback

(A) A model of OFC for movement that incorporates invariant neural dynamics.

(B) Three simulated trials for each condition (center-out [co], counterclockwise [ccw], and clockwise [cw] movements to 8 targets resulting in 24 conditions). Top: full-dynamics model that uses invariant dynamics fit on experimental data. Bottom: no-dynamics model that uses dynamics matrix A set to 0.

(C) Input magnitude as a percentage of the no-dynamics model (for monkeys G and J, n = 9 and 4 sessions, respectively). The population required significantly less input to control movement under the full-dynamics model (D, cyan) as compared with the no-dynamics model (ND, black). Un-normalized data were pooled across sessions and compared with a linear mixed effect (LME) model between input magnitude and model category with session modeled as random effect (for monkeys G and J, $p < 0.001$). Individual sessions were analyzed with a Wilcoxon signed-rank test that paired conditions across the models (monkeys G and J, $p < 0.05$ for 9/9 and 4/4 sessions, respectively).

(D) Same as (C) but for decoder-null dynamics. There was no significant difference in input magnitude between decoder-null dynamics (D, pink) and no dynamics (ND, black) when pooling across sessions (for monkeys G and J, $p > 0.05$) and on individual sessions (monkeys G and J, $p < 0.05$ for 0/9 and 0/4 sessions, respectively).

(E) The same command is issued across conditions in both the full-dynamics model and no-dynamics model. Average position subtrajectories are shown locked to an example command across conditions.

(F) Distance between average population activity for a command/condition and the average activity for the command pooling across conditions, normalized by the mean distance of the shuffle distribution (gray boxplots showing mean, 0^{th}, 25^{th}, 75^{th}, and 95^{th} percentile). Left: data from full-dynamics model. Right: data from the no-dynamics model. Asterisk indicates that distance is greater than shuffle ($p < 0.05$).

(G) Same as (F), but each point is an individual session pooling over command/condition tuples (monkeys G and J, n = 9 and 4 sessions, respectively). Population distances for the full-dynamics model were greater than shuffle. Data were pooled over sessions using a LME with session modeled as random effect (for both monkeys, $p < 0.001$), and individual sessions were analyzed with a Mann-Whitney U test ($p < 0.05$ for monkeys G and J on 9/9 and 4/4 sessions, respectively). No difference was detected in population distances between the no-dynamics model and shuffle when pooling across sessions (monkey G [J]: $p > 0.05$) and on individual sessions ($p < 0.05$ for monkey G [J] on 0/9 [0/4] sessions).

(H) Same as (G), but for the decoder-null-dynamics model (D, pink). No difference was detected in population distances between the decoder-null-dynamics model and shuffle when pooling across sessions (for both monkeys, $p > 0.05$) and on individual sessions ($p < 0.05$ for monkeys G and J on 0/9 and 0/4 sessions, respectively). Also, no difference was detected in population distances between the no-dynamics model and shuffle when pooling across sessions (for monkeys G and J, $p > 0.05$) and on individual sessions ($p < 0.05$ for monkeys G and J on 0/9 and 0/4 sessions, respectively).

See Table S2 for statistical details. See also Figures S3E–S3G for experimental data consistent with the model's view that invariant dynamics interact with ongoing input to control movement.

a feedback control model. For our question, the model needed to produce task movements, but these movements did not need to resemble experimentally observed movements. We simulated the model performing center-out and obstacle-avoidance movements with the decoders that were used in BMI experiments (STAR Methods section optimal feedback control model and simulation). In the full-dynamics model, the brain computed the minimal input to a population that followed the invariant dynamics we observed experimentally. In the no-dynamics model, the minimal input was computed to a neural population that had no invariant dynamics (i.e., the *A* matrix was set to zero). To facilitate comparison, we designed the models to receive the same noise magnitude and to produce behavior with equal success and target-acquisition time (Figure 6B).

These simulations revealed that the population required significantly less input in the full-dynamics model than in the no-dynamics model (Figure 6C). This effect was erased in the decoder-null-dynamics model (Figure 6D), in which the OFC model's invariant dynamics were restricted to the decoder-null space. These results show that invariant dynamics that specifically align with the decoder, as experimentally observed, can help the brain perform feedback control, reducing the input that the population needs to issue commands based on feedback.

Finally, we confirmed the principle that feedback control with invariant dynamics makes use of distinct activity patterns to issue a particular command. As in Figure 3, we compared the OFC models' neural activity against shuffled activity that preserved the temporal order of commands. The population activity distances for command/condition tuples were significantly larger than shuffle in the full-dynamics model but not in the no-dynamics model (Figures 6F and 6G). Further, this effect depended on alignment between invariant dynamics and the decoder, as we detected no difference between the decoder-null-dynamics model and shuffle (Figure 6H). Thus, the OFC model used different neural activity patterns to issue the same command only when the invariant dynamics were useful for feedback control.

DISCUSSION

Theoretical work shows that recurrent connectivity can give rise to neural population dynamics for motor control[1,4,5] and endow the brain with the capacity to generate diverse physical movements.[3] Experimental work has found that population activity in the motor cortex follows similar and predictable dynamics across different movements.[11,12,16] But it has been untested whether dynamics that are invariant across movements are used to actually control movement, as the transformation from neural activity to motor command has been challenging to measure[26,27] and model.[23–25] Here, we use a BMI to perform that test.

We discovered that different neural-activity patterns are used to issue the same command in different movements. The activity patterns issuing the same command vary systemically depending on the past pattern, and critically, they transition according to low-dimensional, invariant dynamics toward activity patterns that causally drive the subsequent command. Our results' focus on the command provides a conceptual advance beyond previous work that characterized properties of dynamics during behavior,[12,13,15,16] revealing that invariant dynamics are actually used to control movement.

Further, it has been unclear how the brain could integrate invariant dynamics with feedback[24,35–37] to control movement. We introduce a hierarchical model[44] of OFC, in which the brain uses feedback to control a neural population that controls movement. Optimal-control theory reveals that invariant dynamics that are aligned to the decoder can help the brain perform feedback control of movement, reducing the input that a population needs to issue the appropriate commands. The model verified that when invariant dynamics are used for feedback control, the same command is issued with different neural-activity patterns across movements. Altogether, these findings form a basis for future studies on what connectivity and neural populations throughout the brain give rise to invariant dynamics, whether the brain sends inputs to a neural population to take advantage of invariant dynamics and whether invariant dynamics actually drive muscles during physical movement.

These results provide strong evidence against one traditional view that the brain reuses the same neural population activity patterns to issue a particular command. This perspective is present in classic studies that describe neurons as representing movement parameters.[55,56] It is still debated what movement parameters are updated by motor cortex neurons,[28,57–59] as population activity encodes movement position,[60–62] distance,[63] velocity,[61,62] speed,[64] acceleration,[65] and direction of movement,[64,66–68] as well as muscle-related parameters such as force/torque,[55,68–70] muscle synergies,[71,72] muscle activation,[73–75] and even activation of motor units.[27] Regardless of how commands from the motor cortex update physical movement, our findings using a BMI strongly suggest that the motor cortex does not use the same neural-activity pattern to issue a specific motor command. Our findings instead support the recent proposal that neural activity in the motor cortex avoids tangling[11] while issuing commands.

We found that invariant dynamics do not perfectly determine the neural population's next command. We propose that, as the brain sends input to the neural population, it performs feedback control on the state of the neural population's invariant dynamics in order to produce movement. This proposal expands the number of behaviors for which invariant dynamics are useful. This is because invariant dynamics do not need to define the precise neural trajectories[12,34] that produce movement; they only need to provide useful transitions of neural activity that inputs can harness to control movement. In our data, simple dynamics (decaying dynamics with different time constants) in a low-dimensional activity space (~4 dimensions) were used to control many conditions of movement (~20 conditions). We find that invariant dynamics constrain neural activity in dimensions which do not directly matter for issuing current commands,[50] so that inputs in these dimensions can produce future commands (Figure 6C). This mechanism refutes a simplistic interpretation of the minimal intervention principle[76] in which neural activity should only be controlled in the few dimensions that directly drive commands. This also accords with the finding that motor cortex responses to feedback are initially in the decoder-null space before transitioning to neural activity that issues corrective commands.[24]

There is almost surely a limitation to the behaviors that particular invariant dynamics are useful for. Motor-cortex activity occupies orthogonal dimensions and shows a different influence on muscle activation during walking and trained forelimb movement[26] and follows different dynamics for reach and grasp movements.[77] Notably, our finding of decaying dynamics for BMI control contrasts with rotational dynamics observed during natural arm movement.[12,13,16,22] We speculate this could be because controlling the BMI relied more on feedback control than a well-trained physical movement, because controlling the BMI did not require the temporal structure of commands needed to control muscles for movement[2] and/or because controlling the BMI did not involve proprioceptive feedback of

physical movement.[35] Recent theoretical work shows that cortico-basal ganglia-thalamic loops can switch between different cortical dynamics useful for different temporal patterns of commands.[46]

The use of invariant dynamics to issue commands has implications for how the brain learns new behavior,[42,78] enabling the brain to leverage pre-existing dynamics for initial learning[25,79,80] and to develop new dynamics through gradual reinforcement.[81,82] This learning, which modifies dynamics, relies on plasticity in cortico-basal ganglia circuits[82–84] and permits the brain to reliably access a particular neural-activity pattern for a given command and movement,[32] even if the same neural-activity pattern is not used to issue the same command across different movements.

Modeling invariant dynamics can inform the design of new neuroprosthetics that can generalize commands to new behaviors[16] and classify entire movement trajectories.[85] We expect that as new behaviors are performed, distinct neural-activity patterns will be used to issue the same command, but that invariant dynamics can predict and thus recognize these distinct neural patterns as signals for the BMI rather than noise. In addition, our results inform the design of rehabilitative therapies to restore dynamics following brain injury or stroke to recover movement.[86,87]

Overall, this study put the output of a neural population into focus, revealing how rules for neural dynamics are used to issue commands and produce different movements. This was achieved by studying the brain as it controlled the very neural activity we recorded. BMI,[42,88–91] especially when combined with technical advances in measuring, modeling, and manipulating activity from defined populations, provides a powerful technique to test emerging hypotheses about how neural circuits generate activity to control behavior.

STAR★METHODS

Detailed methods are provided in the online version of this paper and include the following:

- KEY RESOURCES TABLE
- RESOURCE AVAILABILITY
  - Lead contact
  - Materials availability
  - Data and code availability
- EXPERIMENTAL MODEL AND SUBJECT DETAILS
- METHOD DETAILS
  - Electrophysiology and experimental setup
  - Neuroprosthetic decoding
  - Definition of the command for the BMI
  - Neuroprosthetic tasks
  - Optimal feedback control model and simulation
- QUANTIFICATION AND STATISTICAL ANALYSIS
  - Command discretization for analysis
  - Cursor and command trajectory visualization
  - Matching the condition-pooled distribution
  - Comparing command subtrajectories
  - Behavior-preserving shuffle of activity
  - Analysis of activity issuing a given command
  - Invariant dynamics models
  - Invariant dynamics model characterization
  - Invariant dynamics model predictions
  - Estimation of behavior-encoding models
  - Analysis between pairs of conditions
  - Analysis of Optimal Feedback Control Models
  - Statistics Summary

SUPPLEMENTAL INFORMATION

Supplemental information can be found online at https://doi.org/10.1016/j.cub.2023.06.027.

ACKNOWLEDGMENTS

We thank I. Rodrigues-Vaz, D. Peterka, the Theory Center at the Zuckerman Institute, and I. Papusha for helpful discussions, and the Costa and Carmena labs for their support. This work was supported by NIH NINDS Pathway to Independence Award 1K99NS128250-01 (V.R.A.), BRAIN Initiative National Institute of Mental Health postdoctoral fellowship 1F32MH118714-01 (V.R.A.), NIH Pathway to Independence Award 1K99NS124748-01 (P.K.), BRAIN Initiative National Institute of Mental Health postdoctoral fellowship 1F32MH120891-01 (P.K.), NINDS/NIH BRAIN Initiative U19 NS104649 (R.M.C.), Simons-Emory International Consortium on Motor Control #717104 (R.M.C.), and NINDS/NIH R01 NS106094 (J.M.C.).

AUTHOR CONTRIBUTIONS

V.R.A., P.K., R.M.C., and J.M.C. conceived and designed this study. P.K., S.G., and A.L.O. performed the experiments. P.K. and V.R.A. analyzed the data. All authors contributed materials and analysis tools. V.R.A., P.K., R.M.C., and J.M.C. wrote the manuscript. All authors reviewed the manuscript.

DECLARATION OF INTERESTS

We disclose that we have filed for a patent based on this work.

INCLUSION AND DIVERSITY

We support inclusive, diverse, and equitable conduct of research.

Received: February 22, 2022
Revised: April 24, 2023
Accepted: June 9, 2023
Published: July 3, 2023

REFERENCES

1. Rokni, U., and Sompolinsky, H. (2012). How the brain generates movement. Neural Comput. *24*, 289–331.
2. Churchland, M.M., and Cunningham, J.P. (2014). A dynamical basis set for generating reaches. Cold Spring Harb. Symp. Quant. Biol. *79*, 67–80.
3. Shenoy, K.V., Sahani, M., and Churchland, M.M. (2013). Cortical control of arm movements: a dynamical systems perspective. Annu. Rev. Neurosci. *36*, 337–359.
4. Hennequin, G., Vogels, T.P., and Gerstner, W. (2014). Optimal control of transient dynamics in balanced networks supports generation of complex movements. Neuron *82*, 1394–1406.
5. Sussillo, D., Churchland, M.M., Kaufman, M.T., and Shenoy, K.V. (2015). A neural network that finds a naturalistic solution for the production of muscle activity. Nat. Neurosci. *18*, 1025–1033.
6. Mastrogiuseppe, F., and Ostojic, S. (2018). Linking connectivity, dynamics, and computations in low-rank recurrent neural networks. Neuron *99*, 609–623.e29.
7. Porter, R., and Lemon, R. (1995). Corticospinal Function and Voluntary Movement (Oxford University Press).

8. Nelson, A., Abdelmesih, B., and Costa, R.M. (2021). Corticospinal populations broadcast complex motor signals to coordinated spinal and striatal circuits. Nat. Neurosci. *24*, 1721–1732.
9. Arber, S., and Costa, R.M. (2018). Connecting neuronal circuits for movement. Science *360*, 1403–1404.
10. Arber, S., and Costa, R.M. (2022). Networking brainstem and basal ganglia circuits for movement. Nat. Rev. Neurosci. *23*, 342–360.
11. Russo, A.A., Bittner, S.R., Perkins, S.M., Seely, J.S., London, B.M., Lara, A.H., Miri, A., Marshall, N.J., Kohn, A., Jessell, T.M., et al. (2018). Motor cortex embeds muscle-like commands in an untangled population response. Neuron *97*, 953–966.e8.
12. Churchland, M.M., Cunningham, J.P., Kaufman, M.T., Foster, J.D., Nuyujukian, P., Ryu, S.I., and Shenoy, K.V. (2012). Neural population dynamics during reaching. Nature *487*, 51–56.
13. Michaels, J.A., Dann, B., and Scherberger, H. (2016). Neural population dynamics during reaching are better explained by a dynamical system than representational tuning. PLoS Comput. Biol. *12*, e1005175.
14. Liang, K.-F., and Kao, J.C. (2020). Deep learning neural encoders for motor cortex. IEEE Trans. Bio Med. Eng. *67*, 2145–2158.
15. Truccolo, W., Hochberg, L.R., and Donoghue, J.P. (2010). Collective dynamics in human and monkey sensorimotor cortex: predicting single neuron spikes. Nat. Neurosci. *13*, 105–111.
16. Kao, J.C., Nuyujukian, P., Ryu, S.I., Churchland, M.M., Cunningham, J.P., and Shenoy, K.V. (2015). Single-trial dynamics of motor cortex and their applications to brain-machine interfaces. Nat. Commun. *6*, 7759.
17. Kao, J.C., Ryu, S.I., and Shenoy, K.V. (2017). Leveraging neural dynamics to extend functional lifetime of brain-machine interfaces. Sci. Rep. *7*, 7395.
18. Pandarinath, C., O'Shea, D.J., Collins, J., Jozefowicz, R., Stavisky, S.D., Kao, J.C., Trautmann, E.M., Kaufman, M.T., Ryu, S.I., Hochberg, L.R., et al. (2018). Inferring single-trial neural population dynamics using sequential auto-encoders. Nat. Methods *15*, 805–815.
19. Abbaspourazad, H., Choudhury, M., Wong, Y.T., Pesaran, B., and Shanechi, M.M. (2021). Multiscale low-dimensional motor cortical state dynamics predict naturalistic reach-and-grasp behavior. Nat. Commun. *12*, 607.
20. Gallego-Carracedo, C., Perich, M.G., Chowdhury, R.H., Miller, L.E., and Gallego, J.A. (2022). Local field potentials reflect cortical population dynamics in a region-specific and frequency-dependent manner. eLife *11*, e73155.
21. Gallego, J.A., Perich, M.G., Chowdhury, R.H., Solla, S.A., and Miller, L.E. (2020). Long-term stability of cortical population dynamics underlying consistent behavior. Nat. Neurosci. *23*, 260–270.
22. Sani, O.G., Abbaspourazad, H., Wong, Y.T., Pesaran, B., and Shanechi, M.M. (2021). Modeling behaviorally relevant neural dynamics enabled by preferential subspace identification. Nat. Neurosci. *24*, 140–149.
23. Kaufman, M.T., Churchland, M.M., Ryu, S.I., and Shenoy, K.V. (2014). Cortical activity in the null space: permitting preparation without movement. Nat. Neurosci. *17*, 440–448.
24. Stavisky, S.D., Kao, J.C., Ryu, S.I., and Shenoy, K.V. (2017). Motor cortical visuomotor feedback activity is initially isolated from downstream targets in output-null neural state space dimensions. Neuron *95*, 195–208.e9.
25. Perich, M.G., Gallego, J.A., and Miller, L.E. (2018). A neural population mechanism for rapid learning. Neuron *100*, 964–976.e7.
26. Miri, A., Warriner, C.L., Seely, J.S., Elsayed, G.F., Cunningham, J.P., Churchland, M.M., and Jessell, T.M. (2017). Behaviorally selective engagement of short-latency effector pathways by motor cortex. Neuron *95*, 683–696.e11.
27. Marshall, N.J., Glaser, J.I., Trautmann, E.M., Amematsro, E.A., Perkins, S.M., Shadlen, M.N., Abbott, L.F., Cunningham, J.P., and Churchland, M.M. (2022). Flexible neural control of motor units. Nat. Neurosci. *25*, 1492–1504.
28. Schieber, M.H. (2004). Motor control: basic units of cortical output? Curr. Biol. *14*, R353–R354.
29. Taylor, D.M., Tillery, S.I.H., and Schwartz, A.B. (2002). Direct cortical control of 3D neuroprosthetic devices. Science *296*, 1829–1832.
30. Serruya, M.D., Hatsopoulos, N.G., Paninski, L., Fellows, M.R., and Donoghue, J.P. (2002). Instant neural control of a movement signal. Nature *416*, 141–142.
31. Carmena, J.M., Lebedev, M.A., Crist, R.E., O'Doherty, J.E., Santucci, D.M., Dimitrov, D.F., Patil, P.G., Henriquez, C.S., and Nicolelis, M.A.L. (2003). Learning to control a brain-machine interface for reaching and grasping by primates. PLoS Biol. *1*, E42.
32. Ganguly, K., and Carmena, J.M. (2009). Emergence of a stable cortical map for neuroprosthetic control. PLoS Biol. *7*, e1000153.
33. Elsayed, G.F., Lara, A.H., Kaufman, M.T., Churchland, M.M., and Cunningham, J.P. (2016). Reorganization between preparatory and movement population responses in motor cortex. Nat. Commun. *7*, 13239.
34. Churchland, M.M., Cunningham, J.P., Kaufman, M.T., Ryu, S.I., and Shenoy, K.V. (2010). Cortical preparatory activity: representation of movement or first cog in a dynamical machine? Neuron *68*, 387–400.
35. Kalidindi, H.T., Cross, K.P., Lillicrap, T.P., Omrani, M., Falotico, E., Sabes, P.N., and Scott, S.H. (2021). Rotational dynamics in motor cortex are consistent with a feedback controller. eLife *10*, e67256.
36. Pruszynski, J.A., Kurtzer, I., Nashed, J.Y., Omrani, M., Brouwer, B., and Scott, S.H. (2011). Primary motor cortex underlies multi-joint integration for fast feedback control. Nature *478*, 387–390.
37. Bollu, T., Ito, B.S., Whitehead, S.C., Kardon, B., Redd, J., Liu, M.H., and Goldberg, J.H. (2021). Cortex-dependent corrections as the tongue reaches for and misses targets. Nature *594*, 82–87.
38. Veuthey, T.L., Derosier, K., Kondapavulur, S., and Ganguly, K. (2020). Single-trial cross-area neural population dynamics during long-term skill learning. Nat. Commun. *11*, 4057.
39. Rizzolatti, G., and Luppino, G. (2001). The cortical motor system. Neuron *31*, 889–901.
40. Dum, R.P., and Strick, P.L. (2005). Frontal lobe inputs to the digit representations of the motor areas on the lateral surface of the hemisphere. J. Neurosci. *25*, 1375–1386.
41. Harris, J.A., Mihalas, S., Hirokawa, K.E., Whitesell, J.D., Choi, H., Bernard, A., Bohn, P., Caldejon, S., Casal, L., Cho, A., et al. (2019). Hierarchical organization of cortical and thalamic connectivity. Nature *575*, 195–202.
42. Athalye, V.R., Carmena, J.M., and Costa, R.M. (2020). Neural reinforcement: re-entering and refining neural dynamics leading to desirable outcomes. Curr. Opin. Neurobiol. *60*, 145–154.
43. Sauerbrei, B.A., Guo, J.-Z., Cohen, J.D., Mischiati, M., Guo, W., Kabra, M., Verma, N., Mensh, B., Branson, K., and Hantman, A.W. (2020). Cortical pattern generation during dexterous movement is input-driven. Nature *577*, 386–391.
44. Merel, J., Botvinick, M., and Wayne, G. (2019). Hierarchical motor control in mammals and machines. Nat. Commun. *10*, 5489.
45. Kao, T.-C., Sadabadi, M.S., and Hennequin, G. (2021). Optimal anticipatory control as a theory of motor preparation: A thalamo-cortical circuit model. Neuron *109*, 1567–1581.e12.
46. Logiaco, L., Abbott, L.F., and Escola, S. (2021). Thalamic control of cortical dynamics in a model of flexible motor sequencing. Cell Rep. *35*, 109090.
47. Shanechi, M.M., Orsborn, A.L., and Carmena, J.M. (2016). Robust brain-machine interface design using optimal feedback control modeling and adaptive point process filtering. PLOS Comput. Biol. *12*, e1004730.
48. Shanechi, M.M., Orsborn, A.L., Moorman, H.G., Gowda, S., Dangi, S., and Carmena, J.M. (2017). Rapid control and feedback rates enhance neuroprosthetic control. Nat. Commun. *8*, 13825.
49. Dangi, S., Gowda, S., Moorman, H.G., Orsborn, A.L., So, K., Shanechi, M.M., and Carmena, J.M. (2014). Continuous closed-loop decoder adaptation with a recursive maximum likelihood algorithm allows for rapid

performance acquisition in brain-machine interfaces. Neural Comput. *26*, 1811–1839.

50. Hennig, J.A., Golub, M.D., Lund, P.J., Sadtler, P.T., Oby, E.R., Quick, K.M., Ryu, S.I., Tyler-Kabara, E.C., Batista, A.P., Yu, B.M., et al. (2018). Constraints on neural redundancy. eLife *7*, e36774.
51. Elsayed, G.F., and Cunningham, J.P. (2017). Structure in neural population recordings: an expected byproduct of simpler phenomena? Nat. Neurosci. *20*, 1310–1318.
52. Linderman, S., Johnson, M., Miller, A., Adams, R., Blei, D., and Paninski, L. (2017). Bayesian learning and inference in recurrent switching linear dynamical systems. In Proceedings of the 20th International Conference on Artificial Intelligence and Statistics Proceedings of Machine Learning Research, A. Singh, and J. Zhu, eds., pp. 914–922.
53. Stavisky, S.D., Kao, J.C., Nuyujukian, P., Pandarinath, C., Blabe, C., Ryu, S.I., Hochberg, L.R., Henderson, J.M., and Shenoy, K.V. (2018). Brain-machine interface cursor position only weakly affects monkey and human motor cortical activity in the absence of arm movements. Sci. Rep. *8*, 16357.
54. Biane, J.S., Takashima, Y., Scanziani, M., Conner, J.M., and Tuszynski, M.H. (2016). Thalamocortical projections onto behaviorally relevant neurons exhibit plasticity during adult motor learning. Neuron *89*, 1173–1179.
55. Evarts, E.V. (1968). Relation of pyramidal tract activity to force exerted during voluntary movement. J. Neurophysiol. *31*, 14–27.
56. Kalaska, J.F. (2009). From intention to action: motor cortex and the control of reaching movements. Adv. Exp. Med. Biol. *629*, 139–178.
57. Fetz, E.E. (1992). Are movement parameters recognizably coded in the activity of single neurons? Behav. Brain Sci. *15*, 679–690.
58. Reimer, J., and Hatsopoulos, N.G. (2009). The problem of parametric neural coding in the motor system. Adv. Exp. Med. Biol. *629*, 243–259.
59. Omrani, M., Kaufman, M.T., Hatsopoulos, N.G., and Cheney, P.D. (2017). Perspectives on classical controversies about the motor cortex. J. Neurophysiol. *118*, 1828–1848.
60. Georgopoulos, A.P., Caminiti, R., and Kalaska, J.F. (1984). Static spatial effects in motor cortex and area 5: quantitative relations in a two-dimensional space. Exp. Brain Res. *54*, 446–454.
61. Wang, W., Chan, S.S., Heldman, D.A., and Moran, D.W. (2007). Motor cortical representation of position and velocity during reaching. J. Neurophysiol. *97*, 4258–4270.
62. Paninski, L., Fellows, M.R., Hatsopoulos, N.G., and Donoghue, J.P. (2004). Spatiotemporal tuning of motor cortical neurons for hand position and velocity. J. Neurophysiol. *91*, 515–532.
63. Fu, Q.-G., Suarez, J.I., and Ebner, T.J. (1993). Neuronal specification of direction and distance during reaching movements in the superior precentral premotor area and primary motor cortex of monkeys. J. Neurophysiol. *70*, 2097–2116.
64. Moran, D.W., and Schwartz, A.B. (1999). Motor cortical representation of speed and direction during reaching. J. Neurophysiol. *82*, 2676–2692.
65. Flament, D., and Hore, J. (1988). Relations of motor cortex neural discharge to kinematics of passive and active elbow movements in the monkey. J. Neurophysiol. *60*, 1268–1284.
66. Georgopoulos, A.P., Kalaska, J.F., Caminiti, R., and Massey, J.T. (1982). On the relations between the direction of two-dimensional arm movements and cell discharge in primate motor cortex. J. Neurosci. *2*, 1527–1537.
67. Georgopoulos, A.P., Schwartz, A.B., and Kettner, R.E. (1986). Neuronal population coding of movement direction. Science *233*, 1416–1419.
68. Sergio, L.E., Hamel-Pâquet, C., and Kalaska, J.F. (2005). Motor. J. Neurophysiol. *94*, 2353–2378.
69. Cheney, P.D., and Fetz, E.E. (1980). Functional classes of primate corticomotoneuronal cells and their relation to active force. J. Neurophysiol. *44*, 773–791.
70. Ajemian, R., Green, A., Bullock, D., Sergio, L., Kalaska, J., and Grossberg, S. (2008). Assessing the function of motor cortex: single-neuron models of how neural response is modulated by limb biomechanics. Neuron *58*, 414–428.
71. Overduin, S.A., d'Avella, A., Roh, J., Carmena, J.M., and Bizzi, E. (2015). Representation of muscle synergies in the primate brain. J. Neurosci. *35*, 12615–12624.
72. Holdefer, R.N., and Miller, L.E. (2002). Primary motor cortical neurons encode functional muscle synergies. Exp. Brain Res. *146*, 233–243.
73. Fetz, E.E., and Cheney, P.D. (1980). Postspike facilitation of forelimb muscle activity by primate corticomotoneuronal cells. J. Neurophysiol. *44*, 751–772.
74. Schieber, M.H., and Rivlis, G. (2007). Partial reconstruction of muscle activity from a pruned network of diverse motor cortex neurons. J. Neurophysiol. *97*, 70–82.
75. Morrow, M.M., and Miller, L.E. (2003). Prediction of muscle activity by populations of sequentially recorded primary motor cortex neurons. J. Neurophysiol. *89*, 2279–2288.
76. Todorov, E., and Jordan, M.I. (2002). Optimal feedback control as a theory of motor coordination. Nat. Neurosci. *5*, 1226–1235.
77. Suresh, A.K., Goodman, J.M., Okorokova, E.V., Kaufman, M., Hatsopoulos, N.G., and Bensmaia, S.J. (2020). Neural population dynamics in motor cortex are different for reach and grasp. eLife *9*, e58848.
78. Mannella, F., and Baldassarre, G. (2015). Selection of cortical dynamics for motor behaviour by the basal ganglia. Biol. Cybern. *109*, 575–595.
79. Vyas, S., Even-Chen, N., Stavisky, S.D., Ryu, S.I., Nuyujukian, P., and Shenoy, K.V. (2018). Neural population dynamics underlying motor learning transfer. Neuron *97*, 1177–1186.e3.
80. Sadtler, P.T., Quick, K.M., Golub, M.D., Chase, S.M., Ryu, S.I., Tyler-Kabara, E.C., Yu, B.M., and Batista, A.P. (2014). Neural constraints on learning. Nature *512*, 423–426.
81. Athalye, V.R., Ganguly, K., Costa, R.M., and Carmena, J.M. (2017). Emergence of coordinated neural dynamics underlies neuroprosthetic learning and skillful control. Neuron *93*, 955–970.e5.
82. Athalye, V.R., Santos, F.J., Carmena, J.M., and Costa, R.M. (2018). Evidence for a neural law of effect. Science *359*, 1024–1029.
83. Koralek, A.C., Jin, X., Long, J.D., Costa, R.M., and Carmena, J.M. (2012). Corticostriatal plasticity is necessary for learning intentional neuroprosthetic skills. Nature *483*, 331–335.
84. Neely, R.M., Koralek, A.C., Athalye, V.R., Costa, R.M., and Carmena, J.M. (2018). Volitional modulation of primary visual cortex activity requires the basal ganglia. Neuron *97*, 1356–1368.e4.
85. Willett, F.R., Avansino, D.T., Hochberg, L.R., Henderson, J.M., and Shenoy, K.V. (2021). High-performance brain-to-text communication via handwriting. Nature *593*, 249–254.
86. Khanna, P., Totten, D., Novik, L., Roberts, J., Morecraft, R.J., and Ganguly, K. (2021). Low-frequency stimulation enhances ensemble co-firing and dexterity after stroke. Cell *184*, 912–930.e20.
87. Ramanathan, D.S., Guo, L., Gulati, T., Davidson, G., Hishinuma, A.K., Won, S.J., Knight, R.T., Chang, E.F., Swanson, R.A., and Ganguly, K. (2018). Low-frequency cortical activity is a neuromodulatory target that tracks recovery after stroke. Nat. Med. *24*, 1257–1267.
88. Shenoy, K.V., and Carmena, J.M. (2014). Combining decoder design and neural adaptation in brain-machine interfaces. Neuron *84*, 665–680.
89. Golub, M.D., Chase, S.M., Batista, A.P., and Yu, B.M. (2016). Brain-computer interfaces for dissecting cognitive processes underlying sensorimotor control. Curr. Opin. Neurobiol. *37*, 53–58.
90. Orsborn, A.L., and Pesaran, B. (2017). Parsing learning in networks using brain-machine interfaces. Curr. Opin. Neurobiol. *46*, 76–83.
91. Moxon, K.A., and Foffani, G. (2015). Brain-machine interfaces beyond neuroprosthetics. Neuron *86*, 55–67.

92. Paxinos, G., Huang, X.-F., and Toga, A.W. (2013). The Rhesus Monkey Brain in Stereotaxic Coordinates (Elsevier Academic Press).

93. Gilja, V., Nuyujukian, P., Chestek, C.A., Cunningham, J.P., Yu, B.M., Fan, J.M., Churchland, M.M., Kaufman, M.T., Kao, J.C., Ryu, S.I., et al. (2012). A high-performance neural prosthesis enabled by control algorithm design. Nat. Neurosci. *15*, 1752–1757.

94. Wu, W., Gao, Y., Bienenstock, E., Donoghue, J.P., and Black, M.J. (2006). Bayesian population decoding of motor cortical activity using a Kalman filter. Neural Comput. *18*, 80–118.

95. Dangi, S., Orsborn, A.L., Moorman, H.G., and Carmena, J.M. (2013). Design and analysis of closed-loop decoder adaptation algorithms for brain-machine interfaces. Neural Comput. *25*, 1693–1731.

96. Malik, W.Q., Truccolo, W., Brown, E.N., and Hochberg, L.R. (2011). Efficient decoding with steady-state kalman filter in neural interface systems. IEEE Trans. Neural Syst. Rehabil. Eng. *19*, 25–34.

97. Gowda, S., Orsborn, A.L., Overduin, S.A., Moorman, H.G., and Carmena, J.M. (2014). Designing dynamical properties of brain-machine interfaces to optimize task-specific performance. IEEE Trans. Neural Syst. Rehabil. Eng. *22*, 911–920.

STAR★METHODS

KEY RESOURCES TABLE

REAGENT or RESOURCE	SOURCE	IDENTIFIER
Deposited data		
Neural and behavioral datasets	This paper	https://doi.org/10.48324/dandi.000404/0.230605.2024
Experimental models: Organisms/strains		
Rhesus macaque (macaca mulatta)	California National Primate Center, Davis, CA	N/A
Software and algorithms		
Python 2.7, 3.6	Python Software Foundation	https://www.python.org
ssm – for fitting switching LDS model	Linderman et al.[52]	https://github.com/lindermanlab/ssm
Analysis code	This paper	https://doi.org/10.5281/zenodo.8006653; https://github.com/pkhanna104/bmi_dynamics_code
Other		
128-channel microwire electrode arrays	Innovative Neurophysiology	https://inphysiology.com/

RESOURCE AVAILABILITY

Lead contact

Further information and requests for resources and reagents should be directed to and will be fulfilled by the lead contact, Vivek R. Athalye (va237@columbia.edu).

Materials availability

This study did not generate new unique reagents.

Data and code availability

- Monkey BMI data (binned spike counts, cursor trajectories, condition parameters, decoder parameters, and task parameters) has been deposited in the DANDI Archive (https://doi.org/10.48324/dandi.000404/0.230605.2024) and is publicly available as of the date of publication.
- All original code has been deposited at Zenodo (https://doi.org/10.5281/zenodo.8006653) and at GitHub (https://github.com/pkhanna104/bmi_dynamics_code) and is publicly available as of the date of publication.
- Any additional information required to reanalyze the data reported in this paper is available from the lead contact upon request.

EXPERIMENTAL MODEL AND SUBJECT DETAILS

All training, surgery, and experimental procedures were conducted in accordance with the NIH Guide for the Care and Use of Laboratory Animals and were approved by the University of California Berkeley Institutional Animal Care and Use Committee (IACUC). Two adult male rhesus macaque monkeys (7 years old, monkey G and 10 years old, monkey J) (Macaca mulatta, RRID: NCBI-Taxon:9544) were used as subjects in this study. Prior to this study, Monkeys G and J were trained at arm reaching tasks and spike-based 2D neuroprosthetic cursor tasks for 1.5 years. All animals were housed in pairs.

METHOD DETAILS

Electrophysiology and experimental setup

Two male rhesus macaques were bilaterally, chronically implanted with 16 x 8 arrays of Teflon-coated tungsten microwire electrodes (35 mm in diameter, 500 mm separation between microwires, 6.5 mm length, Innovative Neurophysiology, Durham, NC) in the upper arm area of primary motor cortex (M1) and posterior dorsal premotor cortex (PMd). Localization of target areas was performed using stereotactic coordinates from a neuroanatomical atlas of the rhesus brain.[92] Implant depth was chosen to target layer 5 pyramidal tract neurons and was typically 2.5 - 3 mm, guided by stereotactic coordinates.

During behavioral sessions, neural activity was recorded, filtered, and thresholded using the 128-channel Multichannel Acquisition Processor (Plexon, Dallas, TX) (Monkey J) or the 256-channel Omniplex D Neural Acquisition System (Plexon) (Monkey G). Channel thresholds were manually set at the beginning of each session based on 1–2 min of neural activity recorded as the animal sat quietly (i.e. not performing a behavioral task). Single-unit and multi-unit activity were sorted online after setting channel thresholds. Decoder units were manually selected based on a combination of waveform amplitude, variance, and stability over time.

Neuroprosthetic decoding

Subjects' neural activity controlled a two-dimensional (2D) neuroprosthetic cursor in real-time to perform center-out and obstacle-avoidance tasks. The neuroprosthetic decoder consists of two models:

1) A cursor dynamics model capturing the physics of the cursor's position and velocity.
2) A neural observation model capturing the statistical relationship between neural activity and the cursor.

The neuroprosthetic decoder combines the models optimally to estimate the subjects' intent for the cursor and to correspondingly update the cursor.

Decoder algorithm and calibration – Monkey G

Monkey G used a velocity Kalman filter (KF)[93,94] that uses the following models for cursor state c_t and observed neural activity x_t:

$$c_t = Ac_{t-1} + w_t, w_t \sim N(0, W)$$

$$x_t = Cc_t + q_t, q_t \sim N(0, Q)$$

In the cursor dynamics model, the cursor state $c_t \in R^5$ was a 5-by-1 vector $[pos_x, pox_y vel_x, vel_y, 1]^T$, $A \in R^{5x5}$ captures the physics of cursor position and velocity, and w_t is additive Gaussian noise with covariance $W \in R^{5x5}$ capturing cursor state variance that is not explained by A.

In the neural observation model, neural observation $x_t \in R^N$ was a vector corresponding to spike counts from N units binned at 10 Hz, or 100ms bins. C models a linear relationship between the subjects' neural activity and intended cursor state. The decoder only modeled the statistical relationship between neural activity and intended cursor velocity, so only the columns corresponding to cursor state velocity and the offset (columns 3-5) in C were non-zero. Q is additive Gaussian noise capturing variation in neural activity that is not explained by Cc_t. For Monkey G, 35-151 units were used in the decoder (median 48 units).

In summary, the KF is parameterized by matrices $\{A \in R^{5x5}, W \in R^{5x5}, C \in R^{Nx5}, Q \in R^{NxN}\}$. The KF equations used to update the cursor based on observations of neural activity are defined as in Wu et al.[94]

The KF parameters were defined as follows. For the cursor dynamics model, the A and W matrices were fixed as in previous studies.[95] Specifically, they were:

$$A = \begin{bmatrix} 1 & 0 & 0.1 & 0 & 0 \\ 0 & 1 & 0 & 0.1 & 0 \\ 0 & 0 & 0.8 & 0 & 0 \\ 0 & 0 & 0 & 0.8 & 0 \\ 0 & 0 & 0 & 0 & 1 \end{bmatrix}, W = \begin{bmatrix} 0 & 0 & 0 & 0 & 0 \\ 0 & 0 & 0 & 0 & 0 \\ 0 & 0 & 7 & 0 & 0 \\ 0 & 0 & 0 & 7 & 0 \\ 0 & 0 & 0 & 0 & 0 \end{bmatrix}$$

where units of cursor position were in cm and cursor velocity in cm/sec.

For the neural observation model, the C and Q matrices were initialized from neural and cursor kinematic data collected at the beginning of each experimental session while Monkey G observed 2D cursor movements that moved through either a center-out task or obstacle avoidance task. Maximum likelihood methods were used to fit C and Q.

Next, Monkey G performed a "calibration block" where he performed the center-out or obstacle-avoidance task movements as the newly initialized decoder parameters were continuously calibrated/adapted online ("closed-loop decoder adaptation", or CLDA). This calibration block was performed in order to arrive at parameters that would enable excellent neuroprosthetic performance. Every 100ms, decoder matrices C and Q were adapted using the recursive maximum likelihood CLDA algorithm.[49] Half-life values, defining how quickly C and Q could adapt, were typically 300 sec, and adaptation blocks were performed with a weak, linearly decreasing "assist" (re-defining c_t as a weighted linear combination of user-generated $c_t$and optimal c_t to drive the cursor to the target). Typical assist values at the start of the block were 90% user-generated, 10% optimal and decayed to 100% user-generated, 0% optimal over the course of the block. Following CLDA, decoder parameters were fixed. Then the experiment proceeded with Monkey G performing the center-out and obstacle-avoidance tasks.

Decoder algorithm and calibration – Monkey J

Monkey J used a velocity Point Process Filter (PPF).[47,48] The PPF uses the same cursor dynamics model for cursor state c_t as the KF above, but uses a different neural observations model (a Point Process model rather than a Gaussian model) for the spiking $S_t^{1:N}$ of each of N neurons:

$$c_t = Ac_{t-1} + w_t, w_t \sim N(0, W)$$

$$p\left(S_t^{1:N}\middle|v_t\right) = \prod_{j=1}^{N}\left(\lambda_j\left(t\middle|v_t,\varphi^j\right)\Delta\right)^{S_t^j}\exp\left(-\lambda_j\left(t\middle|v_t,\varphi^j\right)\Delta\right)$$

In the neural observations model, neural observation S_t^j is the j[th] neuron's spiking activity, equal to 1 or 0 depending on whether the j[th] neuron spikes in the interval $(t, t+\Delta)$. We used Δt = 5ms bins since consecutive spikes rarely occurred within 5ms of each other. For Monkey J, 20 or 21 units were used in the decoder (median 20 units). The probability distribution over spiking $p(S_t^{1:N}|v_t)$ was a point process with $\lambda_j(t|v_t,\varphi^j)$ as the j[th] neuron's instantaneous firing rate at time t. $\lambda_j(t|v_t,\varphi^j)$ depended on the intended cursor velocity $v_t \in R^2$ in the two dimensional workspace and the parameters φ^j for how neuron j encodes velocity. $\lambda_j(t|v_t,\varphi^j)$ was modeled as a log-linear function of velocity:

$$\lambda_j\left(t\middle|v_t,\varphi^j\right) = \exp\left(\beta_j + \alpha_j^T v_t\right)$$

where φ^j parameters consist of $\alpha_j \in R^2, \beta_j \in R^1$.

In summary, the PPF is parameterized by $\{A \in R^{5x5}, W \in R^{5x5}, \varphi^{1:N}\}$. The PPF equations used to update the cursor based on observations of neural activity are defined as in Shanechi et al.[48]

The PPF parameters were defined as follows. For the cursor dynamics model, the A and W matrices are defined as:

$$A = \begin{bmatrix} 1 & 0 & 0.005 & 0 & 0 \\ 0 & 1 & 0 & 0.005 & 0 \\ 0 & 0 & 0.989 & 0 & 0 \\ 0 & 0 & 0 & 0.989 & 0 \\ 0 & 0 & 0 & 0 & 1 \end{bmatrix}, W = \begin{bmatrix} 0 & 0 & 0 & 0 & 0 \\ 0 & 0 & 0 & 0 & 0 \\ 0 & 0 & 3.7\times10^{-5} & 0 & 0 \\ 0 & 0 & 0 & 3.7\times10^{-5} & 0 \\ 0 & 0 & 0 & 0 & 0 \end{bmatrix}$$

where units of cursor position were in m and cursor velocity in m/sec.

For the neural observations model, parameters $\varphi^{1:N}$ were initialized from neural and cursor kinematic data collected at the beginning of each experimental session while Monkey J observed 2D cursor movements that moved through a center-out task. Decoder parameters were adapted using CLDA and optimal feedback control intention estimation as outlined in Shanechi et al.[47] Following CLDA, decoder parameters were fixed. Then the experiment proceeded with Monkey J performing the center-out and obstacle-avoidance tasks.

Definition of the command for the BMI

We defined the "command" for the BMI as the direct influence of subjects' neural activity x_t (binned at 100ms) on the cursor. Concretely, in both decoders, the command was a linear transformation of neural activity that we write as Kx_t which updated the cursor velocity.

Command definition – Monkey G

For Monkey G, the update to the cursor state c_t due to cursor dynamics and neural observation x_t can be written as:

$$c_t = F_t c_{t-1} + K_t x_t$$

where $F_t c_{t-1}$ is the update in cursor state due to the cursor dynamics process and $K_t x_t$ is what we have defined as the command: the update in cursor state due to the current neural observation. $K_t \in R^{5xn}$ is the Kalman Gain matrix and $F_t = (I - K_t C)A$. In practice K_t converges to its steady-state form K within a matter of seconds,[96] and thus F_t converges to $F = (I - KC)A$, so we can write the above expression in its steady state form:

$$c_t = Fc_{t-1} + Kx_t$$

In our implementation, the structure of K is such that neural activity x_t directly updates cursor velocity, and velocity integrates to update position. The following technical note explains the structure of K. Due to the form of the A, W matrices, $Rank(K) = 2$. In addition, decoder adaptation imposed the constraint that the intermediate matrix $C^T Q^{-1} C$ was of the form aI, where $a = mean(diag(C^T Q^{-1} C))$. Due to this constraint, the rows of K that update the position of the cursor are equal to the rows of K that update the velocity multiplied by the update timestep: $K(1:2,:) = K(3:4,:) * dt$[97] (see independent velocity control in the reference). Given this structure of K, neural activity's contribution to cursor position is the simple integration of neural activity's contribution to velocity over one timestep.

In summary, since Kx_t reflects the direct effect of the motor cortex units on the velocity of the cursor, we term the velocity components of Kx_t the "command". We analyzed the neural spike counts binned at 100ms that were used online to drive cursor movements with no additional pre-processing.

Command definition – Monkey J

For Monkey J the cursor state updates in time as:

$$c_t = f_t(c_{t-1}) + K_t x_t$$

where

$$f_t(c_{t-1}) = \left(Ac_{t-1} - K_t e^{CAc_{t-1}}\Delta\right), K_t = P_t C$$

Here $f_t(c_{t-1})$ is the cursor dynamics process and $K_t x_t$ is the neural command. $P_t \in R^{5x5}$ is the estimate of cursor state covariance, and $C \in R^{5xN}$ captures how neural activity encodes velocity as a matrix where each column is composed of $[0, 0, \alpha_j^{xvel}, \alpha_j^{yvel}, \beta_j]^T$ for the jth unit.

We define the command for analysis in this study as $K_{est}x_t$, where K_{est} is a time-invariant matrix that almost perfectly approximates K_t. While the PPF's K_t does not necessarily converge in the same way it does in the KF, for all four analyzed sessions, neural activity mapped through $K_{est} \in R^{2xN}$ could account for 99.6, 99.6, 99.5, and 99.8 percent of the variance of the command respectively ($K_t x_t \cong K_{est}x_t$). In addition, due to the accuracy of this linear approximation, we also match Monkey J's timescale of neural activity and commands to that of Monkey G. In order to match timescales across the two animals (Monkey G: 100 ms updates, Monkey J: 5ms updates), Monkey J's commands were aggregated into 100 ms bins by summing $K_{est}x_t$ over 20 consecutive 5ms bins to yield the aggregated command over 100ms. Correspondingly, Monkey J's neural activity was also summed into 100ms bins by summing x_t over 20 consecutive 5ms bins.

Neuroprosthetic tasks

Subjects performed movements in a two-dimensional workspace (Monkey J: 24cm x 24cm, Monkey G: 50cm x 28cm) for two neuroprosthetic tasks: a center-out task and an obstacle-avoidance task. We define the movement "condition" as the task performed ("co" = center-out task, "cw" / "ccw" = clockwise/counterclockwise movement around the obstacle in the obstacle-avoidance task) and the target achieved (numbered 0 through 7). Thus, there were up to 24 different conditions possible (8 center-out conditions, 8 clockwise obstacle-avoidance conditions, 8 counterclockwise obstacle-avoidance conditions). In practice, subjects mostly circumvented the obstacles for a given target location consistently in a clockwise or counterclockwise manner (as illustrated in Figure 1C right) resulting in an average of 16–17 conditions per session.

Center-out task

The center-out task required subjects to hold their cursor within a center target (Monkey J: radius = 1.2 cm, Monkey G: radius = 1.7 cm) for a specified period of time (Monkey J: hold = 0.25 sec, Monkey G: hold = 0.2 sec) before a go cue signaled the subjects to move their cursor to one of eight peripheral targets uniformly spaced around a circle. Each target was equidistant from the center starting target (Monkey J: distance = 6.5cm, Monkey G: distance = 10cm). Subjects then had to position their cursor within the peripheral target (Monkey J: target radius = 1.2cm, Monkey G: target radius = 1.7cm) for a specified period to time (Monkey J: hold = 0.25, Monkey G: hold = 0.2sec). Failure to acquire the target within a specified window (Monkey J: 3-10 sec, Monkey G: 10 sec) or to hold the cursor within the target for the duration of the hold period resulted in an error. Following successful completion of a target, a juice reward was delivered. Monkey J was required to move his cursor back to the center target to initiate a new trial, and Monkey G's cursor was automatically reset to the center target to initiate a new trial.

Obstacle-avoidance task

Monkey G performed an obstacle-avoidance task with a very similar structure to the center-out task. The only difference was that a square obstacle (side length 2 or 3 cm) would appear in the workspace centered exactly in the middle of the straight line connecting the center target position and peripheral target position. If the cursor entered the obstacle, the trial would end in an error, and the trial was repeated.

Monkey J's obstacle-avoidance task required a point-to-point movement between an initial (not necessarily center) target and another target. On arrival at the initial target, an ellipsoid obstacle appeared on the screen. If the cursor entered the obstacle at any time during the movement to the peripheral target, an error resulted, and the trial was repeated. Target positions and obstacle sizes and positions were selected to vary the amount of obstruction, radius of curvature around the obstacles, and spatial locations of targets. Trials were constructed to include the following conditions: no obstruction, partial obstruction with low-curvature, full obstruction with a long distance between targets, and full obstruction with a short distance between targets thus requiring a high curvature. See Shanechi et al.[48] for further details. In this study, only trials that included partial obstruction or full obstruction were analyzed as "obstacle-avoidance" trials.

Number of sessions

We analyzed 9 sessions of data from Monkey G and 4 sessions of data from Monkey J where on each session, monkeys performed both the center-out and obstacle-avoidance tasks with the same decoder. Only successful trials were analyzed.

Optimal feedback control model and simulation

We introduce a model based on optimal feedback control (OFC) for how the brain can use invariant neural population dynamics to control movement based on feedback. From the perspective of the brain trying to control the BMI, we used the model to ask how invariant neural population dynamics affect the brain's control of movement.

Thus, we performed and analyzed simulations of a model in which the brain acts as an optimal linear feedback controller (finite horizon linear quadratic regulator), sending inputs to a neural population so that it performs the center-out and obstacle-avoidance tasks (Figure 6). The feedback controller computed optimal inputs to the neural population based on the current cursor state and current neural population activity. Specifically, the inputs were computed as the solution of an optimization problem that used

knowledge of the target and task, decoder, and the neural population's invariant dynamics. We simulated 20 trials for each of 24 conditions: 8 center-out conditions, 8 clockwise obstacle-avoidance conditions, and 8 counterclockwise obstacle-avoidance conditions. The neural and cursor dynamics processes in the simulation are summarized below:

Neural population dynamics with input

In our simulation, the neural activity of N neurons $x_t \in R^N$ is driven by invariant dynamics $A \in R^{N\times N}$ that act on previous activity x_{t-1}, an activity offset $b \in R^N$, inputs from the feedback controller $u_{t-1} \in R^N$ that are transformed by input matrix $B \in R^{N\times N}$, and noise $\sigma_{t-1} \in R^N$:

$$x_t = Ax_{t-1} + b + Bu_{t-1} + \sigma_{t-1}$$

The input matrix B was set to be the identity matrix such that each neuron has its own independent input. Each neuron also had its own independent, time-invariant noise (see *Noise* section below for how the noise level was set).

For notational convenience, an offset term was appended to x_t: $\begin{bmatrix} x_t \\ 1 \end{bmatrix} \in R^{N+1}$. This enabled incorporating the offset b into the neural dynamics matrix:

$$\begin{bmatrix} x_t \\ 1 \end{bmatrix} = \begin{bmatrix} A & b \\ 0 & 1 \end{bmatrix} \begin{bmatrix} x_{t-1} \\ 1 \end{bmatrix} + \begin{bmatrix} B \\ 0 \end{bmatrix} u_{t-1} + \begin{bmatrix} \sigma_{t-1} \\ 0 \end{bmatrix}$$

BMI cursor dynamics

The cursor update equations for the simulation matched the steady state cursor update equations in the online BMI experiment (see "definition of the command for the BMI" above):

$$c_t = Fc_{t-1} + Kx_{t-1}$$

As in the experiment, cursor state $c_t \in R^{N_c}$ where $N_c = 5$ was a vector consisting of two-dimensional position, velocity, and an offset: $[pos_x, pox_y vel_x, vel_y, 1]^T$. $K \in R^{N_c \times N}$ was the decoder's steady-state Kalman gain (Monkey G) or estimated equivalent K_{est} (Monkey J). $F \in R^{N_c \times N_c}$ was set to the decoder's steady-state cursor dynamics matrix (Monkey G). For Monkey J, F was estimated using the expression for calculating the steady-state cursor dynamics matrix: $F_{est} = (I - K_{est}C_{est}) * A_{100ms}$, where $I \in R^{N_c x N_c}$, $C_{est} \in R^{NxN_c}$ was set using the α, β velocity encoding parameters from the point process filter (see above): $C_{est}(j,:) = [0\ 0\ 0.01 * \alpha_j(1)\ 0.01 * \alpha_j(2)\ 0.01 * \beta_j]$. Values in C_{est} were multiplied by 0.01 to adjust for velocities expressed in units of cm/sec (in the simulation) instead of m/sec (as in PPF). A_{100ms} was set to the same A used by Monkey G so that the cursor dynamics would be appropriate for 100ms timesteps:

$$A_{100ms} = \begin{bmatrix} 1 & 0 & 0.1 & 0 & 0 \\ 0 & 1 & 0 & 0.1 & 0 \\ 0 & 0 & 0.8 & 0 & 0 \\ 0 & 0 & 0 & 0.8 & 0 \\ 0 & 0 & 0 & 0 & 1 \end{bmatrix}$$

Joint dynamics of neural activity and cursor

The feedback controller sent inputs to the neural population which were optimal considering the task goal, the cursor's current state, the neural population's invariant dynamics, and the neural population's current activity. To solve for the optimal input given all the listed quantities, first, the neural and cursor states are jointly defined. We append the cursor state c_t to the neural activity state $\begin{bmatrix} x_t \\ 1 \end{bmatrix}$ to form $z_t \in R^{N+1+N_c}$:

$$z_t = \begin{bmatrix} x_t \\ 1 \\ c_t \end{bmatrix} = \begin{bmatrix} A & b & 0 \\ 0 & 1 & 0 \\ K & 0 & F \end{bmatrix} \begin{bmatrix} x_{t-1} \\ 1 \\ c_{t-1} \end{bmatrix} + \begin{bmatrix} B \\ 0 \\ 0 \end{bmatrix} u_{t-1} + \begin{bmatrix} \sigma_{t-1} \\ 0 \\ 0 \end{bmatrix}$$

In words, this expression defines a linear dynamical system where input u_{t-1} influences only the neural activity x_t, x_t evolves by invariant dynamics A with offset vector b, and x_t drives cursor c_t through the BMI decoder K. Finally, noise σ_{t-1} only influences neural activity x_t (see Noise section below for how the noise level was set).

OFC to reach a target

Our OFC model computes input u_t to the neural population such that the activity of the neural population x_t drives the cursor to achieve the desired final cursor state (i.e. the target) with minimal magnitude of input u_t. Concretely, in the finite horizon LQR model, the optimal control sequence $(u_t, t = 0, 1, \ldots T-1)$ is computed by minimizing the following cost function:

$$J(u_{0:T-1}) = \left(\sum_{t=0}^{T-1} \left((z_t - z_{targ})^T Q (z_t - z_{targ}) + u_t^T R u_t \right) \right) + (z_T - z_{targ})^T Q_T (z_T - z_{targ})$$

In our model, $Q = 0 \in R^{(N+1+N_c)\times(N+1+N_c)}$, $R = I \in R^{N\times N}$, and $Q_T = \begin{bmatrix} 0 \in R^{N\times N} & 0 & 0 \\ 0 & 0 \in R^1 & 0 \\ 0 & 0 & I * 10^2 \in R^{N_c \times N_c} \end{bmatrix} \in R^{(N+1+N_c)\times(N+1+N_c)}$. Thus,

the final cursor state error is penalized, and the magnitude of the input to the neural population u_t is penalized (with setting R as non-zero). Because the magnitude of the input to neural activity is penalized, the controller sends the minimal input to the neural population to produce task behavior. We defined our cost function so that the cursor state during movement before the final cursor state is not penalized, and the neural state is never penalized.

The optimal control sequence $(u_t, t = 0, 1, \ldots T-1)$ is given by $u_t = K_t^{lqr}(z_t - z_{targ})$ where feedback gain matrices $(K_t^{lqr}, t = 0, 1, \ldots T-1)$ are computed iteratively solving the dynamic Ricatti equation backwards in time. We note that we computed the LQR solution for u_t using the dynamics of state error $z_t - z_{targ}$, and that the dynamics of state error for non-zero target states are affine rather than strictly linear.

OFC for center-out task

Center-out task simulations were run with the initial cursor position in the center of the workspace at $c_0 = [0, 0, 0, 0, 1]$ and the target cursor state at $[target_x, target_y, vel_x = 0, vel_y = 0, 1]^T$. Targets were positioned 10cm away from the origin (same target arrangement as Monkey G). Target cursor velocity was set to zero to enforce that the cursor should stop at the desired target location.

Exact decoder parameters from Monkey G and linearized decoder parameters from Monkey J were used (F, K) in simulations. The invariant neural dynamics model parameters (A, b) were varied depending on the simulated experiment (see below). The horizon for each trial to hit its target state was set to be $T = 40$ (corresponding to 4 seconds based on the BMI's timebin of 100ms). Constraining each trial to be equal length facilitated comparison of performance across different simulation experiments. We verified that all of our simulated trials completed their tasks successfully.

OFC for obstacle-avoidance using a heuristic

Obstacle-avoidance task simulations were performed with the same initial and target cursor states as the center-out task, except that the cursor circumvented the obstacle to reach the target in both clockwise and counterclockwise movements. We used a heuristic strategy to direct cursor movements around the obstacle; we defined a waypoint as an intermediate state the cursor had to reach enroute to the final target. The heuristic solution performs optimal control from the start position to the waypoint, and then optimal control from the waypoint to the final target. Importantly, this solution minimizes the amount of input needed to accomplish these goals. We used a heuristic solution because the linear control problem of going from the initial cursor state to the final target cursor state with the constraint of avoiding an obstacle is not a convex optimization problem.

Concretely, for the first segment of the movement, a controller with a horizon T=20 directed the cursor to the waypoint, and then a controller with horizon T=20 directed the cursor from the waypoint to the final target (such that the trial length was matched to the center-out task simulation with T=40).

The waypoint was defined relative to the obstacle position as follows. First the vector between the center target and the obstacle position was determined $(v_{obs,center})$. The $v_{obs,center}$ was then rotated either +90 degrees or -90 degrees corresponding to clockwise and counterclockwise movements. The waypoint position was a 6cm distance in the direction of the rotated vector, from the obstacle center. Finally, the desired velocity vector of the intermediate target was set to be in the direction of $v_{obs,center}$, with a magnitude of 10 cm/s, so that the cursor would be moving in a direction consistent with reaching its final target in the second segment of the movement after the waypoint was reached.

To compute the input u_t to execute these movements, we defined the state error at each time t as $z_{error} = z_{targ} - z_t$, where z_{targ} was the waypoint for the first half of the movement, and z_{targ} was the final target for the second half of the movement. The linear quadratic regulator feedback gain K_t^{lqr} matrices were computed on the appropriate state error dynamics with the shortened horizon T=20.

"Full Dynamics Model" Simulation

Simulations of the "Full Dynamics Model" consisted of OFC with the invariant dynamics parameters (A, b) that were fit on experimentally-recorded neural activity from each subject and session (see "invariant dynamics models" below, under "quantification and statistical analysis"). K_t^{lqr} was computed using these experimentally-observed (A, b) parameters. The initial state of neural activity (i.e. x_t at t=0) was set to the fixed point of the dynamics.

"No Dynamics Model" Simulation

Simulations of the "No Dynamics Model" consisted of OFC with invariant dynamics parameter A set to zero $(A = 0)$. The experimentally-observed offset b was still used from each subject and session. K_t^{lqr} was computed using $A = 0$ and the experimentally-observed b, and thus it was different than in the "Full Dynamics Model." The initial state of neural activity (i.e. x_t at t=0) was set to offset b, the fixed point of dynamics with $A = 0$.

"Decoder-null Dynamics Model" Simulation

Simulations of the "Decoder-null Dynamics Model" consisted of OFC with the experimentally-observed invariant dynamics parameters (A, b) that were restricted to the decoder-null space, i.e. each invariant dynamics model was fit only on the projection of neural activity into the decoder-null space (see "invariant dynamics models" under "quantification and statistical analysis"). K_t^{lqr} was computed using these experimentally-observed decoder-null (A, b) parameters, and thus it was different than in the "Full Dynamics Model." The initial state of neural activity (i.e. x_t at t=0) was set to the fixed point of the decoder-null invariant dynamics.

The "Decoder-null Dynamics Model" was compared to its own "No Dynamics Model", which consisted of OFC with K_t^{lqr} computed using $A = 0$ and the experimentally-observed decoder-null offset b for each subject and session, and thus it was different than in the previously defined models. The initial state of neural activity (i.e. x_t at t=0) was set to the decoder-null offset b, the fixed point of dynamics with $A = 0$.

Noise

In our OFC model, movement errors arise due to noise in the neural activity, and subsequent neural activity issues commands based on feedback to correct these errors. We used two considerations to choose the noise level for neural activity. First, we sought to add a level of neural noise that was comparable to the neural "signal" needed to perform control in the absence of noise. Second, we wanted to add the same level of noise to the dynamics model (either "Full Dynamics Model" or "Decoder-null Dynamics Model") and the corresponding "No Dynamics Model," in order to facilitate comparison.

Thus, we first simulated the "No Dynamics Model" without noise for a single trial for each of 24 conditions, and we calculated a, the average variance of a neuron across time and trials.

Then for our noisy simulations of the "No Dynamics Model" and the corresponding dynamics models, Gaussian noise with zero mean and fixed variance a was added to each neuron at each timestep: $x_t = Ax_{t-1} + Bu_{t-1} + \sigma_{t-1}$, where $\sigma_t \sim N(0, aI)$. Thus, the overall level of added noise (the sum of noise variance over neurons) matched the overall level of signal in the noiseless No Dynamics Model simulation (sum of activity variance over neurons).

We note that our main findings (Figures 6C, 6D, 6G, and 6H) held even with different noise levels.

QUANTIFICATION AND STATISTICAL ANALYSIS

Command discretization for analysis

We sought to analyze the occurrence of the same command across different movements. Commands on individual time points were analyzed as the same command if they fell within the same discretized bin of continuous-valued, two-dimensional command space. All commands from rewarded trials in a given experimental session (including both tasks) were aggregated and discretized into 32 bins. Individual commands were assigned to one of 8 angular bins (bin edges were 22.5, 67.5, 112.5, 157.5, 202.5, 247.5, 292.5, and 337.5 degrees) and one of four magnitude bins. Angular bins were selected such that the straight line from the center to each of the center-out targets bisected each of the angular bins as has been done in previous work[50] (Figure S1A). Magnitude bin edges were selected as the 23.75th, 47.5th, 71.25th, and 95th percentile of the distribution of command magnitudes for that experimental session. Commands falling between the 95th and 100th percentile of magnitude were not analyzed to prevent very infrequent noisy observations from skewing the bin edges for command magnitude.

Conditions that used a command regularly

For each session, the number of times each of the 32 (discretized) commands was used in a given condition was tabulated. If the command was used >= 15 times for that condition within a given session pooling across trials, that condition was counted as using the command regularly and was used in all analyses involving (command, condition) tuples. Commands that were used < 15 times were not used in analysis involving (command, condition) tuples. We note that the main results of the study were not affected by this particular selection. Typically, an individual command is used regularly in 5–10 conditions (distribution shown in Figure S1A).

Cursor and command trajectory visualization

Cursor position subtrajectories

To visualize the cursor position trajectories locally around the occurrence of a given command for each condition, we computed the average position "subtrajectory," which we define as the average trajectory in a window locked to the occurrence of the given command. For each condition, cursor positions from successful trials were aggregated. Cursor position subtrajectories shown in Figure 1F are from representative session 0 from Monkey G. A matrix of x-axis and y-axis position trajectories was formed by extracting a window of -500ms to 500ms (5 previous samples plus 5 proceeding samples) around each occurrence of the given command in a given condition (total of $N_{com\text{-}cond}$ occurrences, yielding a 2 x 11 x $N_{com\text{-}cond}$ matrix). Averaging over the $N_{com\text{-}cond}$ observations yielded a condition-specific command-locked average position subtrajectory (size: 2 x 11) for each condition. If a command fell in the first 500ms or last 500ms of a trial, its occurrence was not included in the subtrajectory calculation. The position subtrajectories were translated such that the occurrence of the given command was set to (0, 0) in the 2D workspace (Figures 1F right and S1C middle).

Command subtrajectories

To visualize trajectories of commands around the occurrence of a given command for each condition (Figure 1G, right), we followed the same procedure as described above for cursor position subtrajectories to tabulate a 2 x 11 x $N_{com\text{-}cond}$ matrix but with x-axis and y-axis commands instead of positions. We note that this matrix consisted of the continuous, two-dimensional velocity values of the commands. Averaging over the $N_{com\text{-}cond}$ observations yielded the average condition-specific command subtrajectory (size: 2 x 11 array), as shown in Figure 1F left for example conditions.

Matching the condition-pooled distribution

In many analyses, data (e.g. neural activity or a command-locked cursor trajectory) associated with a command and a specific condition is compared to data that pools across conditions for that same command (Figures 3, 4, and 5). The distribution of the precise continuous value of the command within the command's bin may systematically differ between condition-specific and condition-pooled datasets, which we refer to as 'within-command-bin differences.' To ensure within-command-bin differences are not the source of significant differences between condition-specific and condition-pooled data associated with a command, we developed a procedure to subselect observations of condition-pooled commands so that the mean of the condition-pooled command

distribution is matched to the mean of the condition-specific command distribution. This procedure ensures that any differences between the condition-specific quantity and condition-pooled quantity are not due to 'within-command-bin differences'. This procedure is performed on all analyses comparing condition-specific data to a condition-pooled distribution of data. The matching procedure is as follows:

1. From the condition-specific distribution, compute the command mean $\mu_{com-cond}$ (size: 2x1) and standard deviation $\sigma_{com-cond}$ (size: 2x1).
2. Compute the deviation of each continuous-valued command observation in the condition-pooled distribution from the condition-specific distribution.
   a. Use the condition-specific distribution's parameters to z-score the condition-pooled distribution's continuous-valued command observations by subtracting $\mu_{com-cond}$ and dividing by $\sigma_{com-cond}$.
   b. Compute the deviation of condition-pooled observations from the condition-specific distribution as the L2-norm of the z-scored value
   c. For indices in the condition-pooled distribution that correspond to data in the condition-specific distribution, over-write the L2-norm of the z-scored values with zeros. This step prevents the condition-pooled distribution from dropping datapoints that are in the condition-specific data, thereby ensuring the condition-pooled distribution contains the condition-specific data.
3. Remove the 5% of condition-pooled observations with the largest deviations
4. Use a Student's t-test to assess if the remaining observations in the condition-pooled distribution are significantly different than the condition-specific distribution for the first and second dimension of the command (two p-values)
5. If both p-values are > 0.05, then the procedure is complete and the remaining observations in the condition-pooled distribution are considered the "command-matched condition-pooled distribution" for a specific command and condition.
6. If either or both p-values are < 0.05, return to step 3 and repeat.

If the condition-pooled distribution cannot be matched to the condition-specific distribution such that the size of the condition-pooled distribution is larger than the condition-specific distribution, the particular command/condition will not be included in the analysis.

Comparing command subtrajectories

To assess whether a command is used within significantly different command subtrajectories in different conditions (Figures S1D and S1E), the following analysis is performed for conditions that have sufficient occurrences of the command (>=15):

1. The condition-specific average command subtrajectory is computed by averaging over $N_{com\text{-}cond}$ single-trial command subtrajectories for the condition, as defined above in "*Command subtrajectories*".
2. The condition-pooled average command subtrajectory is computed: all the single-trial command subtrajectories (N_{com}) are pooled across trials from all conditions that use the given command regularly (command occurs >= 15 times in a session) to create a condition-pooled distribution of single-trial command subtrajectories (a 2 x 11 x N_{com} matrix), which is then averaged to yield the condition-pooled average command subtrajectory (a 2 x 11 matrix).
3. In order to test whether condition-specific average command subtrajectories were significantly different from the condition-pooled average command subtrajectory, a distribution of subtrajectories was created by subsampling the condition-pooled distribution to assess expected variation in subtrajectories due to limited data. Specifically, $N_{com\text{-}cond}$ single-trial command subtrajectories were sampled from a condition-pooled distribution of command subtrajectories that was command-matched to the specific condition (see above, "Matching the condition-pooled distribution"). These $N_{com\text{-}cond}$ samples were then averaged to create a single subtrajectory, representing a plausible condition-specific average subtrajectory under the view that the condition-specific subtrajectories are just subsamples of the condition-pooled subtrajectories. This procedure was repeated 1000 times and used to construct a bootstrapped distribution of 1000 command subtrajectories.
4. This distribution was then used to test whether condition-specific subtrajectories deviated from the condition-pooled subtrajectory more than would be expected by subsampling and averaging the condition-pooled subtrajectory distribution. Specifically, the true condition-specific command subtrajectory distance from the condition-pooled command subtrajectory was computed (L2-norm between condition-specific 2x11 subtrajectory and condition-pooled 2x11 subtrajectory) and compared to the bootstrapped distribution of distances: (L2-norm between each of the 1000 subsampled averaged 2x11 command subtrajectories and the condition-pooled 2x11 command subtrajectory). A p-value for each condition-specific command subtrajectory distance was then derived.

The same analysis is also performed using only the next command following a given command (Figure S1E).

Behavior-preserving shuffle of activity

We shuffled neural activity in a manner that preserved behavior as a control for comparison against the hypothesis that neural activity follows invariant dynamics beyond the structure of behavior. Shuffled datasets preserved the timeseries of discretized commands but shuffled the neural activity that issues these commands. In order to create a shuffle for each animal on each session, all timebins

from all trials from all conditions were collated. The continuous-valued command at each timebin was labeled with its discretized command bin. For each of the 32 discretized command bins, all timebins corresponding to a particular discretized command bin were identified. The neural activity in these identified timebins was then randomly permuted. A complete shuffled dataset was constructed by performing this random permutation for all discretized command bins. This full procedure was repeated 1000 times to yield 1000 shuffled datasets.

Analysis of activity issuing a given command

Condition-specific neural activity distances

For each session, (command, condition) tuples with >= 15 observations were analyzed. For each of these (command, condition) tuples, we analyzed the distance between condition-specific average activity and condition-pooled average activity, both for individual neurons and for the population's activity vector (Figures 3B–3E).

Analysis of individual neurons for a given (command, condition) tuple, given N neurons:

1. Compute the condition-specific average neural activity ($\mu_{com-cond} \in R^N$) as the average neural activity over all observations of the command in the condition.
2. Compute the condition-pooled average activity ($\mu_{com-pool} \in R^N$) as the average neural activity over observations of the command pooling across conditions. The command-matching procedure is used to form the condition-pooled dataset to account for within-command-bin differences (see "matching the condition-pooled distribution" above).
3. Compute the absolute value of the difference between the condition-specific and condition-pooled averages: $d\mu_{com-cond} = abs(\mu_{com-cond} - \mu_{com-pool}) \in R^N$.
4. Repeat steps 1-3 for each shuffled dataset i, yielding $d\mu_{shuff-i-com-cond}$ for i = 1:1000.
5. For each neuron j, compare $d\mu_{com-cond}(j)$to the distribution of $d\mu_{shuff-i-com-cond}(j)$for i = 1:1000. Distances greater than the 95th percentile of the shuffled distribution are deemed to have significantly different neuron j activity for a command-condition.

Analysis of population activity for a given (command, condition) tuple:

To compute population distances, one extra step was performed. We sought to ensure that the distances we calculated were not trivially due to "within-bin differences" between the condition-specific and condition-pooled distributions. The first step to ensure this was described above in "matching the condition-pooled distribution". The second step was to only compute distances in the dimensions of neural activity that are null to the decoder and do not affect the composition of the command. Thus, any subtle remaining differences in the distribution of commands would not influence population distances.

To compute distances in the dimensions of neural activity null to the decoder, we computed an orthonormal basis of the null space of decoder matrix $K \in R^{2xN}$ using scipy.linalg.null_space, yielding $V_{null} \in R^{NxN-2}$. The columns of V correspond to basis vectors spanning the $N-2$ dimensional null space. Using V_{null} we computed: $\mu_{com-cond-null} = V_{null}' * \mu_{com-cond}$ and $\mu_{com-pool-null} = V_{null}' * \mu_{com-pool}$. We then calculated the population distance metric (L2-norm), normalized by the square-root of the number of neurons: $d\mu_{pop-com-cond} = /\sqrt[2]{N}, d\mu_{pop-com-cond} \in R^1$.In step 5, the single value $d\mu_{pop-com-cond}$ is compared to the distribution of $d\mu_{shuff-i-pop-com-cond}$ for i = 1:1000 to derive a p-value for each (command, condition) tuple. The fraction of (command, condition) tuples with population activity distances greater than the 95th percentile of the shuffle data (i.e. significant) is reported in Figure 3E.

For visualization of distances relative to the shuffle distribution (Figures 3B–3D), we divided the observed population distance for each (command, condition) tuple by the mean of the corresponding shuffle distribution. With this normalization, we can visualize the spread of the shuffle distribution (Figure 3B, right) and we can interpret a normalized distance of 1 as the expected distance according to the shuffle distribution.

Activity distances pooling over conditions

To test whether condition-specific neural activity for a given command significantly deviated from condition-pooled neural activity for the given command (Figure 3E, middle), we aggregated the distance between condition-specific and condition-pooled average activity over all *Ncond* conditions in which the command was used (>= 15 occurrences of the command in a condition). An aggregate command distance is computed: $d\mu_{pop-com} = \frac{1}{Ncond}\sum_{j=1}^{Ncond} d\mu_{pop-com-j}$, and an aggregate shuffle distribution is computed: $d\mu_{shuff-i-pop-com} = \frac{1}{Ncond}\sum_{j=1}^{Ncond} d\mu_{shuff-i-pop-com-j}$. Then, $d\mu_{pop-com}$ is compared to the distribution of $d\mu_{shuff-i-pop-com}$ for i = 1:1000 to derive a p-value for each command. The fraction of commands with significant population activity distances is reported in Figure 3E, middle.

Single neuron distances

To test whether an individual neuron's condition-specific activity deviated from condition-pooled activity (Figure 3E right), we aggregated the distances between condition-specific and condition-pooled average activity over the C (command, condition) tuples with at least 15 observations. The aggregated distance for neuron n was computed: $d\mu(n) = \frac{1}{C}\sum_{c=1}^{C} d\mu_c(n)$ where $d\mu_c(n)$ is the condition-specific absolute difference for the nth neuron and cth (command, condition) tuple. Then $d\mu(n)$ was compared to the distribution of the aggregated shuffle: $d\mu_{shuff-i}(n) = \frac{1}{C}\sum_{c=1}^{C} d\mu_{shuff-i-c}(n)$ for i = 1:1000 to derive a p-value for each neuron. The fraction of neurons with significant activity distances (p-value<0.05) is reported in Figure 3E right.

Neural activity distances summary

Single neuron activity distances reported in Figure S2B (left) are for all (command, condition, neuron) tuples that had at least 15 observations. We report distances as a z-score of shuffle distribution: $z_{com-cond}(n) = \frac{(d\mu_{com-cond}(n) - mean(d\mu_{shuff-i}(n),\ i = 1{:}1000))}{std(d\mu_{shuff-i}(n),\ i = 1{:}1000)}$.

Single neuron activity distances reported in (Figure S2B center, right) are for (command, condition, neuron) tuples that significantly deviated from shuffle. We report raw distances in neuron activity as $d\mu_{com-cond}(n)$ (Figure S2B, center), and fraction distances as $\frac{d\mu_{com-cond}(n)}{\mu_{com-pool}(n)}$ (Figure S2B, right).

Population activity distances reported in Figures 3B–3D and S2C left are for all (command, condition) tuples. We report distances in population activity as a fraction of shuffle mean: $d\mu_{pop-com-cond}/mean(d\mu_{shuff-i},\ i = 1{:}1000)$(Figures 3B–3D), and as a z-score of shuffle distribution: $z_{pop-com-cond} = \frac{(\mu_{pop-com-cond} - mean(d\mu_{shuff-i},\ i = 1{:}1000))}{std(d\mu_{shuff-i},\ i = 1{:}1000)}$(Figure S2C left).

Population activity distances reported in Figure S2C (center, right) are for (command, condition) tuples that significantly deviated from shuffle. We report distances in population activity as a fraction of shuffle mean $d\mu_{pop-com-cond}/mean(d\mu_{shuff-i},\ i = 1{:}1000)$(Figure S2C, center) and fraction of condition-pooled activity as $\frac{d\mu_{pop-out-cond}}{\|\mu_{com-pool}\|_2}$ (Figure S2C, right).

Invariant dynamics models

In order to test whether invariant dynamics predicts the different neural activity patterns issuing the same command for different conditions, a linear model was fit for each experimental session on training data of neural activity from all conditions and assessed on held-out test data. Neural activity at time t, x_t, was modeled as a linear function of x_{t-1}:

$$x_t = Ax_{t-1} + b$$

Here $A \in R^{NxN}$ modeled invariant dynamics and $b \in R^N$ was an offset vector that allowed the model to identify non-zero fixed points of neural dynamics. Ridge regression was used to estimate the A and b parameters. Prior to any training or testing, data was collated such that all neural activity in bins from t=2:T_{trl} in all rewarded trials were paired with neural activity from t=1:(T_{trl}-1), where T_{trl} is the number of time samples in a trial.

Estimation of Ridge Parameter

For each experimental session, data collated from all conditions was randomly split into 5 sections, and a Ridge model (sklearn.linear_model.Ridge) with a ridge parameter varying from $2.5x10^{-5}$ to 10^6 was trained using 4 of the 5 sections and tested on the remaining test section. Test sections were rotated, yielding five estimates of the coefficient of determination (R^2) for each ridge parameter. The ridge parameter yielding the highest cross-validated mean R^2 was selected for each experimental session. Ridge regression was used primarily due to a subset of sessions with a very high number of units (148 and 151 units), thus a high number of parameters needed to be estimated for the A matrix. Without regularization, these parameters tended to extreme values, and the model generalized poorly.

Invariant dynamics model: fitting and testing

Once a ridge parameter for a given experimental session was identified, A, b were again trained using 4/5 of the data. The remaining test data was predicted using the fit A, b. This procedure was repeated, rotating the training and testing data such that after five iterations, all data points in the experimental session had been in the test data section for one iteration of model-fitting. The predictions made on the held-out test data were collated together into a full dataset. Predictions were then analyzed in subsequent analyses.

Generalization of invariant dynamics

We assessed how well invariant dynamics generalized when certain categories of neural activity were not included in the training data. Invariant dynamics models were estimated after excluding neural activity in the following categories (Figures 4C, 5C, 5E, and S4):

1. Left-out Command: For each command (total of 32 command bins), training data sets were constructed leaving out neural activity that issued the command (Figures 4C, 5C, 5E, and S4).
2. Left-out Condition: For each condition (consisting of target, task, and clockwise or counterclockwise movement for obstacle avoidance), training data sets were constructed leaving out neural activity for the given condition (Figures 4C, 5C, 5E, and S4).
3. Left-out Command Angle: For each command angular bin (total of 8 angular bins), training data sets were constructed leaving out neural activity that issued commands in the given angular bin. This corresponds to leaving out neural activity for the 4 command bins that have the given angular bin but different magnitude bins (Figure S4B, middle).
4. Left-out Command Magnitude: For each command magnitude bin (total of 4 magnitude bins), training data sets were constructed leaving out neural activity that issued commands of the given command magnitude. This corresponds to leaving out neural activity for the 8 command bins that have the given magnitude bin but different angle bins (Figure S4B, right).
5. Left-out Classes of Conditions (Figure S4G):
   a. vertical condition class consisting of conditions with targets located at 90 and 270 degrees for both tasks,
   b. horizontal condition class consisting of conditions with targets located at 0 and 180 degrees for both tasks,
   c. diagonal 1 condition class consisting of conditions with targets located at 45 and 215 degrees for both tasks, and
   d. diagonal 2 condition class consisting of conditions with targets located at 135 and 315 degrees for both tasks.

For each of the listed categories above, many dynamics models were computed – each one corresponding to the exclusion of one element of the category (i.e. one model per: command left-out, condition left-out, command angle left-out, command magnitude left-out, and class of conditions left-out). Each of the trained models was then used to predict the left-out data. Predictions were aggregated across all dynamics models resulting in a full dataset of predictions. The coefficient of determination (R^2) of this predicted dataset reflected how well dynamics models could generalize to types of neural activity that were not observed during training. We note that Monkey J did not perform all conditions in the "diagonal 2" class, and so was not used in the analysis predicting excluded "diagonal 2" conditions.

Decoder-null dynamics model

As an additional comparison, we modeled invariant dynamics that lie only within the decoder-null space (the neural activity subspace that was orthogonal to the decoder such that variation of neural activity in this space has no effect on the decoder's output, i.e. commands for movement).

Our approach was to project spiking activity into the decoder null space, and then fit invariant dynamics on the projected, decoder-null spiking activity. We first computed an orthonormal basis of the null space of decoder matrix $K \in R^{2xN}$ using scipy.linalg.null_space, yielding $V_{null} \in R^{NxN-2}$. The columns of V correspond to basis vectors spanning the $N-2$ dimensional null space. We then computed the projection matrix $P_{null} \in R^{NxN}$ where $P_{null} = V_{null}V_{null}^T$. Spiking activity was then projected into the null space $x_t^{null} = P_{null}x_t$, where $x_t^{null} \in R^{Nx1}$.

Following the above procedure (see "estimation of ridge parameter"), a ridge regression parameter was selected using projected data x_t^{null}. Decoder-null dynamics model parameters A_{null}, b_{null} were then fit on 4/5 of the dataset and then tested on the remaining 1/5 of the x_t^{null} dataset. As before, the training/testing procedure was repeated 5 times such that all data points fell into the test dataset once. Predictions of test data from all five repetitions were collated into one full dataset of predictions. We note that the average of the decoder-space activity across the entire session $\hat{x}^{decoder} = \frac{1}{T}\sum_{t=1}^{T} x_t^{decoder}$, where T is the number of bins in an entire session, was added to all predictions of decoder-null dynamics ($x_{t+1} = A_{null}x_t + b_{null} + \hat{x}^{decoder}$).

Shuffle dynamics model

The invariant dynamics model was compared to a shuffle dynamics model fit on shuffled data (see "behavior-preserving shuffle of activity" above). Following the above procedure (see "estimation of ridge parameter"), a ridge parameter was selected using shuffled data. Shuffle dynamics model parameters $A_{shuffle}$, $b_{shuffle}$ were then fit on 4/5 of the dataset using shuffled data and then tested on the remaining 1/5 of the dataset using original, unshuffled data.

Invariant dynamics model characterization

Dimensionality and eigenvalues

Once the linear invariant dynamics model's parameters A, b were estimated, A was analyzed to assess which modes of dynamics[16] were present (Figure S3). The eigenvalues of A were computed. From each eigenvalue, an oscillation frequency and time decay value were computed using the following equations:

$$\text{Frequency} = \angle\lambda/(2\pi\Delta t)\ \text{Hz if } \lambda \text{ is complex, else frequency} = 0\ \text{Hz}$$

$$\text{Time Decay} = \frac{-1}{\ln(|\lambda|)}\Delta t\ \text{sec}$$

Modes of dynamics contributing substantially to predicting future neural variance will have time decays greater than the BMI decoder's binsize (here, 100ms). 2-4 such dimensions of dynamics were found across sessions and subjects (Figure S3).

Invariant dynamics model predictions

Predicting next neural activity: $x_{t+1} | x_t, A, b$

In Figure 5C, we predict next activity x_{t+1} based on current activity x_t by taking the expected value according to our model: $E(x_{t+1}|x_t, A, b) = Ax_t + b$.

In Figure 5D, we evaluated this prediction for individual dimensions of neural activity.

We projected the prediction of x_{t+1} onto each eigenvector of the dynamics model A matrix and evaluated how well that dimension was predicted (via coefficient of determination).

In Figures S3E and S3G, we evaluated this prediction across time from the start of trial. The magnitude (i.e. L2 norm) of the model residual $\|x_{t+1} - Ax_t + b\|_2$ (Figure S3E) and the coefficient of determination (R^2) (Figure S3G) are plotted for each time point from trial start, evaluated on held-out test data pooling across trials.

Predicting next command: $\text{command}_{t+1} | x_t, A, b, K$

In Figures 5E–5H, we predict the next command command_{t+1} based on current neural activity x_t by taking its expected value according to our model: $E(\text{command}_{t+1} | x_t, A, b, K) = K(Ax_t + b)$, where the decoder matrix K maps between neural activity and the command. This amounts to first predicting next activity based on current activity as above $E(x_{t+1}|x_t, A, b) = Ax_t + b$ and then applying decoder K.

Predicting activity issuing a given command

In Figures 4C–4G, we predict current activity x_t not only with knowledge of previous activity x_{t-1}, but also with knowledge of the current command command$_t$ ($x_t|\, x_{t-1}, A, b, K,$ command$_t$). We modeled x_t and x_{t-1} as jointly Gaussian with our dynamics model, and command$_t$ is jointly Gaussian with them since command$_t = Kx_t$. We modify our prediction of x_t based on knowledge of command$_t$: $E(x_t|x_{t-1}, A, b, K,$ command$_t)$. Explicitly we conditioned on command$_t$, thereby ensuring that $K * E(x_t|x_{t-1}, A, b, K,$ command$_t) =$ command$_t$. To do this we wrote the joint distribution of x_t and command$_t$:

$$\begin{matrix} x_t \\ Kx_t \end{matrix} \sim N\left(\begin{pmatrix} \mu \\ K\mu \end{pmatrix}, \begin{pmatrix} \Sigma & (K\Sigma)^T \\ K\Sigma & K\Sigma K^T \end{pmatrix}\right)$$

where $\mu = E(x_t|x_{t-1}, A, b) = Ax_{t-1} + b$, and $\Sigma = cov[x_t - (Ax_{t-1} + b)]$ is the covariance of the noise in the dynamics model. Then, the multivariate Gaussian conditional distribution provides the solution to conditioning on command$_t$:

$$E(x_t|x_{t-1}, A, b, \mathrm{K}, \text{command}_t) = Ax_{t-1} + b + \Sigma^T K^T \left(K\Sigma K^T\right)^{-1} (\text{command}_t - K(Ax_{t-1} + b))$$

This prediction constrains the prediction of x_t to produce the given command command$_t$.

For these predictions, Σ is estimated following dynamics model fitting and set to the empirical error covariance between estimates of $E(x_t) = Ax_{t-1} + b$ and true x_t in the training data.

Predicting current activity only with command

In Figures 4C–4E, as a comparison to the dynamics prediction ($x_t|\, x_{t-1}, A, b, K,$ command$_t$), we predict x_t as its expected value ($x_t|\, K,$ command$_t$)based only on the command command$_t = Kx_t$ it issues and the decoder matrix K. The same approach was used as above, except with empirical estimates of μ, Σ corresponding to the mean and covariance of the neural data instead of using the neural dynamics model and x_{t-1} to compute μ, Σ.

$$\begin{matrix} x_t \\ Kx_t \end{matrix} \sim N\left(\begin{pmatrix} \mu \\ K\mu \end{pmatrix}, \begin{pmatrix} \Sigma & (K\Sigma)^T \\ K\Sigma & K\Sigma K^T \end{pmatrix}\right)$$

This formulation makes the prediction:

$$E(x_t|\mathrm{K}, \text{command}_t) = \mu + \Sigma^T K^T \left(K\Sigma K^T\right)^{-1} (\text{command}_t - K\mu)$$

Comparing invariant dynamics to shuffle

For the above predictions, we evaluated if invariant dynamics models were more accurate than shuffle dynamics. A distribution of shuffle dynamics R^2 values (coefficient of determination) was generated by computing one R^2 value per shuffled dataset (see "behavior-preserving shuffle of activity" above), where $R^2_{shuffle,i,j}$ corresponds to the R^2 for shuffle dataset i on session j. For each session j, each invariant dynamics model was considered significant if its R^2 was greater than 95% of shuffle R^2 values. To aggregate over S sessions, the R^2 values for all S sessions were averaged yielding one R^2_{avg} value. This averaged value was compared to a distribution of averaged shuffle R^2 values. Specifically, for each shuffle i (i=1:1000 shuffled dataset) an averaged R^2 value was computed across all S sessions: $R^2_{avg,shuffle,i} = \frac{1}{S}\sum_{j=1}^{S} R^2_{shuffle,i,j}$, yielding a distribution of averaged shuffle R^2 values.

Predicting condition-specific activity

The invariant dynamics model was used to predict the condition-specific average activity for a given command ($\mu_{com-cond}$, i.e. the average neural activity over all observations of the command in the condition, see "analysis of activity issuing a given command" above) (Figures 4D–4G). The invariant dynamics model prediction ($\widehat{\mu_{com-cond}}$) was computed as $E(x_t|x_{t-1}, A, b, K,$ command$_t)$ (see "predicting activity issuing a given command" above) averaged over all observations of neural activity for the given command and condition.

To test if the invariant dynamics prediction was significantly more accurate than the shuffle dynamics model (i.e. the dynamics model fit on shuffled data, see "shuffle dynamics model" above) prediction, we computed the error as the distance between true ($\mu_{com-cond}$) and predicted ($\widehat{\mu_{com-cond}}$) condition-specific average activity (single neuron error and population distance). Note that population distances for true and predicted activity were taken only in the dimensions null to the decoder (see "condition-specific neural activity deviation"). The invariant dynamics model was deemed significantly more accurate than shuffle dynamics if the error was less than the 5th percentile of the distribution of the errors from shuffle dynamics models. We reported the fraction of (command, condition) tuples that were individually significant relative to shuffle (Figure 4G, left). We determined whether commands were individually significant relative to shuffle by analyzing the average population activity error across conditions (Figure 4G, middle). We determined whether neurons were individually significant relative to shuffle by analyzing the average single-neuron error over (command, condition) tuples (Figure 4G, right).

Predicting condition-specific component

The component of neural activity for a given command that was specific to a condition was calculated as $\mu_{com-cond} - E(x^t_{com-cond}|\mathrm{K}, \text{command}_t)$, where $\mu_{com-cond}$ is neural activity averaged over observations for the given command and condition, and $E(x^t_{com-cond}|\mathrm{K}, \text{command}_t)$ is the prediction of neural activity only given the command it issued, averaged over observations for the (command, condition) tuple (see "predicting current activity only with command" above). Thus, $\mu_{com-cond} - E(x^t_{com-cond}|\mathrm{K}, \text{command}_t)$ estimates the portion of neural activity that cannot be explained by just knowing the command issued.

We analyzed how well this condition-specific component could be predicted with invariant dynamics as: $\widehat{\mu_{com-cond}} - E(x^t_{com-cond}|\mathrm{K}, \mathrm{command}_t)$ (see "Predicting condition-specific activity" above for calculation of $\widehat{\mu_{com-cond}}$). The variance of $\mu_{com-cond} - E(x^t_{com-cond}|\mathrm{K}, \mathrm{command}_t)$ explained by $\widehat{\mu_{com-cond}} - E(x^t_{com-cond}|\mathrm{K}, \mathrm{command}_t)$ is reported in Figure 4F.

Predicting condition-specific next command

For each (command, condition) tuple, the average "next command" $\mathrm{command}_{com-cond}$ was calculated. For every observation of the given command in the given condition, we took the command at the time step immediately following the given command and averaged over observations. We then analyzed how well invariant dynamics predicted this average "next command" $\widehat{\mathrm{command}}_{com-cond}$, calculated as $E(\mathrm{command}_{t+1}|\, x_t, A, b, K)$ averaged over all observations of neural activity x_t for the given command and condition. The L2-norm of the difference $\mathrm{command}_{com-cond} - \widehat{\mathrm{command}}_{com-cond}$ was computed and compared to the errors obtained from the shuffled-dynamics predictions. For each (command, condition) tuple, the dynamics-predicted "next command" was deemed significantly more accurate than shuffle dynamics if the error was less than the 5th percentile of the distribution of the errors of the shuffled-dynamics predictions (Figure 5F, left). Commands were determined to be individually significant if the error averaged over conditions was significantly less than the shuffled-dynamics error averaged over conditions (Figure 5F, right).

Analysis of predicted command angle

We sought to further analyze whether invariant dynamics predicted the transition from a given command to different "next commands" in different movements. Thus, we calculated two additional metrics on the direction of the predicted "next command", i.e. the angle of the predicted "next command" $\widehat{\mathrm{command}}_{com-cond}$ with respect to the condition-pooled "next command" $\mathrm{command}_{com-pool}$ (the average "next command" following a given command when pooling over conditions).

First, we predicted whether a condition's "next command" would rotate clockwise or counterclockwise relative to the condition-pooled "next command." Specifically, we calculated whether the sign of the cross-product between $\widehat{\mathrm{command}}_{com-cond}$ and $\mathrm{command}_{com-pool}$ matched the sign of the cross-product between $\mathrm{command}_{com-cond}$ and $\mathrm{command}_{com-pool}$. The fraction of (command, conditions) that were correctly predicted (clockwise vs counterclockwise) was compared to the fraction of (command, condition) tuples correctly predicted in the shuffle distribution (Figure 5H, left).

Second, we calculated the absolute error of the angle between the predicted "next command" and the condition-pooled "next command" for each (command, condition) tuple:

$$\mathrm{abs}(\angle(\widehat{\mathrm{command}}_{com-cond}, \mathrm{command}_{com-pool}) - \angle(\mathrm{command}_{com-cond}, \mathrm{command}_{com-pool}))$$

Explicitly, for each (command, condition) tuple, we calculated the absolute difference between two angles: 1) the angle between the predicted "next command" and the condition-pooled "next command" and 2) the angle between the true "next command" and the condition-pooled "next command". These errors were then compared to the shuffle distribution (Figure 5H, right).

Estimation of behavior-encoding models

To compare invariant dynamics models to models in which neural activity encodes behavioral variables in addition to the command, we fit a series of behavior-encoding models (Figure S5). Regressors included cursor state (position, velocity), target position (x,y postion in cursor workspace), and a categorical variable encoding target number (0–7) and task ("center-out", "clockwise obstacle-avoidance", or "counter-clockwise obstacle-avoidance").

Models were fit using Ridge regression following the same procedure described above (see "estimation of Ridge parameter") was followed with one additional step: prior to estimating the ridge parameter or fitting the regression, variables were z-scored. Without z-scoring, ridge regression may favor giving explanatory power to the variables with larger variances, since they would require smaller weights which ridge regression prefers. Then, as above, models were fit using 4/5 of the data and then used to predict the held-out 1/5 of data. After 5 rotations of training and testing data, a full predicted dataset was collated.

We then tested whether invariant neural dynamics improved the prediction of neural activity beyond behavior-encoding. The coefficient of determination (R^2) of the model containing all regressors except previous neural activity was compared to the R^2 of the model containing all regressors plus previous neural activity (Figure S5B) using a paired Student's t-test where session was paired. One test was done for each monkey.

Analysis between pairs of conditions

We sought to assess whether the invariant dynamics model predicted the relationship between pairs of conditions for neural activity and behavior (Figure S6).

Average neural activity for a given command

The invariant dynamics model was used to predict the distance between average neural activity patterns for the same command across pairs of conditions. Concretely, the predicted distance was simply the distance between the predicted neural activity pattern for condition 1 and for condition 2. The correlation between the true distance and the predicted distance was reported for individual neurons (Figures S6A and S6C) and population activity (Figures S6B and S6D). The Wald test (implemented in scipy.stats.linregress) was used to assess the significance of the correlations on single sessions. To assess significance pooled over sessions, data points (true distances vs. dynamics model predicted distances) were aggregated across sessions and assessed for significance.

Average next command

The invariant dynamics model was used to predict the distance between "next commands" for the same given command across pairs of conditions. Concretely, the predicted distance was simply the distance between the predicted "next command" for condition 1 and for condition 2. The correlation between the true distance and the predicted distance was reported (Figures S6J and S6K). As above, the Wald test was used to assess significance of correlations on single sessions and over pooled sessions.

Correlating neural distance with behavior

We asked whether neural activity for a given command was more similar across conditions with more similar command subtrajectories (see "command subtrajectories") (Figure S6E), and whether invariant dynamics predict this. Specifically, we analyzed whether the distance between average neural activity across two conditions for a given command correlated to the distance between command subtrajectories for the same two conditions (Figures S6F top, S6G left, and S6H left). Further, we analyzed whether invariant dynamics predicted this correlation (Figures S6F bottom, S6G right, and S6H right). For every command (that was used in more than five conditions) and pair of conditions that used the command (>=15 observations in each condition in the pair), 1) the distances between condition-specific average activity were computed and 2) distances between command subtrajectories were computed. The neural activity distances were correlated with the command subtrajectory distances (Figures S6F top, S6G left, and S6H left). To assess whether invariant dynamics made predictions that maintained this structure, we performed that same analysis with distances between dynamics-predicted condition-specific average activity across pairs of conditions (Figures S6F bottom, S6G right, and S6H right).

We assessed the significance of the relationship using a linear mixed effects (LME) model (statsmodels.formula.api.mixedlm). The LME modeled command as a random effect because the exact parameters of the increasing linear relationship between command subtrajectories and population activity may vary depending on command. Individual sessions were assessed for significance. To assess significance across sessions, data points were aggregated over sessions, and the LME model used command and session ID as random effects.

Analysis of Optimal Feedback Control Models

Input magnitude

For each simulated trial, we computed the magnitude of input to the neural population as the L2 norm of the input matrix $u_t \in R^{N \times T}$ (where N is the number of neurons and $T = 40$ was the horizon and thus movement length). For each of the 24 conditions, we calculated the average input magnitude over the 20 trials. We compared the magnitude of input used by the Invariant Dynamics Model and the No Dynamics Model, where the Invariant Dynamics Model was either the Full Dynamics Model (Figure 6C) or the Decoder-Null Dynamics Model (Figure 6D). We analyzed each individual session with a paired Wilcoxon signed-rank test, where each pair within a session consisted of one condition (24 conditions total). We aggregated across sessions for each subject using a linear mixed effect (LME) model between input magnitude and model category (Invariant Dynamics Model or No Dynamics Model), with session modeled as a random effect.

Simulated activity issuing a given command

In the OFC simulations, we sought to verify if different neural activity patterns were used to issue the same command across different conditions, applying analyses that we used on experimental neural data to the OFC simulations. As above, we defined discretized command bins (see "command discretization for analysis") and calculated the average neural activity for each (command, condition) tuple. For (command, condition) tuples with >=15 observations (example shown in Figure 6E), we computed the distance between condition-specific average activity and condition-pooled average activity by subtracting the activity, projecting into the decoder-null space, taking the L2 norm, and normalizing by the square root of the number of neurons, as in the experimental data analysis (see "analysis of activity issuing a given command").

We analyzed the distance between condition-specific average activity and condition-pooled average activity for a given command, comparing each model to its own shuffle distribution (see "behavior-preserving shuffle of activity") (Figures 6G and 6H). Concretely, for each simulated session, we calculated the mean of the shuffle distribution of distances for each (command, condition) tuple and compared these shuffle means (one per (command, condition) tuple) to the observed distances from the simulations. We analyzed individual sessions with a Mann-Whitney U test. We aggregated across sessions for each subject with a LME model between activity distance and data source (OFC Simulation vs shuffle), with session modeled as a random effect. For visualization of distances relative to the shuffle distribution (Figures 6F–6H), we divided the observed distance for each (command, condition) tuple by the mean of the corresponding shuffle distribution (same as in Figures 3B–3D).

Statistics Summary

In many analyses, we assessed whether a quantity calculated for a specific condition was significantly larger than expected from the distribution of the quantity due to subsampling the condition-pooled distribution. A p-value was computed by comparing the condition-specific quantity to the distribution of the quantity computed from subsampling the condition-pooled distribution. The "behavior-preserving shuffle of activity" and "matching the condition-pooled distribution" (see above) were used to construct the condition-pooled distribution.

The following is a summary of these analyses:

- Figure S1D, Quantity: distance between condition-specific average command subtrajectory and condition-pooled average command subtrajectory, P-value: computed using behavior-preserving shuffle.
- Figure S1E, Quantity: distance between condition-specific average next command and the condition-pooled average next command, P-value: computed using behavior-preserving shuffle.
- Figures 3B left and 3E right: Quantity: for a given command, distance between condition-specific average activity for a neuron and condition-pooled average activity for a neuron, P-value: behavior-preserving shuffle.
- Figures 3B right, 3D, and 3E left, middle: Quantity: for a given command, distance between condition-specific average population activity and condition-pooled average population activity, P-value: behavior-preserving shuffle.
- Figure 4G right: Quantity: for a given command, error between the invariant dynamics' prediction of condition-specific average activity for a neuron and the true condition-specific average activity for the neuron. P-value: distribution of prediction errors from shuffle dynamics (models fit on behavior-preserving shuffle and that made predictions using unshuffled data).
- Figure 4G left, middle: Quantity: for a given command, error between the invariant dynamics' prediction of condition-specific average population activity and the true condition-specific average population activity. P-value: distribution of prediction errors from shuffle dynamics (models fit on behavior-preserving shuffle and that made predictions using unshuffled data).
- Figure 5F: Quantity: for a given command, error between the invariant dynamics' prediction of condition-specific average next command and true condition-specific average next command. P-value: distribution of prediction errors from shuffle dynamics (models fit on behavior-preserving shuffle and that made predictions using unshuffled data).

In the above analyses, we also assessed the fraction of condition-specific quantities that were significantly different from the condition-pooled quantities or significantly predicted compared to a shuffled distribution (Figures 3E, 4G, 5F, S1D, S1E, S4D, S4I, and S6G). In order to aggregate over all data to determine whether condition-specific quantities were significantly different from shuffle or significantly predicted within a session relative to shuffle dynamics, we averaged the condition-specific quantity over the relevant dimensions (command, condition, and/or neuron) to yield a single aggregated value for a session. For example in Figure 3E right, we take the distance between average activity for a (command, condition, neuron) tuple and condition-pooled average activity for a (command, neuron) tuple, and we average this distance over (command, condition) tuples to yield an aggregated value that is used to assess if individual neurons are significant. We correspondingly averaged the shuffle distribution across all relevant dimensions (command, condition, and/or neuron). Together this procedure yielded a single aggregated value that could be compared to a single aggregated distribution to determine session significance. Finally, when we sought to aggregate over sessions, we took the condition-specific quantity that was aggregated within a session and averaged it across sessions and again compared it to a shuffle distribution of this value aggregated over sessions.

When R^2 was the metric assessed (Figures 4C, 4F, 5C–5E, S4B, S4F, and S4G), a single R^2 metric was computed for each session and compared to the R^2 distribution from shuffle models. This R^2 metric is known as the "coefficient of determination," and we note that it assesses how well the dynamics-predicted values (e.g. spike counts) account for the variance of the true values.

In some cases, a linear regression was fit between two quantities (Figures S6C, S6D, S6G, S6J, and S6K) on both individual sessions and on data pooled over all sessions, and the significance of the fit and correlation coefficient were both reported. In other cases where random effects such as session or analyzed command may have influenced the linear regression parameters (Figures S6F and S6G), a Linear Mixed Effect (LME) model was used with session and/or command modeled as random effects on intercept.

In Figure S5, a paired Student's t-test was used to compare two models' R^2 metric across sessions. Figure 6 analyzed simulations of OFC models, not experimentally-recorded data. Figures 6C and 6D used a paired Wilcoxon test and a LME to compare input magnitude between a pair of OFC models. Figures 6G and 6H used a Mann-Whitney U test and a LME to compare population distance between an OFC model and its shuffle distribution.

Current Biology, Volume *33*

Supplemental Information

Invariant neural dynamics drive commands to control different movements

Vivek R. Athalye, Preeya Khanna, Suraj Gowda, Amy L. Orsborn, Rui M. Costa, and Jose M. Carmena

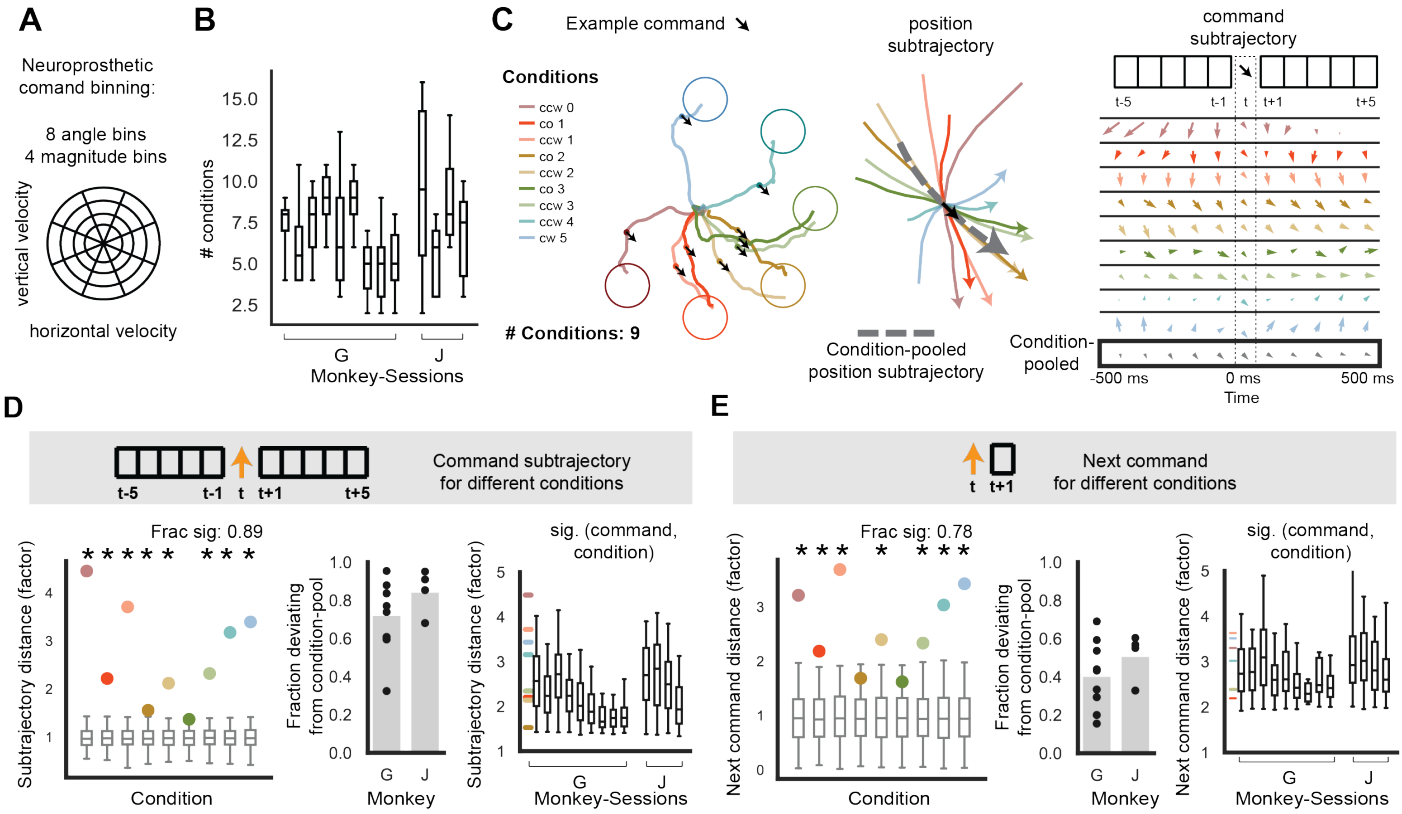

Figure S1. The same command is issued within different command trajectories to produce different movements. Related to Figure 1EF.

(A) To analyze the same command in different movements, the continuous-valued two-dimensional commands are categorized into one of 32 bins. Bins discretize the command angle into 8 equally spaced bins and magnitude into 4 bins, so that the pair of angle bin and magnitude bin results in 32 total bins. **(B)** The number of conditions in which the same command occurs frequently enough to be analyzed (>=15 occurrences) for each session analyzed from monkeys G and J. **(C)** *Left*. Repeated from Figure 1E for visualization: observations of an example command (shown as a black arrow) are plotted during single trials for nine conditions. The example command was in the -45 degree direction and the smallest magnitude bin of analysis (see STAR methods – "Command discretization for analysis"). *Center.* Local cursor position subtrajectory plot (aligned to command occurrence) repeated from Figure 1F for visualization, plus the condition-pooled cursor position subtrajectory (dashed gray arrow; average over command observations pooling over conditions). *Right.* Command subtrajectory plot repeated from Figure 1F for visualization, plus the condition-pooled command subtrajectory (gray; average over command observations pooling over conditions). **(D)** Analysis of whether the same command is used within different command subtrajectories in different conditions. The "condition-specific subtrajectory distance" is quantified between each condition-specific command subtrajectory and the condition-pooled command subtrajectory. *Left.* Colored dots show the condition-specific subtrajectory distance for the example command and conditions. The gray boxplots (whiskers span 0^{th}-95^{th} percentile) show the chance distribution of distances derived from bootstrapping, i.e. subsampling and averaging command subtrajectories from the condition-pooled distribution of command occurrences. For visualization, condition-specific subtrajectory distances are normalized by the mean of the bootstrapped distribution. 89% of the example conditions have command subtrajectories that are significantly different from the condition-pooled command subtrajectory. *Center.* Fraction of (command, condition) tuples with condition-specific command subtrajectories that are significantly different from the condition-pooled command subtrajectory. Condition-specific command subtrajectories are overall significantly different from the condition-pooled command subtrajectory: Monkey G [J]: p-value < 0.001 for 9/9 [4/4] sessions, p-value < 0.001 pooled over sessions (mean of command subtrajectory distances = 1.920 [2.342], mean (95th percentile) of bootstrapped distribution distances = 1.0 (1.01) [1.0 (1.02)]). *Right.* Distribution of condition-specific subtrajectory distances for individually significant (command, condition) tuples. Horizontal colored lines correspond to example conditions shown in left. **(E)**

Analysis of whether the same command is followed by distinct next commands in different conditions. For a given command and condition, the "condition-specific next command" is calculated as the average command following the given command in the given condition. For a given command, the "condition-pooled next command" is the average command following the given command, pooling over conditions. The "condition-specific next command distance" is calculated between the condition-specific next command and the condition-pooled next command. Distances are normalized by the mean of the bootstrapped shuffle distribution. *Left.* Colored dots show the condition-specific next command distance for the example command and conditions. *Center.* Fraction of (command, condition) tuples with condition-specific next commands that are significantly different from the condition-pooled next command. Condition-specific next commands are overall significantly different from the condition-pooled next command: Monkey G [J]: p-value < 0.01 for 9/9 [4/4] sessions, p-value < 0.001 for 8/9 [4/4] sessions, p-value < 0.001 pooled over sessions (mean of next command distances = 1.676 [2.178], mean (95th percentile) of bootstrapped distribution of next command distances = 1.0 (1.03) [1.0 (1.05)]). *Right.* Distribution of condition-specific next command distances for individually significant (command, condition) tuples. Horizontal colored lines correspond to example shown in left.

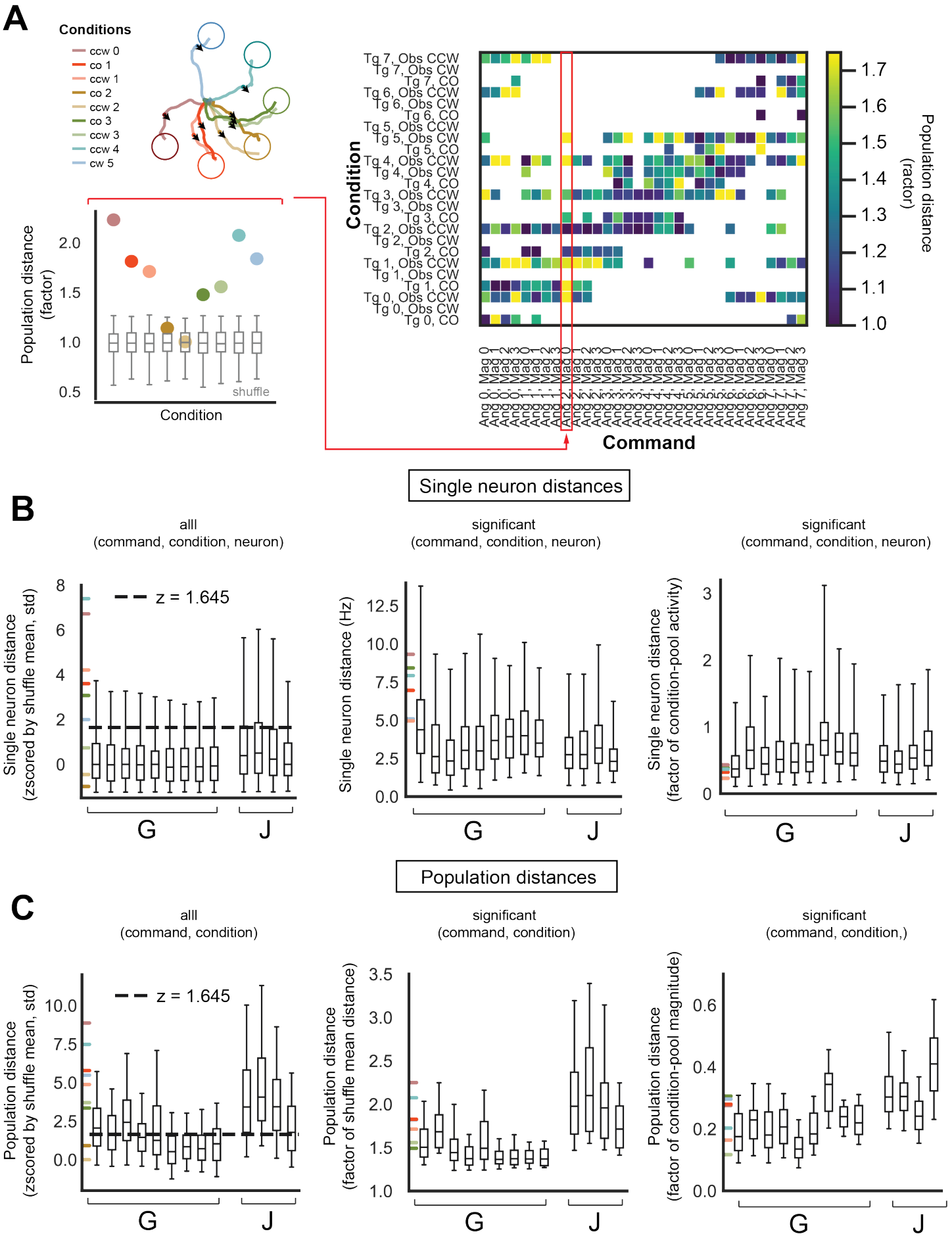
A
Conditions
ccw 0
co 1
ccw 1
co 2
ccw 2
co 3
ccw 3
ccw 4
cw 5
Population distance (factor)
2.0
1.5
1.0
0.5
shuffle
Condition
Condition
Command
Population distance (factor)
1.7
1.6
1.5
1.4
1.3
1.2
1.1
1.0
Single neuron distances
B
alll (command, condition, neuron)
significant (command, condition, neuron)
significant (command, condition, neuron)
Single neuron distance (zscored by shuffle mean, std)
z = 1.645
Single neuron distance (Hz)
Single neuron distance (factor of condition-pool activity)
G
J
Population distances
C
alll (command, condition)
significant (command, condition)
significant (command, condition,)
Population distance (zscored by shuffle mean, std)
Population distance (factor of shuffle mean distance)
Population distance (factor of condition-pool magnitude)

Figure S2. Distributions of condition-specific neural activity issuing a given command. Related to Figure 3B-E. In all plots, colored horizontal lines correspond to the example data in Figure 3B, and whiskers span the 2.5^{th} – 97.5^{th} percentiles of the data distribution.
(A) Population activity distances for all (command, condition) tuples in an example session. *Left.* Population activity distances (divided by the shuffle mean) for the example command, conditions, and session (Money G, session 0) from Figure 3B. *Right.* For the same example session, population distances (divided by shuffle mean) for all commands and conditions with sufficient datapoints (>= 15 observations per session) to be analyzed. Columns correspond to the analysis of one command across various conditions (rows). Boxes are not filled in (white) if there are not enough observations of the command in the condition. The example command in *left* is marked in *right* with a red box and the command bin label of "Ang 2, Mag 0". **(B)** Single neuron activity distances. *Left.* For all (command, condition, neuron) tuples, the distance (absolute difference) between condition-specific activity and condition-pooled activity, z-scored by the mean and standard deviation of the shuffle distribution's same distances. The horizontal black line illustrates an estimate of the significance threshold (z = 1.645, 95^{th} percentile of a standard normal distribution). In formal analysis, the empirical (command, condition, neuron) shuffle distribution's 95^{th} percentile serves as the significance threshold for each (command, condition, neuron) tuple. *Center.* For (command, condition, neuron) tuples that are significantly different than shuffle, the distribution of the distance (absolute difference) between condition-specific activity and condition-pooled activity. *Right.* For (command, condition, neuron) tuples that are significantly different than shuffle, the distribution of the distance (absolute difference) between condition-specific activity and condition-pooled activity, divided by the condition-pooled activity. **(C)** Population activity distances. *Left.* For all (command, condition) tuples, the distance between condition-specific activity and condition-pooled activity, z-scored by the mean and standard deviation of the shuffle distribution's same distances. The horizontal black line illustrates an estimate of the significance threshold (z = 1.645, 95^{th} percentile of a standard normal distribution). In formal analysis, the empirical (command, condition) shuffle distribution's 95^{th} percentile serves as the significance threshold for each (command, condition) tuple. *Center.* For (command, condition) tuples that are significantly different than shuffle, the distribution of the distance between condition-specific activity and condition-pooled activity, divided by the mean of the shuffle distribution of the same distance. *Right.* For (command, condition) tuples that are significantly different than shuffle, the distribution of the distance between condition-specific activity and condition-pooled activity, divided by the magnitude of the condition-pooled activity.

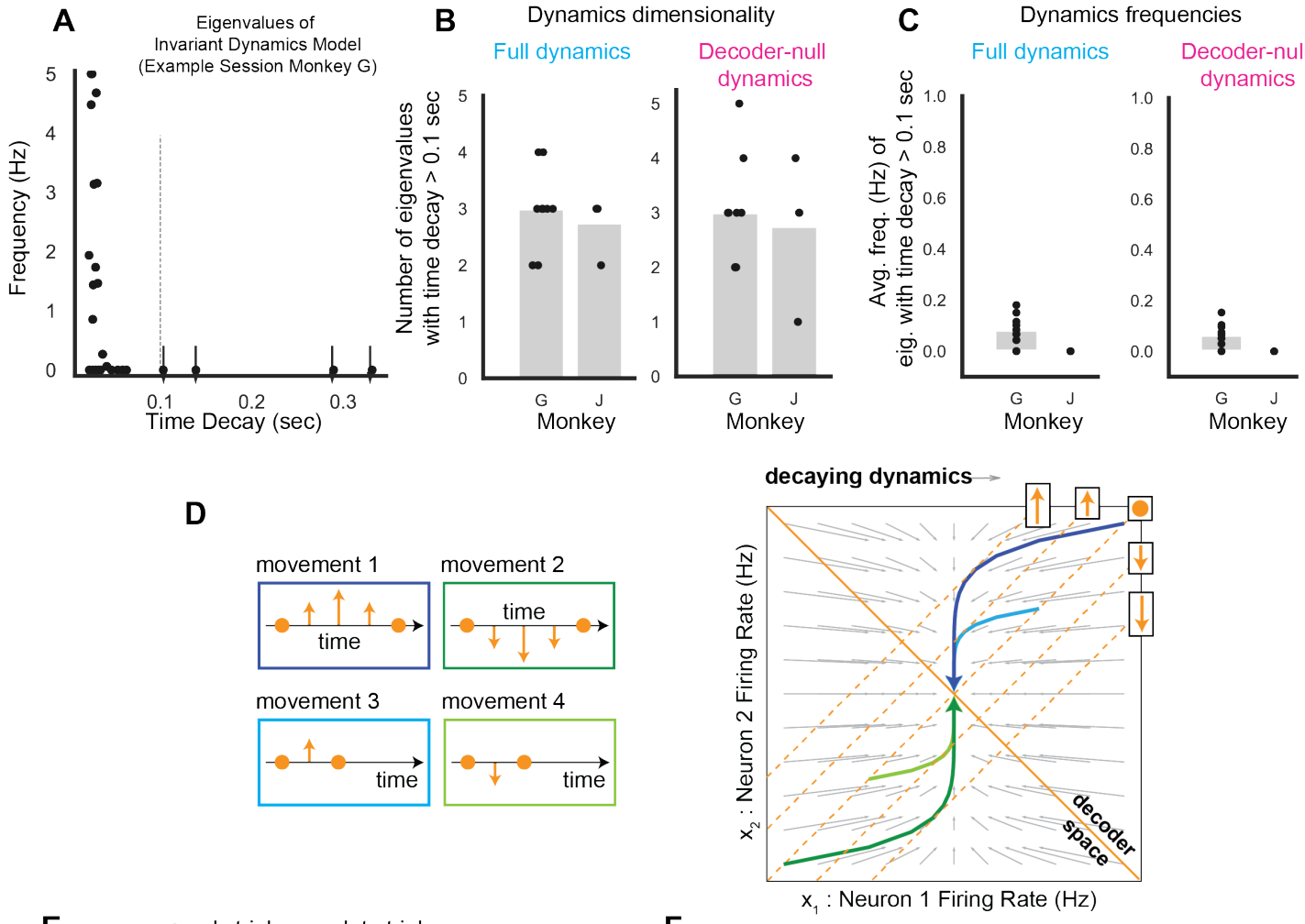
A
Eigenvalues of
Invariant Dynamics Model
(Example Session Monkey G)
Frequency (Hz)
Time Decay (sec)
B
Dynamics dimensionality
Full dynamics
Decoder-null dynamics
Number of eigenvalues with time decay > 0.1 sec
Monkey
C
Dynamics frequencies
Full dynamics
Decoder-null dynamics
Avg. freq. (Hz) of eig. with time decay > 0.1 sec
Monkey
D
movement 1
movement 2
movement 3
movement 4
time
decaying dynamics
decoder space
x2 : Neuron 2 Firing Rate (Hz)
x1 : Neuron 1 Firing Rate (Hz)
E
early trial
late trial
median trial length
Magnitude of residual from invariant dynamics model
Monkey G: session 0
Seconds from trial start
F
Fraction change in residual
Early trial
Late trial
Monkey G
Monkey J
G
Dynamics model R²
Monkey G
Monkey J
Seconds from trial start

Figure S3. Properties of invariant dynamics models. Related to Figures 2, 4C, and 6.
(A) The frequency and decay properties of the eigenvalues of the dynamics matrix for an example session's dynamics model (Monkey G, session 0). Eigenvalues with decay timescales greater than 0.1 seconds (the timescale at which the BMI updates the command and cursor) are denoted with arrows. **(B)** The dimensionality of the full dynamics matrix (decoder-null dynamics matrix) ranged from 2-4 (2-5) when considering the eigenvalues that had timescales greater than the BMI update's timescale of 0.1 seconds. The number of eigenvalues (each corresponding to one dimension of neural activity) with time decay > 0.1 seconds is shown for each monkey and session. **(C)** The average frequency of the full dynamics matrix (decoder-null dynamics matrix) eigenvalues with time decays > 0.1 seconds is ~0.1 (~0.06) Hz for Monkey G and is 0 Hz (0 Hz) for Monkey J. The average frequency (averaged over eigenvalues with time decays > 0.1 seconds) is shown for each monkey and session. **(D)** *Left.* Example movements which are composed of the same commands in different temporal orders. *Right.* Illustration of neural trajectories that follow invariant, decaying dynamics to control different movements. As illustrated in Figure 2B, the projection of neural activity into the decoder space determines the command that is issued for movement. As in Figure 4A, different neural activity patterns are used to issue the same command. For example, the first neural activity pattern in each trajectory is different, although they issue the same command. **(E)** Plot of the magnitude of neural activity that is not explained by the invariant dynamics model (i.e. the residual of the invariant dynamics model's predictions, which is the difference between observed neural activity and the prediction of neural activity based on the previous time step's neural activity). The trial-averaged L2-norm of the residual (divided by the square root of the number of neurons) is shown across time for an example session (Monkey G, session 0). **(F)** The residual magnitude in the late trial period, normalized to the residual magnitude in the early trial period. For analysis, the trial length was set to the median trial time for each session, and the early trial period (late trial period) was the first (last) one-third of the trial length. Each data point is the average of a single session, and the bar is the average across sessions. The residual is larger in the early trial period than the late trial period. Analysis was done using a linear-mixed effect model with session modeled as a random effect and early vs. late modeled as a fixed effect: Monkey G, slope = -0.242, $t(4746) = -24.926$, p-value = 3.87×10^{-137}, Monkey J slope = -0.0625, $t(1161) = -5.354$, p-value = 8.58×10^{-8}. Individual datapoints in the statistics were the average of the norm of the residuals during the early and late epochs for individual trials. Trials that were shorter than the trial median were not included in the statistics. **(G)** The R^2 (coefficient of determination) of the invariant dynamics model at each time point relative to the start of the trial, calculated for each session with held-out test data pooling across trials and conditions. The following is some interpretation of this data. At the very start of the trial, the model predicts spiking activity less well, consistent with large input driving neural activity. Then, there is a bump of high predictability, consistent with the initial large input evolving according to invariant dynamics. Then, the predictability decreases to an asymptote, consistent with ongoing feedback modulating neural activity.

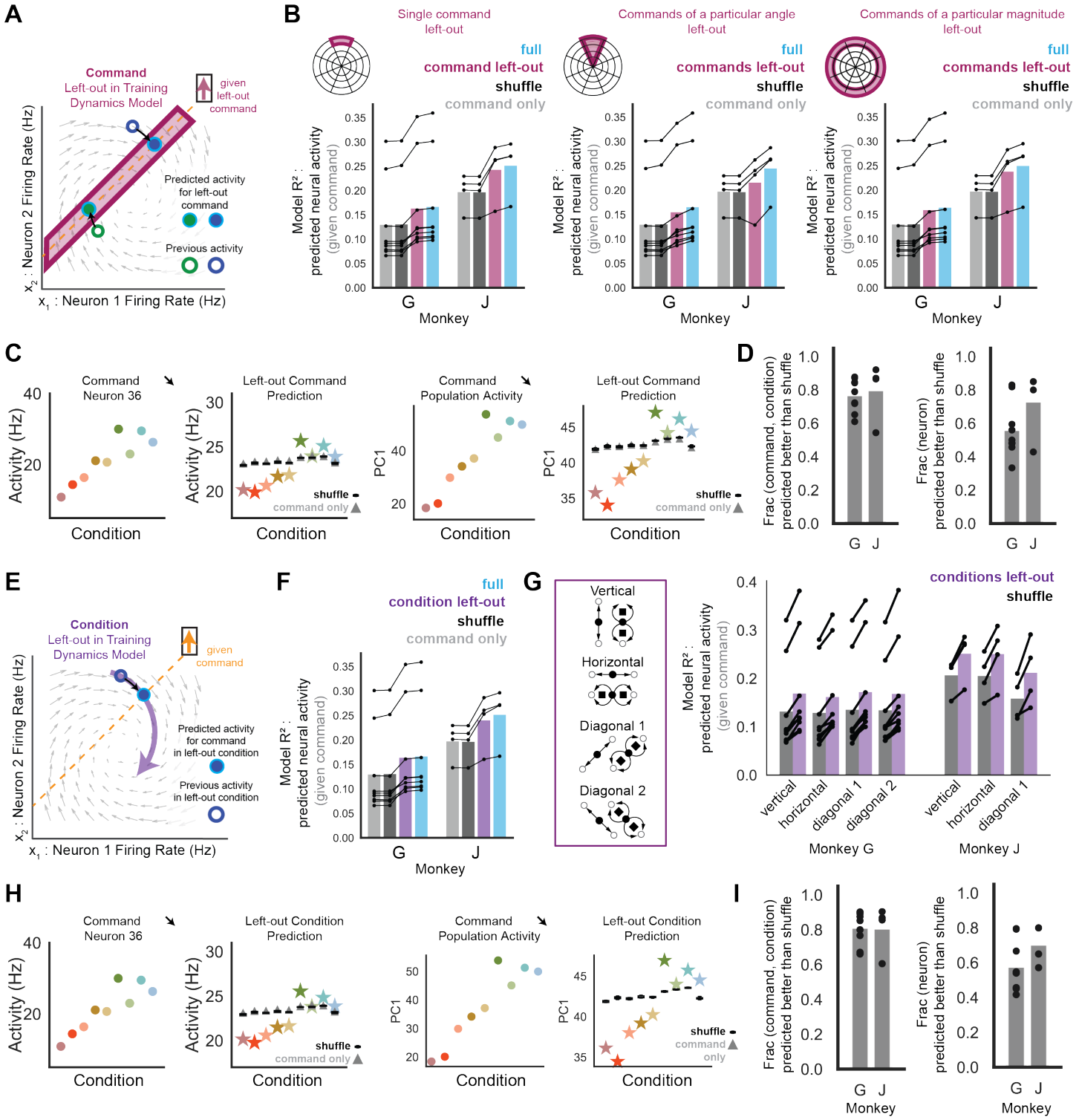

Figure S4. Generalization of invariant dynamics across sets of commands and conditions. Related to Figure 4B-E, G.

As in Figure 4C, each panel shows the R^2 of models predicting neural activity given the command it issues (Monkey G [J]: n=9 [4] sessions) including 1) the dynamics model that is trained using a complete dataset and that predicts held-out test data (cyan, labeled "full"), 2) the dynamics model that is trained with commands left out and that predicts the left-out commands (magenta, labeled "command left-out"), 3) the dynamics model that is trained using a shuffled complete dataset and that predicts held-out, unshuffled test data (black, labeled "shuffle"), and 4) a model trained using a complete dataset and that predicts held-out test data just given the command but not given previous neural activity (gray, labeled "command only"). See STAR methods – "Invariant dynamics models" – "*Generalization of invariant dynamics*". **(A)** Schematic (as in Figure 4B *left*).

We ask if a linear model of invariant dynamics can predict the neural activity that issues a given command that was left out of training the model. Magenta box indicates that neural activity that transitions to and from the given command are left-out of the dynamics model training data. **(B)** Generalization of invariant dynamics' predictions to sets of commands that were not used to train the invariant dynamics model. Predictions of left-out neural activity are significantly better than shuffle dynamics. *Left.* An individual command is left out and significantly predicted relative to shuffle dynamics (stats reported in Figure 4C for "command left-out dynamics"). The left-out model coefficient of determination (R^2) aggregates the predictions for each left-out command. *Middle.* All commands in a particular angular bin are left out and predicted significantly better than shuffle dynamics (Monkey G [J]: p-value < 0.001 for 9/9 [3/4], p-value n.s for 0/9 [1/4] sessions, p-value < 0.001 for sessions pooled, mean R^2 = 0.155 [0.216], mean (95th percentile) R^2 of shuffle = 0.130 (0.130) [0.196 (0.196)]). The left-out model R^2 aggregates the predictions for each left-out angle of commands. *Right.* All commands in a particular magnitude bin are left out and predicted significantly better than shuffle dynamics (Monkey G [J]: p-value < 0.001 for 9/9 [4/4] sessions, p-value < 0.001 for sessions pooled, mean R^2 = 0.159 [0.238], mean (95th percentile) R^2 of shuffle = 0.130 (0.130) [0.196 (0.196)]). The left-out model R^2 aggregates the predictions for each left-out magnitude of commands. **(C)** Visualization of observed and predicted neural activity for the example command and conditions from Figure 4DE. Predictions are from the invariant dynamics model that has been trained with data left out for the example command ("left-out command dynamics"). *Left.* Condition-specific average activity for the example neuron and command (repeated from Figure 4D *left* for visualization). *Left-center.* Prediction for the condition-specific average activity for the example neuron by the left-out dynamics model (stars), the shuffle dynamics model (black boxplot distribution), and the model predicting neural activity only using the command (gray triangle). *Right-center.* Condition-specific average population activity is visualized along the activity dimension that captured the most neural activity variance (the first principal component, labeled "PC1", from principal components analysis applied to condition-specific average population activity) for the example command and conditions (repeated from Figure 4E *left* for visualization). *Right.* Prediction for the condition-specific average population activity on PC1 by the left-out dynamics model (stars), the shuffle dynamics model (black boxplot distribution), and the model predicting neural activity only using the command (gray triangle). **(D)** Analyses of how well neural activity is predicted for individual (command, condition) tuples when the command is left out of training data for the dynamics model ("left-out dynamics"). *Left.* Fraction of (command, condition) tuples where left-out dynamics predicts condition-specific average population activity significantly better than shuffle dynamics (Monkey G [J]: n=9 [4] sessions). *Right.* Fraction of neurons, aggregated over all (command, condition) tuples, where left-out dynamics predicts the neuron's average activity significantly better than shuffle dynamics (Monkey G [J]: n=9 [4] sessions). **(E)** Schematic (as in Figure 4B *right*). We ask if the invariant dynamics model can predict neural activity for a given command and condition if all neural activity in that condition (illustrated in purple) is left-out of training the model. **(F)** Predictions of neural activity for a given command in a left-out condition are significantly better than shuffle dynamics (stats reported in Figure 4C for "condition left-out dynamics"). The left-out model R^2 aggregates the predictions for each left-out condition. **(G)** Generalization of invariant dynamics' predictions to sets of conditions that were not used to train the invariant dynamics model. *Left.* Schematics illustrate which conditions were left out and then predicted for each left-out set of conditions. *Right.* All neural activity in a particular set of left-out conditions is left out and predicted significantly better than shuffle dynamics. *Vertical conditions left out*. Monkey G [J]: p-value < 0.001 for 9/9 [4/4] sessions, p-value < 0.001 for sessions pooled (mean R^2 = 0.169 [0.251], mean (95th percentile) of shuffled R^2 = 0.131 (0.131) [0.206 (0.206)]). *Horizontal conditions left out.* Monkey G [J]: p-value < 0.001 for 9/9 [4/4] sessions, p-value < 0.001 for sessions pooled (mean R^2 = 0.161 [0.251], mean (95th percentile) of shuffled R^2 = 0.128 (0.128), [0.204, (0.205)]). *Diagonal 1 conditions left out*. Monkey G [J]: p-value < 0.001 for 9/9 [4/4] sessions, p-value < 0.001 for sessions pooled (mean R^2 = 0.172 [0.212], mean (95th percentile) of shuffled R^2 = 0.135 (0.135) [0.158 (0.158)]). *Diagonal 2 conditions left out*. Monkey G: p-value < 0.001 for 9/9 sessions, p-value < 0.001 for sessions pooled (mean R^2 = 0.168, mean (95th percentile) of shuffled R^2 = 0.134 (0. 134)). Monkey J: obstacle task did not have these diagonal conditions. **(H)** Visualization of observed and predicted neural activity for the example command and conditions from Figure 4DE. Predictions are from the invariant dynamics model that has been trained with data left out for each condition separately ("left-out condition dynamics"). Thus, each prediction is made by a separate model with the corresponding condition left out of training data. *Left.*

Condition-specific average activity for the example neuron and command (repeated from Figure 4D *left* for visualization). *Left-center.* Prediction for the condition-specific average activity for the example neuron by the left-out dynamics models (stars), the shuffle dynamics model (black boxplot distribution), and the model predicting neural activity only using the command (gray triangle). *Right-center.* Condition-specific average population activity is visualized along PC1 (see legend (C) for explanation) for the example command and conditions (repeated from Figure 4E *left* for visualization). *Right.* Prediction for the condition-specific average population activity on PC1 by the left-out dynamics models (stars), the shuffle dynamics model (black boxplot distribution), and the model predicting neural activity only using the command (gray triangle). **(I)** Analyses of how well neural activity is predicted for individual commands and conditions when the condition is left out of training data for the dynamics model ("left-out dynamics"). *Left.* Fraction of (command, condition) tuples where left-out dynamics predicts condition-specific average population activity significantly better than shuffle dynamics (Monkey G [J]: n=9 [4] sessions). *Right.* Fraction of neurons, aggregated over all (command, condition) tuples, where left-out dynamics predicts the neuron's average activity significantly better than shuffle dynamics (Monkey G [J]: n=9 [4] sessions).

Alternative model: tuning to behavior

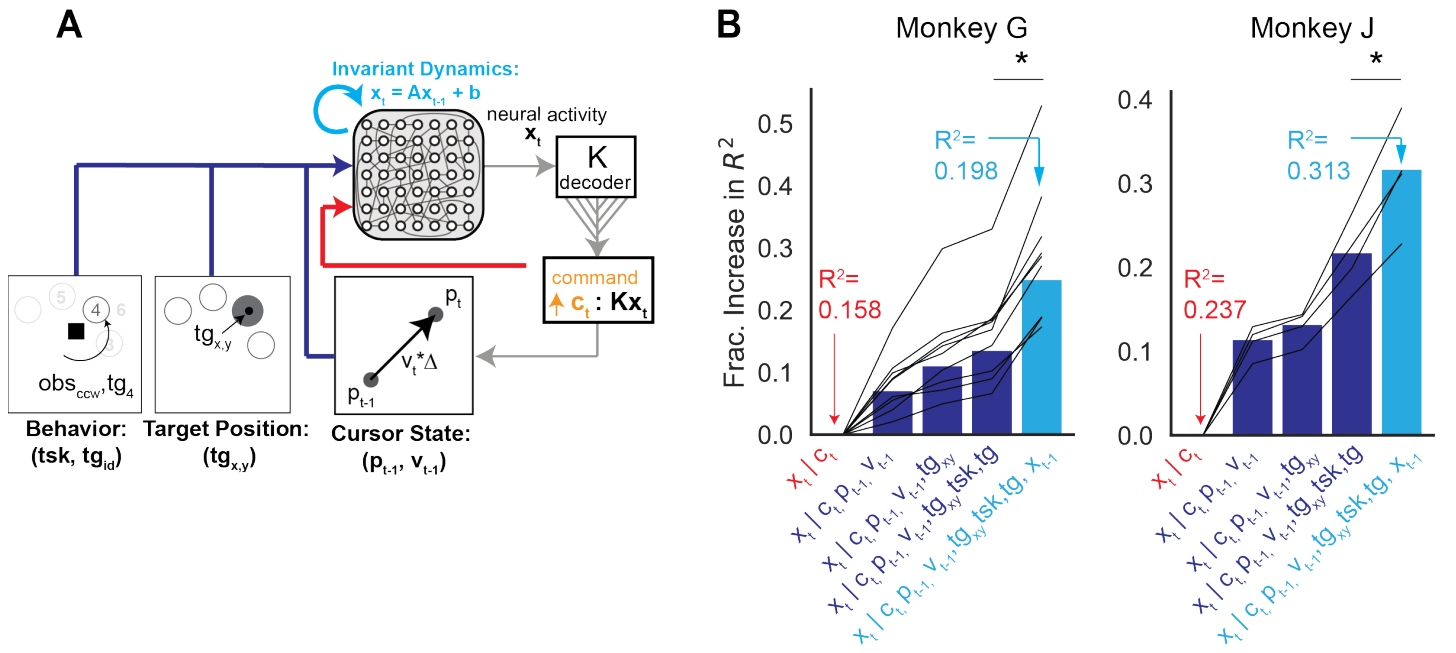

Alternative model: non-linear dynamics
fit using piecewise linear dynamics

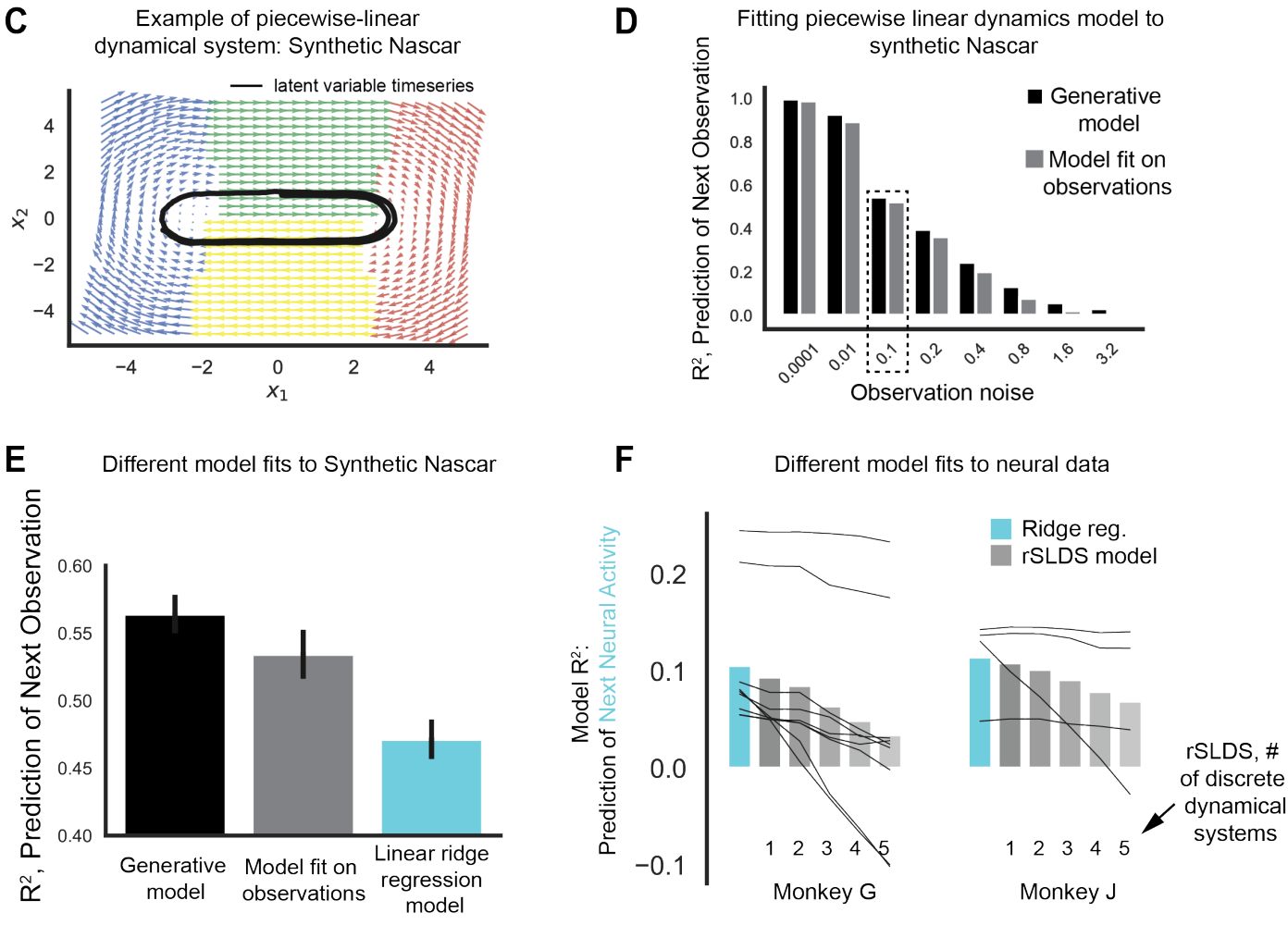

Figure S5. Alternative models to predict neural activity. Related to Figures 4AC and 5C.
Invariant dynamics predict neural activity beyond encoding of cursor, target, and task.
(A) Schematic of task-relevant behavior variables that may be encoded in motor cortex population activity x_t at time t during BMI performance, including the command c_t (orange), cursor position p_{t-1} and velocity v_{t-1}, target position $tg_{x,y}$ in the 2D workspace, a categorical variable tg that encodes the target, and a categorical variable tsk that encodes task (center-out versus obstacle-avoidance) and whether the trajectory went clockwise vs counterclockwise for the obstacle-avoidance task. **(B)** Fraction increase in coefficient of determination (R^2) for models predicting neural activity for a given command c_t as an increasing number of predictors are incorporated. Reported R^2 values are on left-out test data, so increasing the number of predictors does not trivially increase R^2. Incorporating invariant neural dynamics (cyan) significantly improves upon predictions from the model with all task-relevant variables (right-most dark blue bar "behavior encoding model": $x_t | \, c_t, p_{t-1}, v_{t-1}, tg_{xy}, tsk, tg$) (Monkey G: paired Student's t-test: N = 18, T = -7.182, p-value = 9.41e-05, Monkey J: paired Student's t-test: N = 8, T = -5.141, p-value = 0.0143).
Non-linear invariant dynamics do not predict neural activity beyond linear invariant dynamics. To test if neural activity predictions may be improved by using a non-linear model of invariant dynamics, we chose to use a recurrent switching linear dynamics system (rsLDS) model [S1]. The rsLDS has the advantage of capturing non-linear dynamics yet still having parameters that are interpretable using linear systems analysis. Specifically, we used a "recurrent-only" switching linear dynamical system that switches between dynamical systems depending only on the latent state[S1]. This was selected for interpretability (i.e. dynamics always obey specific linear dynamics A when the latent state is in a specific region of state space).
(C) We first ensured we could properly fit the non-linear dynamics[S1] to a toy example, the "Nascar example" ("ssm" repository -- https://github.com/lindermanlab/ssm) that has activity evolving under a piecewise combination of four linear dynamical systems. **(D)** Forward prediction accuracy of the true Nascar example generative models (black bars) and the fit models (gray bars) confirmed that our fitting procedure found model parameters that yielded comparable accuracy in forward model prediction to the generative model, even when noise was added to observations. Both models suffered similarly from additive noise to the observations. **(E)** In the case of mild additive noise (noise = 0.1, indicated in dotted box in (D)), both the nascar generative (black) and fit (gray) rsLDS models outperformed linear ridge regression (cyan) in prediction of future observations, as expected due to the non-linear generative model. **(F)** Comparison of rsLDS models (gray) vs. linear ridge regression (cyan) fit on neural data as animals perform BMI. We set the latent state dimensionality to the number of neurons that were recorded. This choice was made after sweeping latent state dimensionalities and observing increasing log-likelihoods with higher latent state dimensionality on held-out test data. The linear ridge regression models outperformed the rsLDS models on held-out test data, and the rsLDS performance worsened as more dynamical systems were incorporated (i.e., as more non-linearities were added).

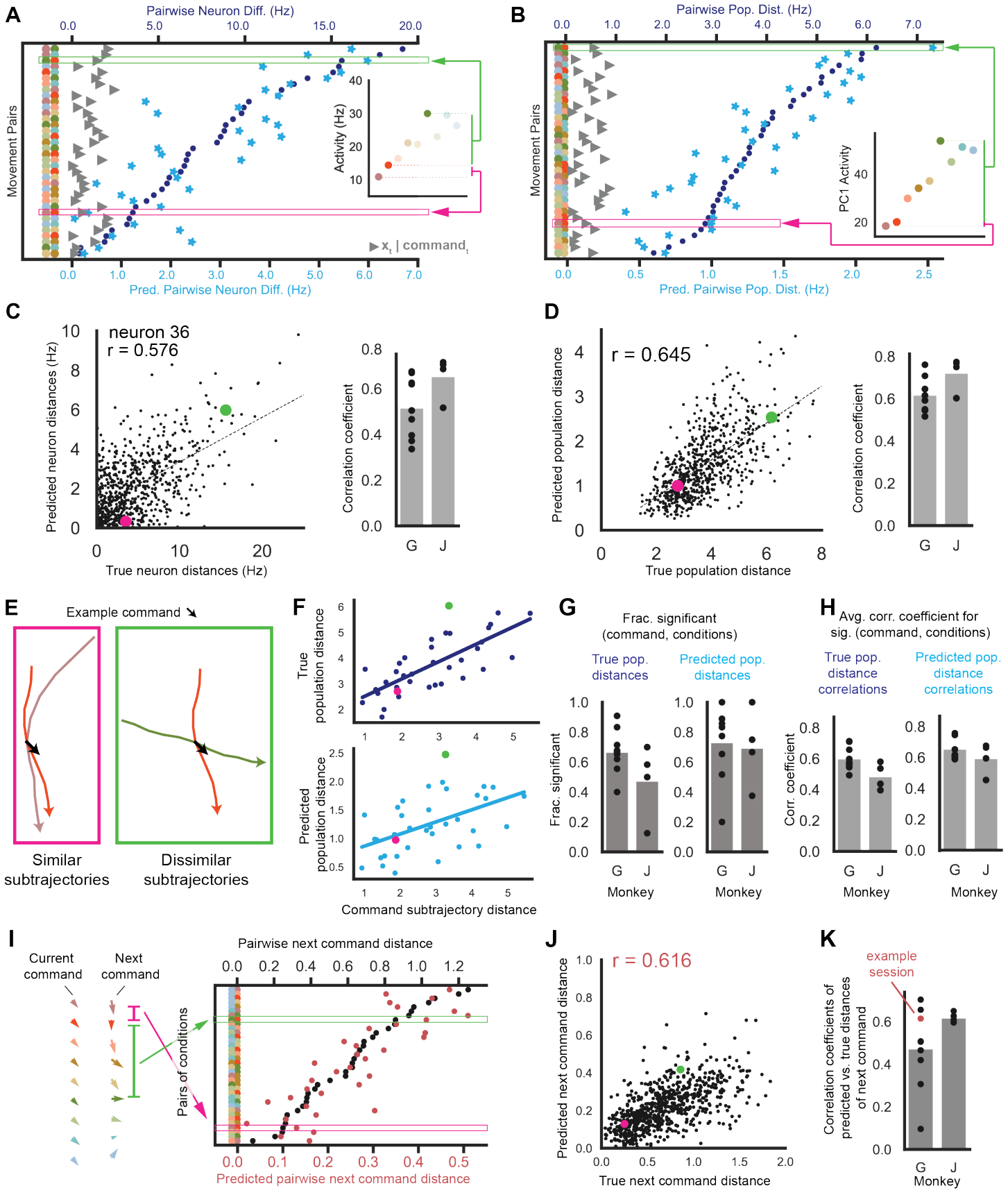

Figure S6. Invariant dynamics predicts structure across pairs of conditions. Related to Figures 3 and 4ADEG.

(A) For a given example command, visualization of the distance between single neuron activity across pairs of conditions (dark blue dots, top x-axis) and the distance between dynamics-predictions of activity across pairs of

conditions ("predicted distance", cyan blue dots, bottom x-axis), shown for the command, neuron (neuron 36), and conditions in Figure 3B. As comparison, activity was predicted given just the continuous-valued commands for each condition in the pair (i.e. activity predicted without an invariant dynamics model), and the distance between these predictions across pairs of conditions is shown (gray triangles which are measured on the cyan scale). The individual conditions composing each condition-pair are indicated with colored dots at the left of the plot. Condition-pairs are sorted by increasing distance. Two examples of condition-pairs are highlighted in pink and green, and the corresponding activity of the individual conditions is shown in the inset. The position subtrajectories for these condition-pairs are shown below in (E). **(B)** Same as (A) but for distances between population activity. Inset shows differences in PC1 activity for illustration, but population distances are calculated in the high-dimensional decoder-null space (see STAR methods – "Analysis of activity issuing a given command"). **(C)** *Left.* For a given command, correlation between the true distance across condition-pairs (x-axis) and predicted distance (y-axis), for the example neuron and session in (A) and Figure 3B. Dots include all commands and corresponding condition-pairs analyzed for this example session. Pink and green dots indicate condition pairs highlighted in (A). *Right.* Correlation coefficients between true distance across condition-pairs and predicted distance. Each data point is one session, averaging over neurons for all (command, condition-pair) tuples, and the bar is the session-average. Dynamics-predicted distances across condition-pairs are significantly correlated with true distances: Monkey G: p-value < 0.001 for 9/9 sessions, p-value < 0.001 pooled over sessions (linear regression: slope = 0.221, rv = 0.584, N=377489). Monkey J: p-value < 0.001 for 4/4 sessions, p-value < 0.001 pooled over sessions (linear regression: slope = 0.317, rv = 0.693, N = 34643). **(D)** *Left.* Same as (C) *left*, except for population activity distances. *Right.* Same as (C) *right*, except for population activity distances. Each data point is for one session, averaging over all (command, condition-pair) tuples, and the bar is the session-average. Dynamics-predicted distances across condition-pairs are significantly correlated with true distances: Monkey G: p-value < 0.001 for 9/9 sessions, p-value < 0.001 pooled over sessions (linear regression, slope = 0.350, rv = 0.638, N = 5112). Monkey J: p-value < 0.001 for 4/4/ sessions, p-value < 0.001 pooled over sessions (linear regression, slope = 0.449, rv = 0.800, N=1714). **(E)** Analysis of whether neural activity for a given command is more similar across conditions that have more similar command subtrajectories, and whether this structure is predicted by a model of invariant dynamics. Illustration of example condition-pairs used in (A)-(D) with similar (pink) and dissimilar (green) command subtrajectories (position subtrajectories are plotted). **(F)** *Top.* For the example command from Figure 3B, correlation between population activity distances and command subtrajectory distances for condition-pairs in (A). Pink and green points correspond to pairwise comparisons illustrated in (E). *Bottom*. Same as *Top* but correlation between dynamics-predicted distances and command subtrajectory distances. **(G)** *Left.* Fraction of commands that occur frequently (in > 5 conditions) that exhibit a significant correlation between 1) population activity distance across a condition-pair and 2) command subtrajectory distance across a condition-pair. Over all commands, command subtrajectory distance across a condition-pair is significantly correlated with population activity distance: Monkey G: p-value < 0.001 for 9/9 sessions, pooled over sessions: linear mixed effect (LME) model with command identity and session as random effects: N=4674, z = 31.04, p = 1.36e-211, Monkey J: p-value < 0.05 for 4/4 sessions, p-value < 0.001 for 3/4 sessions, pooled over sessions: LME model with command identity and session as random effects: N=1629, z = 14.18, p-value = 1.22e-45. *Right.* Fraction of commands that occur frequently (in > 5 conditions) that exhibit a significant correlation between 1) the dynamics-predicted population activity distance across a condition-pair and 2) the command subtrajectory distance. Over all commands, command subtrajectory distance across a condition-pair is significantly correlated with dynamics-predicted population activity distance (Monkey G: p-value < 0.01 for 9/9 session, p-value < 0.001 for 8/9 sessions, p-value < 0.001 for pooled sessions (LME with command identity and session modeled as random effects, N = 4674, z = 33.1, p-value = 3.92e-240), Monkey J: p-value < 0.001 for 4/4 sessions, p-value < 0.001 for pooled sessions (LME with command identity and session modeled as random effects, N = 1629, z = 22.5, p-value = 5.93e-112)). **(H)** *Left.* Average correlation coefficient of 1) true population distance across a condition-pair versus 2) command subtrajectory distance, aggregated across significant command-conditions. *Right*. Same as *Left* but correlation of 1) predicted population distance across a condition-pair versus 2) command subtrajectory distance. **(I)** Analysis of how condition-specific neural activity issuing the same current command (c_t) transitions forward to issue distinct next commands (c_{t+1}).

Left. For the example command in Figure 3B, visualization of the average current and next command for each example condition. *Right.* Visualization of the distance between the dynamics-predicted next commands for each condition in a pair (red, bottom x-axis) and the distance between the true next commands across a condition-pair (black, top x-axis). The individual conditions composing each condition-pair are indicated with colored dots at the left of the plot. Condition-pairs are sorted by increasing distance in next command. Two examples of condition pairs are highlighted in pink and green (same as in (A)). **(J)** For the example session, correlation of 1) the distance between true next commands across a condition-pair (x-axis) and 2) the distance between predicted next commands across a condition-pair (y-axis). Dots include all commands and corresponding condition-pairs. Pink and green dots indicate condition-pairs highlighted in (I). **(K)** Same as (J) except for all sessions (example session is shown in red). Dynamics-predicted distance between next commands across a condition-pair is significantly correlated with the true distance: Monkey G: p-value < 0.001 for 8/9 sessions, p-value n.s. for 1/9 sessions, p-value < 0.001 for pooled sessions (linear regression, slope=0.263, rv =0.76), Monkey J: p-value < 0.001 for 4/4 sessions, p-value < 0.001 for pooled sessions (linear regression, slope=0.178, rv =0.63).

Analysis description	Figure	Monkey	Session significance			Pooled session statistics vs. shuffle			
			# sessions with p-value < 0.001	*# sessions with 0.001 < p-value < 0.05*	*# sessions with p-value > 0.05 (n.s.)*	*mean of data*	*5th percentile of shuffle*	*mean of shuffle*	*95th percentile of shuffle*
Distances aggregating over (command, condition, neuron) tuple	3B	G	9/9			1.167		1.004	1.010
		J	4/4			1.235		0.745	0.757
Population distance aggregating over (command, condition) tuple	3D	G	9/9			1.222		1.0	1.007
		J	4/4			1.724		1.0	1.019
R2 of full dynamics predictions of neural activity given command (cyan bar)	4C	G	9/9			0.167		0.130	0.130
		J	4/4			0.252		0.196	0.196
R2 of command left-out dynamics predictions of neural activity given command (magenta bar)	4C	G	9/9			0.163		0.130	0.130
		J	4/4			0.243		0.196	0.196
R2 of condition left-out dynamics predictions of neural activity given command (purple bar)	4C	G	9/9			0.163		0.130	0.130
		J	4/4			0.240		0.196	0.196
Single neuron error between true and dynamics-predicted neural activity given command, aggregating over all (command, condition, neuron) tuples	4D	G	9/9			1.232	1.359	1.359	
		J	4/4			1.182	1.454	1.455	
Population error between true and dynamics-predicted neural activity given command, aggregating over all (command, condition) tuples, normalized by the mean of the shuffle distribution	4E	G	9/9			0.883	0.99	1.0	
		J	4/4			0.809	0.99	1.0	
R2 of condition-specific component of neural activity predicted by dynamics	4F	G	9/9			0.226		-0.006	-0.005
		J	4/4			0.330		-0.016	-0.014
R2 of full dynamics predictions of neural activity (cyan bar)	5C	G	9/9			0.100		0.055	0.055
		J	4/4			0.117		0.051	0.053
R2 of command left-out dynamics predictions of neural activity (magenta bar)	5C	G	9/9			0.099		0.055	0.055
		J	4/4			0.113		0.051	0.053
R2 of condition left-out dynamics predictions of neural activity (purple bar)	5C	G	9/9			0.097		0.055	0.055
		J	4/4			0.103		0.051	0.053
R2 of decoder-null dynamics predictions of neural activity (pink bar)	5C	G	9/9			0.083		0.055	0.055
		J	4/4			0.085		0.051	0.053
R2 of full dynamics predictions of command (orange bar)	5D	G	9/9			0.315		0.264	0.266
		J	4/4			0.212		0.186	0.188
R2 of command left-out dynamics predictions of command (magenta bar)	5D	G	9/9			0.310		0.264	0.266
		J	4/4			0.211		0.186	0.188
R2 of condition left-out dynamics predictions of command (purple bar)	5D	G	9/9			0.305		0.264	0.266
		J	2/4	1/4	1/4	0.193		0.186	0.188
R2 of decoder-null dynamics predictions of command (pink bar)	5D	G			9/9	0.0		0.264	0.266
		J			4/4	0.0		0.186	0.188
Error in prediction of condition-specific next command	5E	G	9/9			3.956	5.38	5.40	
		J	4/4			7.324	9.240	9.305	
Fraction of (command, condition) tuples with sign of next command's angle is accurately predicted with full dynamics	5G	G	9/9			0.708		0.535	0.541
		J	4/4			0.617		0.473	0.480
Error in prediction of next command's angle with full dynamics	5G	G	9/9			19.503	26.415	26.564	
		J	4/4			9.608	12.636	12.779	

Table S1. Comparisons to shuffled datasets. Related to Figures 3-5. Statistics computed for individual animal sessions and pooling across sessions compared to shuffled datasets as described in main text and STAR Methods.

Analysis description	**Figure**	**Monkey**	**Session significance**		**Pooled session statistics (linear mixed effect model with session modeled as random effect)**		
			Individual session comparison test	*# of sessions w/ p-value < 0.05*	*Number of datapoints (N)*	*z statistic*	*p-value*
Input magnitude, comparison between full dynamics and no dynamics	6C	G	Wilcoxon signed-rank test with conditions paired	9/9	432	10.49	9.67e-26
		J		4/4	192	5.20	1.92e-7
Input magnitude, comparison between decoder-null dynamics and no dynamics	6D	G	Wilcoxon signed-rank test with conditions paired	0/9	432	0.002	0.998
		J		0/4	192	-0.003	0.990
Distance between average population activity for a (command, condition) compared to shuffle: Full dynamics (cyan)	6G	G	Mann-Whitney U test	9/9	4906	-23.09	6.37e-118
		J		4/4	2408	-16.68	1.77e-62
Distance between average population activity for a (command, condition) compared to shuffle: No dynamics (black)	6G	G	Mann-Whitney U test	0/9	4334	0.168	0.866
		J		0/4	2188	0.462	0.644
Distance between average population activity for a (command, condition) compared to shuffle: Decoder-null dynamics (pink)	6H	G	Mann-Whitney U test	0/9	4488	0.932	0.351
		J		0/4	2252	-1.490	0.136
Distance between average population activity for a (command, condition) compared to shuffle: No dynamics (black)	6H	G	Mann-Whitney U test	0/9	4482	0.611	0.541
		J		0/4	2250	0.449	0.654

Table S2. Simulation statistics. Related to Figure 6. Statistics computed for simulations performed on individual animal sessions and pooling across sessions as described in main text and STAR Methods.

Supplemental Reference

S1. Linderman, S., Johnson, M., Miller, A., Adams, R., Blei, D., and Paninski, L. (2017). Bayesian Learning and Inference in Recurrent Switching Linear Dynamical Systems. In Proceedings of the 20th International Conference on Artificial Intelligence and Statistics Proceedings of Machine Learning Research., A. Singh and J. Zhu, eds. (PMLR), pp. 914–922.